MAGMATIC AND TECTONIC EFFECTS OF THE INTERACTION OF THE JUAN DE FUCA MID-OCEAN RIDGE WITH THE COBB HOTSPOT

By

DAVID JOHN CHADWICK

A DISSERTATION PRESENTED TO THE GRADUATE SCHOOL
OF THE UNIVERSITY OF FLORIDA IN PARTIAL FULFILLMENT
OF THE REQUIREMENTS FOR THE DEGREE OF
DOCTOR OF PHILOSOPHY

UNIVERSITY OF FLORIDA

2002

ACKNOWLEDGMENTS

I would like to thank Dr. Mike Perfit for his tremendous help on this dissertation and for helping to prepare me for life as a research scientist. Mike was helpful in finding the all-important funds that kept me from starving to death. Without question, the most important choice graduate students make is deciding who their advisor will be, and I chose very well. I thank him for sending me out on high-seas adventures and to Papua New Guinea and Iceland.

I would also like to thank Drs. Paul Mueller, David Foster, Ann Heatherington, and Willie Harris for serving on my committee, reading this lengthy tome, and for offering help and guidance.

Much of the geochemical data in this study was provided by the analytical wizardry of Ian Ridley, Ian Jonnassen, Petrus le Roux, and David Graham. I offer many thanks to Marianne Kozuch for showing me the ropes on the mass spectrometer and in the clean lab; she was a tremendous help.

Most importantly, I thank my family. I would not be able to spend my life in this decadent, student-for-life fashion if it weren't for the constant moral and occasional financial support of my parents. I thank the newest member of my family, my fiancé Claire, for her help with this dissertation, and for her constant love, friendship, and support ♥.

TABLE OF CONTENTS

page

ACKNOWLEDGMENTS ii

ABSTRACT v

CHAPTERS

1 INTRODUCTION 1

2 MAGMATIC EFFECTS OF THE INTERACTION OF THE JUAN DE FUCA RIDGE WITH THE COBB HOTSPOT 8

- Regional Geology 8
- Morphological Characteristics of the Axial Segment 15
- Sample Collection and Petrographic Analyses 17
- Major Element Geochemistry 19
- Trace Element Geochemistry 38
- Isotope Geochemistry 51
- Discussion 57

3 TEMPORAL GEOCHEMICAL VARIABILITY OF AXIAL SEGMENT LAVAS REVEALED BY RIDGE CAPTURE 67

- Introduction 67
- Sample Recovery and Geological Observations 76
- Ridge Capture 82
- Temporal Geochemical Variations 87
- Discussion 101

4 THE COBB HOTSPOT: A FIXED MANTLE MELTING ANOMALY WITH MORB-LIKE GEOCHEMICAL CHARACTERISTICS 104

- Introduction 104
- The Cobb Hotspot 106
- Discussion 107
- Model Age of the Cobb Hotspot 111

5 SUMMARY AND CONCLUSIONS 116

Magmatic Consequences of Ridge-Hotspot Interaction 116
Capture of the Axial Segment by the Cobb Hotspot 119
The MORB-like Cobb Hotspot 120

APPENDIX: ANALYTICAL METHODS 121

REFERENCES 124

BIOGRAPHICAL SKETCH 132

Abstract of Thesis Presented to the Graduate School
of the University of Florida in Partial Fulfillment of the
Requirements for the Degree of Doctor of Philosophy

MAGMATIC AND TECTONIC EFFECTS OF THE INTERACTION OF THE JUAN DE FUCA MID-OCEAN RIDGE WITH THE COBB HOTSPOT

By

DAVID JOHN CHADWICK

May 2002

Chair: Dr. Michael Perfit
Major Department: Geological Sciences

The Cobb hotspot has had a major influence on the Axial Segment, one of seven segments of the Juan de Fuca Ridge and the one the hotspot is directly interacting with. The Axial Segment has anomalous shallow bathymetry and is dominated by volcanic landforms instead of the tectonic features found on the other segments. Major element, trace element, and isotopic studies of the lavas erupted along the Axial Segment reveal variable mixing of the indigenous mid-ocean ridge basalt source with the Cobb hotspot magmas, with the proportion of the mid-ocean ridge component increasing with distance from the hotspot.

The hotspot has also "captured" the Axial Segment, a process that is also occurring where the Mid-Atlantic Ridge overlies the Iceland hotspot. Ridge capture has caused the neo-volcanic zone to remain fixed over the hotspot for about 0.4 Ma in spite of continued migration of the rest of the ridge system. Ridge capture has led to the exposure of basalts of different ages along the Axial Segment in a spatial framework, allowing for geochemical changes to be detected between younger and older basalts. Younger basalts are more mafic and slightly more enriched in some incompatible trace elements than older basalts, suggesting a recent influx of primitive magmas into the Axial Segment system that have a slightly higher proportion of the Cobb hotspot end-member.

The Cobb hotspot itself is anomalous in that it exhibits none of the radiogenic isotopic enrichments observed at other hotspots, although it is clearly a fixed mantle plume with a source below the mobile mantle. Although the hotspot has major and trace element characteristics that are distinct from the nearby Juan de Fuca ridge, these are within global mid-ocean ridge basalt geochemical ranges. A set of 'model ages' calculated for Cobb-Eickelberg basalts suggest that the hotspot is too young to be derived from oceanic crustal material that has undergone subduction to the core-mantle boundary.

CHAPTER 1
INTRODUCTION

Plate tectonics and hotspot volcanism are two of the most dominant geological processes that affect the Earth's surface. They build mountains, sever continents to open ocean basins, and place immense volumes of molten rock from the Earth's interior onto its surface. As powerful and global in scale as these processes may be, they are merely a consequence of the cooling of the planet, the surface manifestation of the removal of heat generated by radioactive decay and heat remaining from the genesis of the planet 4.6 billion years ago.

The primary magmatic and tectonic features created by plate tectonic processes are mid-ocean ridges, which comprise a planet-girdling mountain chain where new oceanic lithosphere is created, and subduction zones, where this lithosphere is recycled back into the mantle. Hotspots may complete the cycle; subducted lithosphere is thought to be dense enough to sink into the deep mantle, perhaps down to the D" layer at the core-mantle boundary. Here the material may heat and become buoyant, rising as solid-state plumes back toward the surface where they partially melt and form long hotspot chains like the Hawaiian Islands and the Cobb-Eickelberg Seamount chain (Hauri and Hart, 1993; Albarede and Van der Hilst, 1999). Material in these hotspot plumes may also replenish the asthenosphere, the upper mantle material tapped by mid-ocean ridges, where the cycle begins anew (Yale and Phipps Morgan, 1998). This pattern of convection in the Earth may explain why hotspots are more prevalent near spreading centers than subduction zones (Marzocchi and Mulargia, 1993; Weinstein and Olson, 1989).

Recent mid-ocean ridge research has largely been focused on how magmatic, tectonic, and geochemical characteristics vary with rates of spreading, and the nature and scale of ridge segmentation and mantle geochemical heterogeneity (Perfit and Chadwick, 1998). Fast-spreading ridges like the East Pacific Rise are robust magmatic systems, with relatively common volcanic eruptions, widespread hydrothermal activity, and a broad, axial high morphology that emulates a shield volcano (Macdonald, 1989). Slow spreading ridges like the Mid-Atlantic Ridge are dominated by tectonism, with wide axial valleys and extensive normal and detachment faulting, less volcanic and hydrothermal activity, and generally larger constructional volcanic features. Intermediate rate spreading ridges, such as the Juan de Fuca Ridge, generally have features that are transitional between the ridges with fast and slow spreading rates.

Recent hotspot research has involved the geochemical classification of mantle plumes and determining the sources of radiogenic isotope and incompatible trace element enrichments (Zindler and Hart, 1986; Saunders, 1988; Hart, 1988); 'EMI' (enriched mantle) plumes such as Kerguelen have chemical characteristics that possibly reflect enrichment by lower continental crust, 'EMII' plumes like Samoa have characteristics that may result from mixing depleted mantle with continental sediments, and 'HIMU' plumes such as St. Helena have chemical features that suggest sources with a subducted oceanic crust component. The Depleted Mantle ('DM') component is presumed to be derived from the shallow mid-ocean ridge basalt (MORB) mantle source, and is thought to mix with the other components.

Hotspots interact with mid-ocean ridges at 18 locations on the Earth, including Iceland, the Galapagos Islands, Easter Island, and the Azores (see http://triton.ori.u-tokyo.ac.jp/~intridge/hotspot.htm for a complete listing). This dissertation research is an analysis of the magmatic, geochemical and tectonic effects of one of these interactions between these two fundamentally different tectonomagmatic features. The geographic area in this study is the Juan de Fuca Ridge where it overlies the Cobb Hotspot in the northeast Pacific, about 400 km west of the North American coast.

The morphology of the Axial Segment of the Juan de Fuca Ridge has been acutely affected by the presence of the Cobb hotspot. It has shallow bathymetry and an inflated appearance, standing much higher than the other segments on the ridge (Figure 1). It is also dominated by constructional volcanic features, a morphology that is very different from the common tectonic features found on the other Juan de Fuca segments. These observations suggest that the hotspot

Figure 1-1. Perspective view of the central portion of the Juan de Fuca Ridge. The Axial Segment is the linear ridge bisected by Axial Seamount, the large edifice near the center of the image. Axial Seamount has a large (3 x 8 km) caldera and its summit is about 1415 meters below sea level. Brown Bear Seamount is the previous volcanic center built by the Cobb hotspot. The Vance Segment of the Juan de Fuca Ridge extends toward the south, and the CoAxial Segment extends toward the north. Multibeam sonar imagery from Pacific Marine Environment Laboratory (PMEL), courtesy of Robert Embley.

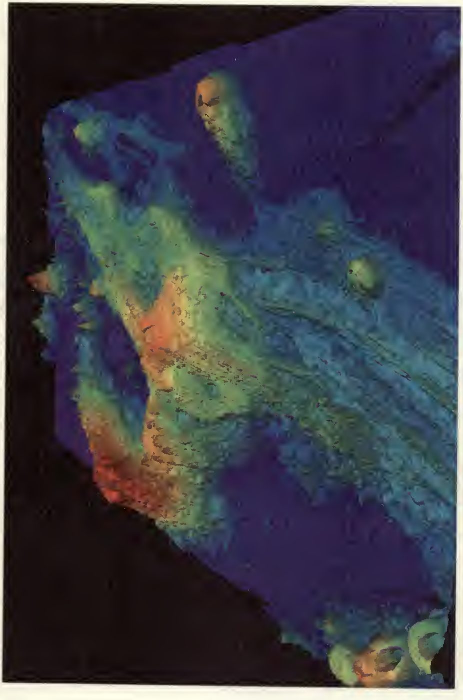

magmas have infiltrated the mid-ocean ridge magmatic system, possibly mixing with indigenous Axial Segment magmas. In chapter 2, the results of an effort to elucidate the magmatic consequences of the ridge hotspot interaction are presented, using the major element, trace element, and radiogenic isotope compositions of rock samples collected from along the Axial Segment. Comparisons with the geochemical characteristics of the other ridge segments show the effects of the hotspot on the Axial Segment lavas. An analysis of spatial geochemical trends along the segment has clarified the importance of magmatic mixing, migration, and eruption processes in this ridge-hotspot interaction.

The Axial Segment has an asymmetrical cross-sectional profile, with the shallowest bathymetry on its eastern side, and the most recent lava flows, freshest-looking basalts, and thinnest sediment cover are also found on the eastern side of the segment. These observations suggest that the Axial Segment is not operating as a normal, symmetrically spreading mid-ocean ridge. In chapter 3, evidence is presented for the "capture" of the segment by the Cobb hotspot, which has effectively arrested its northwesterly migration for at least the past 0.4 my. This process is also occurring at Iceland, where westward migration of a portion of the Mid-Atlantic Ridge has been halted by the Iceland hotspot (Hardarson et al., 1997). With an understanding of the spatial variability in eruptive ages on the Axial Segment caused by ridge capture, geochemical differences between the younger lavas from the east side and older lavas from the west side of the segment are examined.

Chapter 4 is an investigation of the anomalous geochemistry of the Cobb hotspot, which has created the Cobb-Eickelberg (C-E) seamount chain. The chain extends from Axial Seamount, the current locus of the hotspot, to the 33 Ma Patton Seamount near the Aleutian Trench (Keller et al., 1997). ^{40}Ar-^{39}Ar and K-Ar ages from volcanoes in the C-E chain show a clear progression from Axial Seamount to the northwest, consistent with plate motion vectors for the north Pacific and a fixed hotspot plume origin for the chain (Karsten and Delaney, 1989). The C-E chain exhibits the temporal and spatial characteristics of other hotspots, but its lavas do not have typical ocean island basalt (OIB) isotopic or incompatible trace element characteristics (Desonie and Duncan, 1990). C-E basalts have a modest enrichment in LREE, Sr, and K, distinguishing them from the Juan de Fuca Ridge (See Chapter 2), but they fall within global MORB geochemical ranges. The hypothesis of deep mantle plume origins for hotspots is largely supported by the enriched isotopic and trace element geochemistry of OIB relative to MORB (Schilling, 1973; Hart et al. 1973). A fixed, deep mantle plume with the geochemical characteristics of MORB presents a vexing problem in light of the hotspot geochemical paradigm.

CHAPTER 2

MAGMATIC EFFECTS OF THE INTERACTION OF THE JUAN DE FUCA RIDGE WITH THE COBB HOTSPOT

Regional Geology

Axial Seamount is located on the Juan de Fuca Ridge, approximately 400 km west of the western North American coast, and is the volcanic edifice currently being built by the Cobb hotspot. The volcano is associated with a linear system of "rift zones" that extend about 50 km to the north and south from its flanks. These comprise the northern and southern halves of the Axial Segment (a.k.a the Axial Seamount or Axial Volcano Segment; Hammond and Delaney, 1985; Johnson and Holmes, 1989; Embley et al., 1990), one of seven ridge segments that together comprise the Juan de Fuca Ridge (JdFR) system (Figure 2-1). The north and south rift zones and Axial Seamount will collectively be referred to as the Axial Segment in this dissertation.

Axial Seamount rises to about 2100 m above the surrounding seafloor and its summit shallows to about 1415 meters below sea level. With a basal diameter of about 30 km, Axial has dimensions that are similar to the subareal portion of Kauai in the Hawaiian Islands. To the northeast of the caldera, the flank of the volcano drops precipitously from about 1400 m down to 2300 m depth in the Helium Basin over a distance of less than 2 km. Side-scan and Sea Beam sonar surveys have shown that Axial Seamount has a unique morphology, with a 3 x 8

Figure 2-1. The 500-km-long Juan de Fuca Ridge is divided into seven segments (labeled in the inset), and the Axial Segment directly overlies the Cobb hotspot. The Axial Segment is in an overlapping relationship with the neighboring Vance and CoAxial Segments. The outline of Axial Seamount is denoted by the 1600 m isobath contour, and shows the approximate position of the change from contours that are concentric around the seamount to those that are linear and parallel to the trend of the ridge. Locations of basalt samples from the NeMO cruises that have been geochemically analyzed are denoted with a '+' symbol.

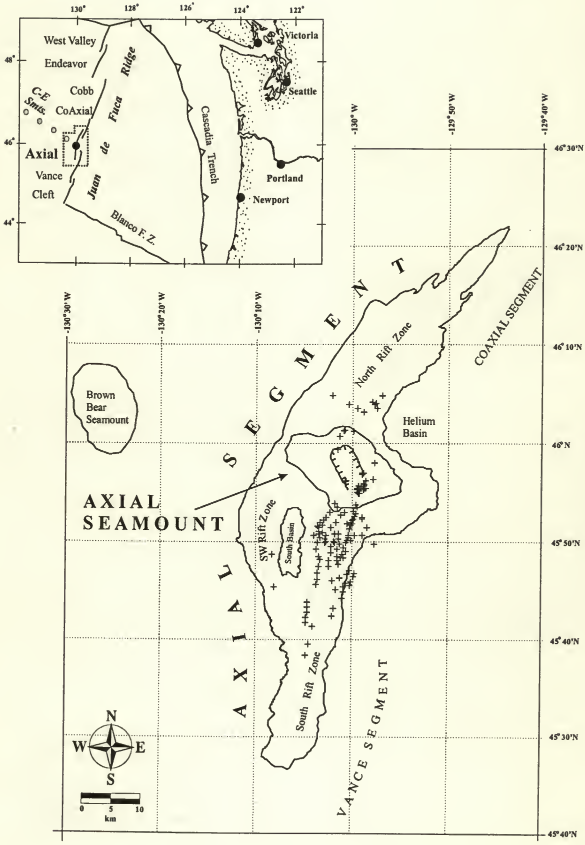
130°
128°
126°
124°
122°
48°
46°
44°
West Valley
Endeavor
Cobb
CoAxial
C-E Smts.
Axial
Vance
Cleft
Juan de Fuca Ridge
Blanco F. Z.
Cascadia Trench
Victoria
Seattle
Portland
Newport
-130° W
-129°50' W
-129°40' W
46°30'N
46°20'N
46°10'N
46°N
45°50'N
45°40'N
45°30'N
45°40'N
-130°30' W
-130°20' W
-130°10' W
AXIAL SEGMENT
COAXIAL SEGMENT
VANCE SEGMENT
North Rift Zone
Helium Basin
Brown Bear Seamount
AXIAL SEAMOUNT
SW Rift Zone
South Basin
South Rift Zone
N
W
E
S
0
5
10
km

km, roughly rectangular caldera that opens to the southeast (Embley et al., 1990). The northeasterly trend of volcanic structures in the rift zones and the northwesterly trend of the caldera's long axis give the system a sigmoidal appearance in map view, similar to Long Valley Caldera in California. The en-echelon offset between the north and south rift zones that occurs across the caldera may be due to an overlapping spreading center offset (Embley et al., 1990).

The Cobb hotspot has produced the major NW-SE-trending Cobb-Eickelberg (C-E) seamount chain in the north Pacific (Smoot, 1985; Karsten and Delaney, 1989; Desonie and Duncan, 1990), which extends from Axial Seamount to the 33-million-year-old Patton Seamount near the Aleutian Trench (Keller et al., 1997), and is roughly parallel to the trend of the Hawaiian chain. Axial Seamount is connected by a low saddle to the next volcano in the chain to the northwest, Brown Bear Seamount. The magmatic activity of the hotspot has apparently been variable over time, with the comparatively smaller Anger, Sloth, Gluttony, and Lust seamounts created during a period of reduced magmatic output between about 2.5 and 4.5 Ma, and larger seamounts reflecting more robust magmatic activity over the past 2.5 Ma (Desonie and Duncan, 1986; Karsten and Delaney, 1989). Son of Brown Bear and Thompson Seamounts, located to the east of Axial Seamount on the Juan de Fuca Plate, may have formed off-axis during periods of higher magmatic output of the Cobb hotspot as the ridge approached it (Desonie and Duncan, 1986; Karsten and Delaney, 1989).

However, a 3 Ma date for a sample from Thompson Seamount (Karsten and Delaney, 1989) indicates that it was formed during the presumed period of reduced activity.

The JdFR comprises the central 490 km of the boundary between the Pacific and Explorer-Juan de Fuca-Gorda plates. Axial Seamount lies near its center and is the shallowest portion of it (Figure 2-2). The region was part of a classic mid-ocean ridge magnetic anomaly study (Raff and Mason, 1961; Vine and Matthews, 1963), and the tectonic evolution and spreading rates of the ridge have been studied in detail (Hey and Wilson, 1982; Wilson and Hey, 1984; Wilson, 1993). The JdFR has a strike of about 20° and intersects the Blanco fracture zone at its southern terminus, which offsets the spreading axis by ~400 km from the Gorda Ridge. The JdFR is bounded to the north by a complex triple junction with the Sovanco fracture zone and left-lateral Nootka fault (Hyndman et al., 1979; Riddihough, 1984).

The number and names of the individual second-order ridge segments of the JdFR have changed over time with improvements in mapping, and descriptions of the segments and the ridge in general have been published in previous studies (Delaney et al., 1981; Embley and Chadwick, 1994; Embley et al., 2000; Johnson and Embley, 1990; Johnson and Holmes, 1989; Kappel and Ryan, 1986; Malahoff et al., 1982; Smith et al., 1994; Van Wagoner and Leybourne, 1991). The seven segments most recently identified are, from south to north (previously used names of segments are given in parenthesis for comparison

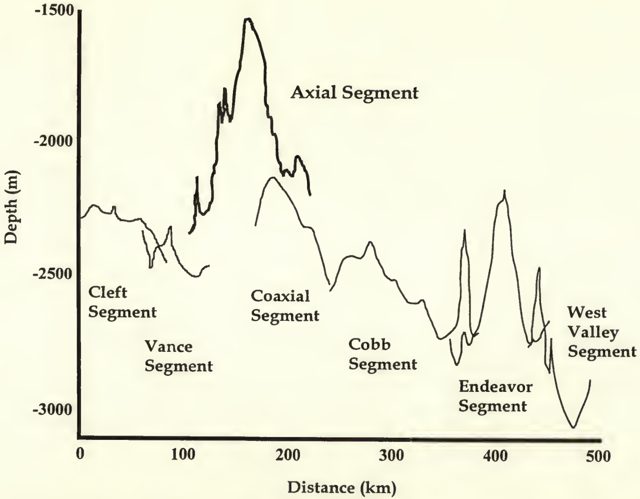

Figure 2-2. Bathymetric profiles along the Juan de Fuca Ridge segments. The Axial Segment is the shallowest of the entire ridge, attesting to the oversupply of magmas to the ridge from the hotspot, and allowing the hotspot and MORB-source magmas to mix.

with older papers): Cleft (Southern Symmetrical Ridge), Vance (Segment "B" or the Shingle Ridge Segment), Axial (Axial Seamount or Axial Volcano), CoAxial (part of the Northern Symmetrical Ridge and later considered part of the Cobb Segment), Cobb (part of the Northern Symmetrical Ridge), Endeavor and West Valley (Figure 2-1). Offsets between these segments are generally characterized by overlapping spreading centers, with the ends of each of the segments curving toward each other. The JdFR is a medium spreading-rate system, with a full rate of about 6 cm/year (Vine and Wilson, 1965; Johnson and Embley, 1990). The entire plate boundary system is migrating to the NW at 3.1 cm/yr (Desonie and Duncan, 1986; Karsten and Delaney, 1989).

The age of the interaction between the JdFR and Cobb hotspot is constrained by the offset location of the Axial Segment in the paleomagnetic lineation pattern. The center of the Brunhes normal-polarity crust pattern lies about 15 km to the east of the Axial Segment, collinear with the Vance and CoAxial segment trends (Tivey and Johnson, 1990). This indicates that active spreading linked the Vance and CoAxial segments in early Brunhes time, but ceased when the section of ridge between them was abandoned and spreading moved westward to the Cobb hotspot, creating the Axial Segment between 0.2 and 0.7 Ma (Delaney et al., 1981; Karsten and Delaney, 1989; Tivey and Johnson, 1990). This ridge "jump" trapped small areas of Matuyama-age crust (e.g. Helium Basin) between the abandoned and current spreading ridges. A study of ridge morphological and bathymetric characteristics and age distribution of basalts on the Axial Segment suggest that the segment has been captured by the hotspot (see Chapter 3), essentially arresting its migration in a situation similar to the capture of the Mid-Atlantic Ridge by the Iceland hotspot.

Morphological Characteristics of the Axial Segment

The general characteristics of the Axial Segment have been described in previous studies based on side-scan sonar imagery (Delaney at al., 1981; Embley et al., 1990; Johnson and Holmes, 1989; Johnson and Embley, 1990). The gross bathymetric and detailed morphologic characteristics of the Axial Segment are distinct from the rest of the JdFR segments due to the presence of the Cobb hotspot. The segment is, however, an integral part of the JdFR spreading system and not simply a volcanic rift system similar to the one associated with Kilauea volcano in Hawaii (Delaney et al., 1981; Hammond and Delaney, 1985; Delaney, 1986; Johnson and Holmes, 1989). It accommodates spreading in the 60-km gap between the southern end of the CoAxial segment and the northern end of the Vance segment (Figure 2-1), and it overlaps these segments in the manner of an overlapping spreading center (Embley et al., 2000). The complex interaction between seafloor spreading and hotspot volcanism has led to the creation of the ridge-centered Axial Seamount, and elongate, inflated rift zones that have the highest-standing bathymetry on the entire JdFR, with average depths that are 250-750 m shallower than the other segments (Figure 2-2). The other JdFR segments are characterized by a predominance of tectonic features typical of medium spreading rate ridges (e.g. Karsten et al., 1986; Johnson and Holmes, 1989; Van Wagoner and Leybourne, 1991, Smith et al., 1994; Embley et al., 2000), but the Axial Segment is dominated by constructional volcanic features (Appelgate, 1990). It has a corrugated appearance, composed of parallel-trending sets of thin, linear ridges that appear to be dike-fed volcanic constructs. They are typically about 300 to 500 m wide, up to 50 m high, and can be up to 15 km long. Interspersed among this linear pattern are small (typically <1 km) seamounts that represent more focused, localized higher effusion, and these features are more prevalent closer to the northern and southern ends of the segment.

The linear ridges are larger and more numerous close to Axial Seamount, suggesting that they are fed by lateral dike intrusion from the large magma chamber detected using seismic tomography under the seamount (West et al., 2001). Lateral migration of magmas along the segment from the vicinity of the hotspot is also implied by the locations of waterborne T-wave foci generated by the eruption of Axial Seamount during January of 1998, detected by the Sound Surveillance System (SOSUS) hydrophone network (Dziak and Fox, 1998, 1999). The activity migrated progressively southward from Axial's caldera ~50 km into the South Rift Zone during the first few days of the 11-day period of activity (Embley et al., 1999). Similar migration of seismic activity during eruptive events has been observed in Icelandic and Hawaiian diking events (Dziak and Fox, 1998). The bathymetric and morphologic features of the Axial Segment suggest an "oversupply" and lateral migration of magmas from the hotspot focus at

Axial Seamount, along the entire length of the ridge segment; a hypothesis that should be testable using petrologic and geochemical methods.

The January, 1998 eruption produced extensive lava flows to the southeast of the caldera from at least two collinear fissure sources. The geological, hydrothermal, and biological effects of this eruption have been the focus of NOAA's New Millennium Observatory (NeMO) project (http://www.pmel.noaa.gov/vents/nemo/index.html). The field work in support of this research has included high-density rock sampling using wax corers and the Remotely Operated Platform for Ocean Science (ROPOS) submersible. In this paper we discuss the results of this geologic research, in an effort to elucidate the magmatic consequences of the Cobb-JdFR interaction using the major element, trace element, and radiogenic isotopic compositions of rock samples collected on the Axial Segment. Comparisons with the geochemical characteristics of the other segments on the JdFR allow us to better constrain the effects of the hotspot on any Axial Segment MORB lavas, and analysis of spatial geochemical trends has improved our understanding of mixing, migration, and eruption processes that have occurred in response to this ridge-hotspot interaction.

Sample Collection and Petrographic Analyses

A total of 254 rock samples were collected on Axial Seamount, the Axial Segment rift zones, and the Cleft and Vance Segments of the JdFR during the 1998-2002 NeMO cruises (Figure 2-1). Samples were collected mostly by wax coring on the Axial Segment, and the ROPOS submersible was used primarily in the Axial Seamount caldera region, particularly around the 1998 eruption area. The wax core samples were collected in a high density grid on the ridge within 25 km of Axial Seamount, allowing for trends and small-scale differences in geochemistry to be identified. An additional 28 samples were collected in the study area in 1986 by the Pisces IV submersible, and 42 samples from the northern caldera and Axial Seamount flanks were collected using a grab-sampler with integrated video camera (TV-grab) during the 1996 cruise of RV Sonne, and geochemical analyses of these supplement the study where noted. Natural glass samples were analyzed by electron microprobe, X-ray fluorescence spectroscopy, and thermal ionization mass spectrometry for major element, trace element, and isotopic compositions (See Appendix for analytical methods). Thin-sections of representative samples were also petrographically examined to provide phase chemical information.

Basalt flow morphologies in the Axial caldera region include sheet flows, chaotic jumbled flows, pillow basalts, and lobate flows (Embley et al., 1990). The freshest samples have thick (>1 cm) glass rinds that are friable and easily exfoliated, while progressively older samples have thinner rinds and increasing Mn alteration. Most of the basalt samples collected in the Axial Seamount caldera and on the flanks are sparsely to moderately phyric, (<5%) and have mineral assemblages dominated by plagioclase with rare olivine phenocrysts. The plagioclase phenocrysts commonly occur as clots of crystals with dimensions up to several mm. Samples from a small cone in the central part of the caldera (Pisces sample XL-2087-5) are highly plagioclase phyric (~40%) with minor olivine. Complex zoning and disequilibrium compositions of some plagioclase and more rare, partially resorbed olivine crystals in basalts retrieved from the caldera indicate magma mixing has taken place. Most samples from the adjacent ridge portion of the Axial Segment are moderately plagioclase phyric (up to 15%), and the abundance of crystals generally increases with distance from Axial Seamount. Plagioclase phenocrysts are typically less than 1 mm and euhedral to subhedral. Microphenocrysts and microlites of olivine, plagioclase, clinopyroxene and opaques commonly occur in the groundmass. Lavas typically have a variolitic texture, with varioles composed of plagioclase and clinopyroxene. Most of the basalts in the study area are sparsely vesicular (< 5% by volume), although four andesite samples collected in the north rift zone and one basalt from the caldera region (R494-3) are moderately to highly vesicular. One basalt sample containing a small gabbroic (olivine-plagioclase-clinopyroxene) xenolith was collected just to the south of the Axial Seamount caldera (R483-6).

Major Element Geochemistry

Major and minor element compositions of 226 glass samples collected on Axial Seamount and the adjacent rift zones were analyzed by electron microprobe and are presented in Table 2-1 and plotted in Figure 2-3. The basalts exhibit typical tholeiitic differentiation trends, with increasing concentrations of

Table 2-1. Major element concentrations (wt. %) for Axial Segment samples, analyzed by electron microprobe[1].

Sample	Latitude	Latitude	SiO_2	Al_2O_3	TiO_2	FeO	MnO	MgO	CaO	K_2O	Na_2O	P_2O_5	Total
98-RC-01	-129.9970	45.8922	50.3	14.4	1.52	10.7	0.21	7.15	11.7	0.19	2.95	0.14	99.3
98-RC-02	-129.9758	45.8535	50.0	14.1	1.65	11.3	0.21	6.94	11.6	0.23	2.96	0.15	99.0
98-RC-03	-130.0130	45.8287	50.0	14.1	1.59	11.1	0.21	7.00	11.6	0.20	3.03	0.16	99.0
98-RC-04	-130.0117	45.8325	50.2	14.2	1.61	11.2	0.20	7.10	11.7	0.19	2.86	0.15	99.4
98-RC-05	-130.0053	45.8327	49.9	14.9	1.37	10.2	0.20	7.66	11.9	0.14	2.82	0.12	99.2
98-RC-06	-130.0097	45.8363	50.0	14.1	1.59	11.1	0.21	7.02	11.6	0.21	2.96	0.16	99.1
98-RC-07	-130.0597	45.7867	50.0	14.0	1.57	11.2	0.21	6.99	11.8	0.16	2.98	0.15	99.0
98-RC-09	-130.0575	45.8012	50.2	14.2	1.58	11.1	0.23	7.10	11.7	0.17	2.99	0.16	99.4
98-RC-10	-129.9633	45.9615	50.1	14.8	1.41	10.5	0.20	7.49	11.6	0.16	2.83	0.14	99.2
98-RC-11	-130.0062	45.8505	50.1	14.3	1.52	10.6	0.20	7.16	11.9	0.20	2.94	0.13	99.0
98-RC-12	-130.0088	45.8400	50.2	14.2	1.63	11.2	0.22	6.98	11.6	0.20	3.02	0.18	99.5
98-RC-13	-130.0268	45.8440	50.1	14.1	1.50	10.9	0.21	7.15	11.8	0.19	2.86	0.15	98.9
98-RC-15	-130.0318	45.8943	50.3	14.3	1.60	11.2	0.22	6.92	11.7	0.20	2.86	0.16	99.5
98-RC-16	-130.0258	45.7923	50.2	14.0	1.48	11.3	0.20	7.08	11.7	0.15	2.87	0.14	99.1
98-RC-17	-130.0283	45.7983	50.4	13.9	1.57	11.5	0.21	6.95	11.6	0.16	2.95	0.15	99.3
98-RC-18	-130.0193	45.8087	50.0	14.0	1.65	11.3	0.21	6.91	11.6	0.21	3.07	0.15	99.1
98-RC-21	-130.0813	45.6367	48.2	16.6	1.31	10.1	0.18	8.76	11.2	0.09	2.75	0.10	99.4
98-RC-22	-130.0467	45.8707	50.4	14.1	1.63	11.3	0.22	6.84	11.7	0.20	2.95	0.17	99.4
98-RC-23	-130.0417	45.8803	50.3	14.3	1.50	10.9	0.21	7.17	11.9	0.19	2.87	0.13	99.6
98-RC-24	-130.0380	45.8527	50.1	14.0	1.62	11.5	0.22	6.85	11.5	0.21	3.00	0.16	99.1
98-RC-26	-130.0485	45.8343	48.7	16.3	1.07	9.9	0.20	8.53	11.8	0.11	2.56	0.11	99.4
98-RC-27	-130.0258	45.8342	49.9	14.2	1.53	10.9	0.21	7.18	11.9	0.17	2.98	0.14	99.2
98-RC-28	-130.0250	46.0075	50.6	14.5	1.52	10.5	0.20	7.09	11.3	0.24	3.07	0.17	99.2
98-RC-30	-130.0375	45.8212	49.9	13.8	1.66	11.7	0.23	6.71	11.5	0.20	3.01	0.14	98.9
98-RC-31	-130.0277	45.8167	50.0	14.3	1.71	11.8	0.23	6.58	11.1	0.24	3.17	0.18	99.3
98-RC-32	-130.0130	45.8133	50.1	14.2	1.62	11.0	0.21	7.13	11.9	0.20	2.93	0.16	99.4
98-RC-33	-130.0315	45.8437	50.2	13.9	1.65	11.5	0.22	6.84	11.7	0.20	2.92	0.15	99.2
98-RC-34	-130.0475	45.8403	50.0	13.7	1.74	11.9	0.22	6.54	11.3	0.23	3.03	0.18	99.0
98-RC-35	-130.0113	45.8612	50.2	14.3	1.45	10.6	0.20	7.32	12.0	0.17	2.83	0.13	99.1
98-RC-36	-129.9638	45.8263	49.5	15.2	1.34	10.6	0.20	7.69	12.0	0.14	2.80	0.12	99.5
98-RC-39	-130.0028	45.8608	50.1	14.4	1.51	10.5	0.20	7.27	11.9	0.19	2.85	0.14	99.1

[1] Analyzed by the U.S. Geological Survey, Denver, Colorado.

Table 2-1. Continued.

Sample	Latitude	Latitude	SiO_2	Al_2O_3	TiO_2	FeO	MnO	MgO	CaO	K_2O	Na_2O	P_2O_5	Total
98-RC-40	-130.0700	45.8400	50.1	13.9	1.67	11.6	0.22	6.79	11.4	0.18	3.13	0.16	99.2
98-RC-41	-130.0290	45.8893	50.4	14.4	1.54	10.8	0.21	7.21	11.8	0.19	2.91	0.15	99.6
98-RC-42	-129.9965	46.0227	50.1	14.3	1.62	10.8	0.22	7.14	11.7	0.21	2.97	0.18	99.3
98-RC-43	-130.0475	45.8310	50.3	13.9	1.65	11.4	0.23	6.88	11.4	0.19	2.98	0.15	99.2
98-RC-44	-130.0500	45.8275	50.2	13.9	1.59	11.5	0.23	6.86	11.4	0.18	2.99	0.15	99.0
98-RC-45	-130.0602	45.8053	49.9	14.0	1.59	11.3	0.22	6.97	11.7	0.21	2.91	0.17	99.0
98-RC-46	-130.0308	45.7483	47.8	17.2	1.01	9.8	0.16	9.27	11.4	0.07	2.52	0.05	99.3
98-RC-47	-129.9828	46.0488	50.0	14.2	1.49	10.8	0.20	7.25	11.9	0.18	2.84	0.13	99.1
98-RC-48	-129.9678	46.0660	50.1	14.1	1.55	11.0	0.22	7.07	11.8	0.20	2.88	0.15	99.1
98-RC-49	-129.9630	46.0623	57.7	12.3	1.79	13.6	0.32	1.82	5.8	0.90	2.29	0.70	97.2
99-RC-50	-130.0000	45.8810	49.5	15.5	1.35	10.0	0.17	8.05	12.1	0.12	2.85	0.12	99.7
99-RC-51	-130.0150	45.8790	50.1	14.1	1.59	11.1	0.22	6.93	11.7	0.17	2.88	0.16	99.1
99-RC-52	-130.0210	45.8760	49.9	14.5	1.50	10.9	0.21	7.15	12.1	0.15	2.88	0.15	99.3
99-RC-53	-130.0300	45.8620	49.9	14.4	1.53	10.9	0.21	7.40	12.0	0.15	2.85	0.15	99.6
99-RC-54	-130.0780	45.6560	48.7	16.9	1.25	9.3	0.17	8.47	11.8	0.09	2.78	0.09	99.5
99-RC-55	-130.0720	45.6870	50.0	14.1	1.69	11.4	0.22	6.78	11.9	0.18	2.91	0.13	99.2
99-RC-56	-130.0820	45.6920	50.0	13.8	1.77	12.3	0.23	6.35	11.3	0.18	3.13	0.17	99.3
99-RC-57	-130.0820	45.7010	50.0	13.7	1.79	12.3	0.22	6.37	11.4	0.18	3.14	0.17	99.3
99-RC-58	-130.0640	45.7570	49.9	14.0	1.71	11.6	0.24	6.71	11.8	0.18	2.97	0.16	99.2
99-RC-59	-130.0630	45.7660	50.0	14.1	1.62	11.3	0.20	6.82	11.8	0.16	3.01	0.14	99.2
99-RC-60	-130.0630	45.7770	49.9	13.9	1.65	11.4	0.21	6.70	11.9	0.19	2.99	0.16	98.9
99-RC-61	-130.1380	45.7530	50.0	13.8	1.64	11.4	0.22	6.70	11.5	0.19	2.99	0.17	98.7
99-RC-62	-130.0510	45.8670	50.1	13.7	1.72	11.4	0.21	6.64	11.5	0.21	2.95	0.18	98.6
99-RC-63	-130.0530	45.8570	49.9	14.0	1.57	11.0	0.20	6.94	12.0	0.18	2.88	0.15	98.7
99-RC-64	-130.0800	45.7270	50.0	13.8	1.71	11.4	0.23	6.62	11.6	0.21	2.97	0.19	98.7
99-RC-65	-130.0790	45.7190	50.0	13.8	1.73	11.7	0.23	6.51	11.7	0.20	2.94	0.16	99.0
99-RC-66	-130.0800	45.7090	50.2	14.0	1.51	11.0	0.20	6.91	11.9	0.13	2.90	0.13	98.8
99-RC-67	-130.1410	45.8080	49.7	14.2	1.71	10.8	0.21	6.85	11.9	0.22	3.06	0.19	98.8
99-RC-68	-130.0580	45.8360	49.9	13.7	1.70	11.5	0.22	6.73	11.6	0.20	2.92	0.18	98.7
99-RC-69	-130.0610	45.8420	50.0	14.3	1.51	10.7	0.21	7.20	12.2	0.19	2.67	0.13	99.1
99-RC-70	-130.0190	45.7340	50.0	14.4	1.45	10.5	0.21	7.21	12.2	0.13	2.80	0.14	98.9
99-RC-71	-130.0180	45.7440	50.1	14.2	1.51	10.7	0.22	7.04	12.2	0.14	2.82	0.14	99.1

Table 2-1. Continued.

Sample	Latitude	Latitude	SiO_2	Al_2O_3	TiO_2	FeO	MnO	MgO	CaO	K_2O	Na_2O	P_2O_5	Total
99-RC-72	-130.0140	45.7600	49.0	14.1	1.59	11.0	0.20	6.97	11.9	0.17	2.89	0.14	98.0
99-RC-73	-130.0070	45.7550	49.4	14.3	1.45	10.4	0.21	7.28	12.2	0.17	2.73	0.14	98.4
99-RC-74	-130.0170	45.7530	49.5	14.1	1.58	11.1	0.22	6.80	12.0	0.17	2.92	0.17	98.5
99-RC-75	-130.0120	45.7740	49.9	14.1	1.64	11.2	0.22	6.61	12.0	0.18	2.94	0.15	98.9
99-RC-76	-130.0010	45.7700	49.5	14.3	1.48	10.4	0.21	7.21	12.2	0.18	2.72	0.15	98.3
99-RC-77	-130.0070	45.7810	49.4	14.0	1.62	11.2	0.21	6.87	11.9	0.17	2.94	0.16	98.5
99-RC-78	-129.9990	45.7760	49.5	14.3	1.48	10.4	0.21	7.25	12.2	0.18	2.76	0.15	98.3
99-RC-79	-130.0050	45.7620	48.8	14.3	1.44	10.3	0.21	7.31	12.2	0.17	2.72	0.15	97.7
99-RC-81	-130.0230	45.7690	49.9	14.2	1.38	10.3	0.19	7.40	12.6	0.12	2.81	0.13	99.0
99-RC-82	-130.0370	45.7630	47.8	16.9	1.17	9.6	0.19	8.82	11.8	0.07	2.68	0.09	99.1
99-RC-83	-130.0550	45.8460	49.8	14.1	1.55	10.7	0.22	7.10	12.2	0.17	2.85	0.15	98.8
99-RC-84	-130.0600	45.8470	49.8	14.1	1.54	10.9	0.22	7.06	12.0	0.18	2.86	0.15	98.9
99-RC-85	-130.0600	45.8530	50.0	14.0	1.55	10.8	0.20	7.09	12.0	0.17	2.85	0.15	98.8
99-RC-86	-130.0430	45.7870	49.9	13.7	1.73	11.8	0.22	6.46	11.5	0.20	3.09	0.19	98.8
99-RC-87	-130.0430	45.7980	49.9	13.7	1.76	11.9	0.24	6.46	11.5	0.19	3.12	0.19	98.9
99-RC-88	-130.0390	45.8110	49.9	13.9	1.59	11.0	0.20	6.97	11.8	0.17	2.95	0.16	98.8
99-RC-89	-130.0240	45.8250	50.1	13.9	1.64	11.1	0.20	6.75	11.8	0.20	3.01	0.18	98.8
99-RC-90	-130.0350	45.8300	49.8	13.9	1.59	11.1	0.21	7.25	11.7	0.17	3.01	0.13	98.9
99-RC-91	-130.0280	45.8050	49.7	14.0	1.54	10.7	0.21	7.41	12.1	0.14	3.00	0.14	98.9
99-RC-92	-130.0210	45.8020	49.8	14.1	1.54	10.7	0.21	7.36	11.9	0.18	2.84	0.15	98.7
99-RC-93	-130.0170	45.8030	49.8	14.1	1.52	10.6	0.20	7.08	11.9	0.17	2.92	0.14	98.5
99-RC-97	-130.0370	45.7030	47.9	16.7	0.98	9.6	0.17	9.37	11.6	0.04	2.58	0.05	99.0
99-RC-98	-130.0340	45.7160	48.6	16.1	1.40	9.6	0.18	8.13	11.8	0.08	3.01	0.09	99.1
99-RC-99	-129.9620	46.0640	58.3	12.5	1.57	12.9	0.29	1.56	5.4	0.90	3.67	0.63	97.7
99-RC-100	-129.9600	46.0560	55.1	12.8	1.99	13.2	0.29	2.26	6.1	0.84	4.27	0.68	97.5
99-RC-101	-129.9520	46.0770	53.8	12.1	2.19	14.6	0.32	2.40	6.5	0.71	4.12	0.96	97.7
99-RC-102	-130.0370	46.0770	49.7	14.1	1.52	10.6	0.21	7.08	12.0	0.15	2.88	0.13	98.3
99-RC-105	-130.0620	45.8550	49.6	14.3	1.47	10.3	0.20	7.24	11.9	0.15	2.84	0.12	98.2
99-RC-106	-130.0580	45.8620	49.5	14.0	1.53	10.7	0.20	7.03	12.0	0.17	2.91	0.14	98.1
99-RC-107	-130.0620	45.8290	49.7	14.2	1.53	10.5	0.21	7.15	12.2	0.16	2.93	0.13	98.7
99-RC-108	-130.0640	45.8170	50.0	13.9	1.65	11.2	0.22	6.82	11.6	0.19	3.04	0.13	98.7
00-RC-113	-129.9825	45.9165	49.6	14.5	1.51	10.5	0.18	7.57	12.0	0.19	2.89	0.15	99.1

Table 2-1. Continued.

Sample	Latitude	Latitude	SiO_2	Al_2O_3	TiO_2	FeO	MnO	MgO	CaO	K_2O	Na_2O	P_2O_5	Total
00-RC-116	-130.0317	45.8283	49.9	14.0	1.71	11.6	0.22	6.88	11.7	0.21	2.94	0.17	99.2
00-RC-117	-130.0168	45.8190	50.0	14.4	1.54	10.6	0.21	7.32	12.1	0.20	2.87	0.16	99.3
00-RC-118	-129.9684	45.9167	49.7	14.6	1.48	10.2	0.20	7.27	12.2	0.18	2.84	0.15	98.9
00-RC-119	-129.9928	46.0562	47.0	17.2	1.32	8.9	0.17	8.58	11.7	0.11	2.81	0.12	98.0
00-RC-120	-130.0093	46.0619	49.3	15.5	1.33	9.7	0.21	7.80	12.2	0.13	2.78	0.11	99.1
00-RC-122	-129.9848	45.8403	48.2	16.7	1.38	9.2	0.18	8.06	11.9	0.13	2.96	0.12	98.8
00-RC-123	-129.9983	45.8398	48.8	15.8	1.29	9.7	0.18	8.04	12.1	0.12	2.72	0.11	98.9
R460-04	-129.9855	45.9438	50.0	14.4	1.51	10.7	0.20	7.32	12.1	0.18	2.97	0.15	99.5
R460-06	-129.9817	45.9333	50.0	14.5	1.52	10.6	0.21	7.35	12.1	0.18	2.98	0.15	99.6
R461-16	-129.9883	45.9227	50.0	14.4	1.52	10.6	0.21	7.32	12.1	0.19	2.96	0.15	99.5
R461-25	-129.9798	45.9270	50.1	14.9	1.23	9.9	0.20	7.96	12.1	0.12	2.69	0.10	99.3
R461-26	-129.9798	45.9270	50.0	14.4	1.47	10.4	0.20	7.54	11.8	0.19	2.89	0.14	99.1
R462-08	-129.9823	45.9333	49.9	14.5	1.52	10.7	0.21	7.34	12.0	0.19	2.98	0.14	99.5
R462-15	-129.9818	45.9333	50.0	14.5	1.55	10.7	0.21	7.34	12.0	0.19	2.96	0.14	99.6
R464-06	-129.9818	45.9333	50.1	14.6	1.53	10.7	0.20	7.30	12.0	0.18	2.94	0.14	99.6
R465-01	-129.9862	45.8693	50.1	14.2	1.53	10.9	0.19	7.04	11.7	0.20	2.98	0.14	99.1
R465-02	-129.9863	45.8695	50.2	14.2	1.57	10.9	0.20	7.05	11.6	0.20	2.97	0.14	99.0
R467-01	-130.0163	46.0188	50.1	14.4	1.50	10.6	0.20	7.38	11.7	0.19	2.92	0.13	99.0
R471-04	-130.0137	45.9337	49.9	14.6	1.52	10.7	0.19	7.29	12.1	0.19	2.97	0.14	99.6
R473-06	-129.9848	45.9455	50.0	14.5	1.52	10.7	0.21	7.33	12.1	0.18	2.99	0.13	99.6
R473-18	-129.9822	45.9333	50.0	14.5	1.51	10.7	0.20	7.34	12.1	0.18	2.96	0.14	99.5
R473-21	-129.9830	45.9287	49.9	14.5	1.53	10.7	0.22	7.31	12.1	0.19	2.95	0.15	99.6
R474-02	-129.9780	45.9330	50.0	14.5	1.45	10.3	0.19	7.51	11.8	0.20	2.89	0.15	99.0
R474-03	-129.9815	45.9360	50.2	14.4	1.50	10.7	0.18	7.11	11.7	0.20	2.95	0.15	99.0
R476-02	-129.9847	45.9460	50.0	14.3	1.47	10.7	0.20	7.35	11.7	0.19	2.88	0.16	98.9
R476-07	-129.9850	45.9463	50.1	14.5	1.51	10.6	0.21	7.32	12.0	0.19	2.95	0.15	99.6
R478-08	-129.9815	45.9358	50.0	14.5	1.55	10.7	0.21	7.26	12.0	0.20	2.99	0.16	99.6
R479-15	-130.0140	45.9333	49.9	14.6	1.53	10.6	0.22	7.30	12.1	0.19	2.95	0.15	99.6
R483-02	-129.9823	45.9333	49.5	14.3	1.51	10.7	0.20	7.21	12.2	0.18	2.88	0.15	98.7
R483-04	-129.9823	45.9333	49.5	14.2	1.49	10.6	0.20	7.22	12.1	0.19	2.87	0.14	98.7
R483-06	-129.9823	45.9333	49.5	14.2	1.50	10.7	0.20	7.20	12.1	0.18	2.86	0.14	98.6
R484-01	-129.9823	45.9333	49.6	14.3	1.48	10.6	0.20	7.43	12.1	0.18	2.86	0.16	98.9

Table 2-1. Continued.

Sample	Latitude	Latitude	SiO_2	Al_2O_3	TiO_2	FeO	MnO	MgO	CaO	K_2O	Na_2O	P_2O_5	Total
R488-15	-129.9818	45.9334	49.5	14.3	1.48	10.6	0.21	7.17	12.3	0.19	2.85	0.15	98.8
R488-16	-129.9818	45.9334	49.5	14.2	1.51	10.7	0.19	7.17	12.0	0.18	2.90	0.15	98.5
R488-05	-129.9823	45.9333	49.4	14.2	1.50	10.6	0.20	7.16	12.0	0.18	2.87	0.15	98.4
R488-06	-129.9823	45.9333	49.5	14.3	1.53	10.7	0.19	7.19	12.0	0.18	2.88	0.16	98.6
R488-FS	-129.9819	45.9332	49.5	14.3	1.51	10.6	0.20	7.21	12.0	0.18	2.86	0.14	98.5
R491-21	-129.9817	45.9364	50.0	14.6	1.48	10.3	0.18	7.33	12.3	0.19	2.83	0.15	99.3
R491-22	-129.9816	45.9344	50.0	14.6	1.48	10.3	0.19	7.62	12.2	0.18	2.85	0.13	99.5
R491-25	-129.9833	45.9451	49.9	14.5	1.53	10.4	0.19	7.35	12.3	0.18	2.83	0.14	99.3
R492-02	-129.9886	45.9188	49.9	14.4	1.52	10.7	0.20	7.58	12.2	0.18	2.89	0.15	99.7
R492-09	-129.9919	45.9168	49.8	14.5	1.49	10.5	0.19	7.35	12.2	0.18	2.87	0.16	99.2
R492-08	-129.9919	45.9168	49.9	14.5	1.54	10.6	0.19	7.22	12.5	0.18	2.81	0.15	99.5
R492-14	-129.9893	45.9162	49.9	14.4	1.52	10.6	0.20	7.15	12.4	0.17	2.89	0.14	99.3
R493-01	-129.9952	45.9134	50.1	14.5	1.51	10.4	0.18	7.54	12.1	0.18	2.84	0.13	99.4
R494-01	-130.0042	45.8583	50.1	14.3	1.53	10.6	0.19	7.03	12.3	0.18	2.84	0.15	99.2
R494-04	-130.0041	45.8624	50.1	14.4	1.56	10.8	0.20	7.11	11.8	0.18	2.90	0.15	99.3
R494-05	-130.0041	45.8624	50.1	14.5	1.53	10.9	0.19	7.14	11.9	0.18	2.91	0.15	99.5
R494-06	-130.0041	45.8624	50.1	14.4	1.55	10.7	0.18	7.15	12.0	0.19	2.86	0.15	99.3
R494-08	-129.9958	45.8782	50.1	14.5	1.57	10.7	0.21	7.10	12.0	0.18	2.88	0.14	99.4
R494-09	-129.9929	45.8894	50.1	14.5	1.52	10.7	0.19	7.24	12.0	0.18	2.87	0.13	99.4
R495-35	-129.9904	45.9111	50.0	14.4	1.51	10.7	0.20	7.53	11.9	0.18	2.86	0.15	99.5
R495-36	-129.9904	45.9111	49.9	14.5	1.52	10.7	0.20	7.21	12.2	0.18	2.87	0.14	99.4
R496-03	-129.9883	45.9226	50.0	14.5	1.53	10.7	0.20	7.50	12.0	0.18	2.89	0.15	99.6
R496-RU	-129.9840	45.9303	50.0	14.5	1.53	10.8	0.19	7.21	12.1	0.18	2.88	0.14	99.5
R497-12	-130.0272	45.9889	50.1	14.5	1.49	10.4	0.21	7.18	11.7	0.20	3.05	0.16	99.0
R497-20	-130.0163	46.0188	50.0	14.5	1.46	10.5	0.20	7.13	11.9	0.20	3.06	0.16	99.1
R500-06	-129.9833	45.9451	49.8	14.5	1.49	10.4	0.19	7.41	12.1	0.18	2.95	0.15	99.1
R501-10	-129.9823	45.9240	49.8	14.3	1.51	10.6	0.20	7.21	12.1	0.18	2.60	0.15	98.7
R501-11	-129.9823	45.9239	49.7	14.3	1.50	10.5	0.19	7.18	12.2	0.18	2.48	0.15	98.4
R501-12	-129.9876	45.9240	49.5	14.5	1.48	10.2	0.20	7.40	12.2	0.18	2.48	0.14	98.3
R501-13	-129.9886	45.9240	49.7	14.3	1.51	10.7	0.21	7.48	12.0	0.18	2.90	0.15	99.2
R501-14	-129.9886	45.9240	49.6	14.5	1.47	10.4	0.19	7.43	12.1	0.19	2.84	0.16	98.8
R501-16	-129.9922	45.9240	49.6	14.5	1.49	10.4	0.19	7.39	12.2	0.18	2.85	0.15	99.0

Table 2-1. Continued.

Sample	Latitude	Latitude	SiO_2	Al_2O_3	TiO_2	FeO	MnO	MgO	CaO	K_2O	Na_2O	P_2O_5	Total
R501-02	-129.9924	45.9206	49.7	14.6	1.51	10.4	0.19	7.39	12.2	0.19	2.92	0.16	99.2
R501-03	-129.9914	45.9207	49.9	14.5	1.50	10.6	0.20	7.27	12.0	0.18	2.94	0.13	99.2
R501-04	-129.9899	45.9203	49.8	14.4	1.49	10.5	0.20	7.32	12.1	0.18	2.92	0.15	99.1
R501-05	-129.9877	45.9204	49.7	14.4	1.50	10.5	0.19	7.35	12.2	0.18	2.92	0.17	99.1
R501-06	-129.9867	45.9206	49.9	14.4	1.50	10.5	0.19	7.31	11.9	0.18	2.92	0.16	99.0
R501-07	-129.9818	45.9204	49.7	14.4	1.49	10.5	0.19	7.32	12.2	0.18	2.91	0.16	99.0
R501-08	-129.9777	45.9202	49.6	14.6	1.48	10.3	0.21	7.68	12.3	0.19	2.84	0.14	99.3
R501-09	-129.9777	45.9201	49.8	14.3	1.51	10.6	0.21	7.17	12.0	0.18	2.89	0.14	98.8
R502-34	-130.0163	46.0188	49.8	14.4	1.52	10.6	0.19	7.14	12.2	0.19	2.88	0.15	99.1
R543-01	-129.9817	45.9334	49.8	13.7	1.89	11.5	0.22	7.03	10.7	0.22	2.79	0.23	98.2
R543-08	-129.9823	45.9333	49.7	14.6	1.53	10.4	0.21	7.58	12.1	0.19	2.87	0.15	99.4
R545-02	-130.0136	45.9336	48.9	14.5	1.54	10.5	0.20	7.62	12.1	0.18	2.87	0.16	98.6
R545-05	-130.0141	45.9333	50.0	14.6	1.51	10.4	0.20	7.49	12.2	0.18	2.89	0.15	99.7
R546-02	-130.0037	45.8631	50.1	14.4	1.53	10.6	0.20	7.38	12.3	0.19	2.85	0.15	99.6
R547-12	-129.9823	45.9333	49.8	14.6	1.50	10.4	0.19	7.59	12.1	0.19	2.88	0.14	99.4
R547-23	-129.9819	45.9332	49.8	14.6	1.51	10.4	0.18	7.55	12.1	0.19	2.88	0.15	99.3
R547-31	-129.9816	45.9334	49.8	14.6	1.52	10.4	0.19	7.55	12.1	0.19	2.87	0.15	99.3
R547-35	-129.9799	45.9261	50.1	14.4	1.52	10.4	0.19	7.49	12.1	0.19	2.89	0.13	99.4
R547-37	-129.9805	45.9261	50.2	14.4	1.37	10.1	0.20	7.68	12.6	0.12	2.70	0.11	99.5
R548-01	-129.9849	45.9462	50.0	14.5	1.50	10.5	0.21	7.16	12.1	0.19	2.87	0.15	99.3
R548-02	-129.9894	45.9162	49.2	14.3	1.50	10.4	0.21	7.34	12.0	0.18	2.88	0.15	98.1
R548-07	-129.9892	45.9175	49.3	14.3	1.47	10.5	0.20	7.32	12.1	0.19	2.88	0.14	98.3
R548-09	-129.9886	45.9188	49.4	14.5	1.52	10.5	0.20	7.32	12.1	0.19	2.89	0.17	98.7
R548-10	-129.9886	45.9188	49.4	14.5	1.52	10.4	0.20	7.28	12.2	0.19	2.88	0.15	98.7
R548-12	-129.9886	45.9188	49.9	14.5	1.52	10.4	0.21	7.14	12.2	0.19	2.86	0.16	99.1
R549-05	-129.9816	45.9334	49.2	14.3	1.53	10.3	0.18	7.30	12.1	0.19	2.89	0.16	98.1
R549-13	-129.9818	45.9330	49.7	14.5	1.51	10.5	0.19	7.30	12.1	0.19	2.88	0.14	98.9
R549-16	-129.9830	45.9287	49.0	14.3	1.52	10.4	0.20	7.35	12.0	0.18	2.84	0.14	97.9
R551-13	-129.9816	45.9334	49.0	14.5	1.52	10.5	0.20	7.49	12.0	0.19	2.84	0.14	98.4
R551-17	-129.9882	45.9227	49.4	14.7	1.51	10.3	0.20	7.37	12.1	0.19	2.82	0.15	98.7
R551-23	-129.9892	45.9175	49.0	14.6	1.52	10.4	0.21	7.25	12.1	0.20	2.82	0.14	98.3
R551-34	-129.9931	45.9175	49.7	14.7	1.50	10.3	0.21	7.32	12.1	0.20	2.84	0.14	98.9

Table 2-1. Continued.

Sample	Latitude	Latitude	SiO_2	Al_2O_3	TiO_2	FeO	MnO	MgO	CaO	K_2O	Na_2O	P_2O_5	Total
R552-01	-129.9882	45.9227	49.6	14.6	1.50	10.4	0.20	7.19	12.0	0.19	2.89	0.15	98.8
R552-02	-129.9932	45.9168	49.6	14.6	1.49	10.3	0.20	7.31	12.1	0.19	2.84	0.15	98.8
R552-03	-129.9898	45.9174	49.7	14.4	1.49	10.5	0.20	7.17	12.0	0.19	2.91	0.17	98.8
R552-06	-129.9761	45.9122	49.6	14.5	1.53	10.5	0.20	7.12	12.1	0.19	2.87	0.14	98.8
R552-07	-129.9777	45.9191	48.8	14.8	1.46	10.1	0.20	7.41	12.1	0.19	2.79	0.13	98.0
R552-08	-129.9761	45.9120	49.7	14.6	1.46	10.1	0.21	7.32	12.1	0.18	2.81	0.13	98.5
R554-02	-129.9982	45.8739	49.9	15.0	1.32	10.0	0.20	7.85	12.4	0.13	2.73	0.13	99.7
R554-03	-129.9983	45.8739	48.5	14.4	1.55	10.6	0.20	7.76	12.6	0.15	2.77	0.14	98.7
R554-04	-130.0003	45.8686	49.3	14.5	1.53	10.6	0.19	7.58	12.1	0.19	2.86	0.15	98.9
R554-05	-130.0015	45.8665	49.2	14.4	1.53	10.5	0.21	7.54	12.2	0.19	2.84	0.16	98.8
R554-06	-130.0015	45.8665	49.1	14.3	1.52	10.6	0.18	7.54	12.0	0.19	2.84	0.16	98.5
xl 1720-1B wr	-130.0139	45.9336	49.9	14.7	1.41	10.4	0.20	7.45	12.2	0.17	2.84	0.12	99.4
xl 1721-2B	-130.0140	45.9337	50.1	14.6	1.52	10.5	0.20	7.24	12.1	0.20	2.93	0.14	99.5
xl 1722-3	-130.0158	45.9337	50.2	14.5	1.50	10.6	0.20	7.35	11.8	0.19	2.92	0.15	99.4
xl 1723-1B	-130.0142	45.9333	50.2	14.5	1.53	10.6	0.20	7.35	11.7	0.19	2.90	0.15	99.3
xl 1723-1A	-130.0142	45.9333	50.1	14.5	1.53	10.5	0.22	7.33	12.1	0.20	2.90	0.14	99.5
xl 1724-4A	-130.0142	45.9333	49.9	14.6	1.53	10.6	0.22	7.37	12.0	0.19	2.92	0.16	99.4
xl 1726-1.8	-130.0139	45.9336	50.1	14.5	1.54	10.6	0.20	7.32	12.1	0.19	2.90	0.14	99.5
xl 1726-2	-130.0083	45.9250	49.2	14.6	1.52	10.6	0.22	7.42	11.8	0.18	2.94	0.15	98.7
xl 1726-6	-130.0138	45.9336	50.2	14.5	1.51	10.6	0.21	7.37	11.8	0.20	2.90	0.15	99.4
xl 1727-8	-130.0167	45.9375	49.1	16.6	0.91	8.6	0.17	9.36	12.0	0.09	2.31	0.07	99.2
xl 1728-4B	-130.0142	45.9333	49.7	15.5	1.20	9.7	0.18	8.29	11.9	0.13	2.66	0.12	99.4
xl 1728-6.7	-130.0140	45.9333	50.0	14.4	1.50	10.4	0.21	7.32	11.7	0.19	2.92	0.16	98.9
xl 1729-1	-130.0135	45.9337	50.0	14.5	1.55	10.5	0.20	7.31	12.1	0.19	2.94	0.16	99.5
xl 1729-8	-130.0135	45.9337	50.2	14.6	1.49	10.5	0.21	7.39	11.7	0.19	2.91	0.14	99.3
xl 1730 2-3	-129.9834	45.9371	50.1	14.5	1.51	10.5	0.22	7.47	11.7	0.19	2.92	0.16	99.4
xl 1730-4	-129.9839	45.9409	50.0	14.6	1.55	10.6	0.22	7.25	12.1	0.19	2.93	0.15	99.5
xl 1730-6-7	-129.9827	45.9396	50.1	15.0	1.23	9.9	0.20	8.12	12.0	0.11	2.64	0.11	99.4
xl 1730-MC 5	-129.9835	45.9427	50.0	14.5	1.51	10.5	0.19	7.38	12.1	0.18	2.95	0.13	99.5
xl 1731- 6.7B2	-130.0284	45.9885	49.7	14.3	1.48	10.5	0.20	7.22	11.7	0.19	2.85	0.15	98.3
xl 1731-4	-130.0283	45.9900	50.0	14.5	1.49	10.5	0.21	7.32	12.1	0.19	2.91	0.14	99.5
xl 1731-6.7B1	-130.0284	45.9887	50.0	14.2	1.43	10.4	0.20	7.25	11.8	0.18	2.79	0.16	98.4

Table 2-1. Continued.

Sample	Latitude	Latitude	SiO_2	Al_2O_3	TiO_2	FeO	MnO	MgO	CaO	K_2O	Na_2O	P_2O_5	Total
xl 1731-6-1	-130.0281	45.9886	50.2	14.5	1.53	10.6	0.19	7.35	11.7	0.19	2.97	0.15	99.4
xl 1732 -1-8A	-130.0172	45.9323	50.3	14.5	1.51	10.5	0.20	7.30	11.7	0.19	2.92	0.14	99.2
xl 1732- 4.8B	-130.0154	45.9312	50.0	14.4	1.54	10.8	0.22	7.01	11.9	0.11	3.02	0.15	99.0
xl 1732-1.8B	-130.0170	45.9322	50.1	14.5	1.52	10.5	0.21	7.27	12.1	0.18	2.93	0.16	99.5
xl 1732-2.3A	-130.0164	45.9318	49.9	14.6	1.43	10.3	0.20	7.35	11.7	0.18	2.80	0.15	98.6
xl 1732-MCB	-130.0125	45.9314	50.5	14.2	1.63	11.3	0.22	6.93	11.3	0.22	3.18	0.17	99.8
xl 1733-4	-130.0138	45.9336	50.1	14.5	1.51	10.5	0.21	7.38	12.1	0.19	2.93	0.16	99.5

Figure 2-3. Major element variation for samples collected from the Axial Segment during four NeMO cruises, with an additional 28 samples collected in 1986 from the Axial Seamount caldera region by the Pisces IV submersible. Comparisons with the Juan de Fuca Ridge (JdFR) and Cobb-Eickelberg (C-E) fields shows that the study area samples have the same relative enrichments and depletions as the C-E seamounts, although they still generally reside within the JdFR fields. High alkalis and K_20/TiO_2 are particularly diagnostic of the C-E and Axial Segment lavas. Liquid lines of descent were generated using the methods of Weaver and Langmuir (1990), which show that fractional crystallization of a single mafic parental magma cannot explain the observed major element variation. Data for the C-E seamounts field are from Desonie and Duncan (1990), and for the JdFR field: (Cleft Segment) this study; Eaby et al., 1984; Smith et al., 1994, (Vance Segment) this study; Eaby et al., 1984; M. Perfit unpublished data, (CoAxial Segment) Eaby et al., 1984; Smith, 1999 (Cobb Segment), Eaby et al., 1984; Van Wagoner and Leybourne.

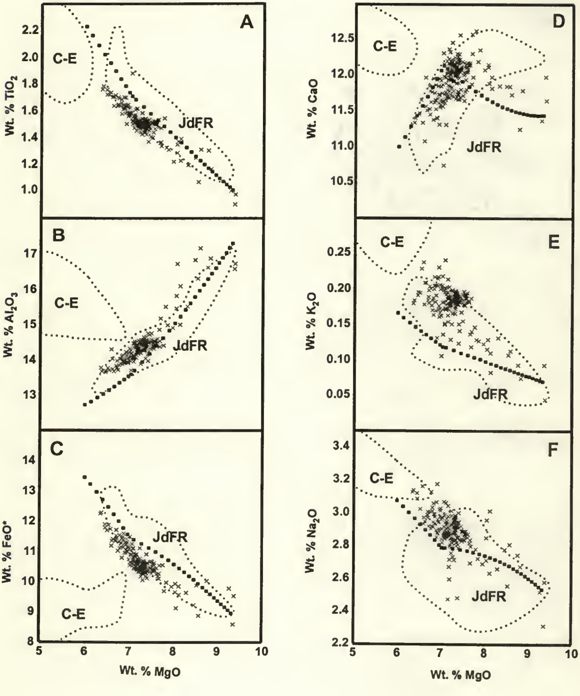
A
B
C
D
E
F
C-E
JdFR
Wt. % TiO$_2$
Wt. % Al$_2$O$_3$
Wt. % FeO*
Wt. % CaO
Wt. % K$_2$O
Wt. % Na$_2$O
Wt. % MgO
Wt. % MgO
2.2
2.0
1.8
1.6
1.4
1.2
1.0
17
16
15
14
13
14
13
12
11
10
9
8
12.5
12.0
11.5
11.0
10.5
0.25
0.20
0.15
0.10
0.05
3.4
3.2
3.0
2.8
2.6
2.4
2.2
5
6
7
8
9
10

Figure 2-3. Continued.

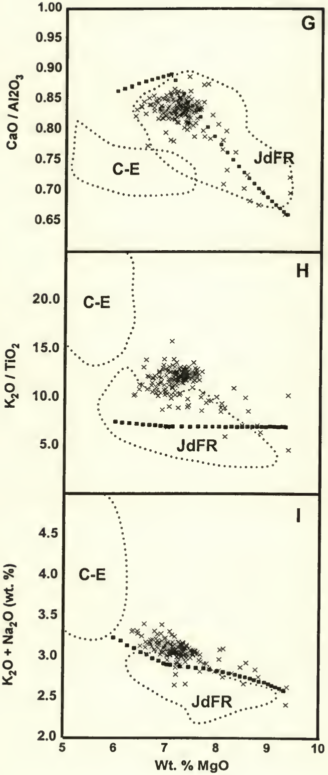
G
CaO / Al2O3
1.00
0.95
0.90
0.85
0.80
0.75
0.70
0.65
C-E
JdFR
H
K_2O / TiO_2
20.0
15.0
10.0
5.0
C-E
JdFR
I
K_2O + Na_2O (wt. %)
4.5
4.0
3.5
3.0
2.5
2.0
C-E
JdFR
5
6
7
8
9
10
Wt. % MgO

FeO, TiO_2, MnO, Na_2O, K_2O, and P_2O_5, and decreasing Al_2O_3 and CaO with decreasing MgO (Figure 2-3). In spite of the potential influence of the Cobb hotspot, most of the basalts recovered from the study area contain relatively low K_2O contents and can be classified as mid-ocean ridge basalts (MORB) (Rhodes et al., 1990; Desonie and Duncan, 1990), with the exception of the four tholeiitic andesites that were recovered from the eastern side of the north rift zone (RC-49, -99, -100, and -101). These andesites are extremely rare along the JdFR, having only been recovered in one other area, near the ridge-transform intersection at the southern end of the Cleft Segment (Perfit et al., 2001).

Compositional fields for lavas from the Cobb-Eickelberg seamounts and basalts from JdFR segments located to the south of the Cobb Offset (located between the Endeavor and Cobb Segments) are shown in Figure 2-3, to evaluate the geochemical influence of the Cobb hotspot on lavas erupted from the Axial Segment. The Endeavor and West Valley Segments are not included in the JdFR comparative group due to the presence of anomalously enriched lavas including E-MORB on these northernmost segments (Karsten et al., 1990; Van Wagoner and Leybourne, 1991). Axial Segment basalts generally fall within the JdFR fields, but are among the most enriched compared with the Cleft, Vance, CoAxial, and Cobb Segments, in CaO, Na_2O, and K_2O, and notably depleted in FeO and TiO_2 at comparable MgO contents. These departures from the JdFR trends reflect the same relative enrichments and depletions at given MgO contents that are observed for these elements in the C-E basalts, an indication of the influence of the Cobb plume on the Axial Segment basalts (Figure 2-3). The observed enrichment in total alkalis (Na_2O+K_2O) is one of the most prominent geochemical expressions of the Cobb hotspot (Desonie and Duncan, 1990; Rhodes et al., 1990), and Axial Segment lavas reflect this with values up to 3.4 wt.% (Figure 2-3).

Liquid line of descent (LLD) calculations (Weaver and Langmuir, 1990) produce major element variations that follow the general trend of the data (Figure 2-3). The models predict olivine plus plagioclase fractionation for even the most mafic samples in the suite, and clinopyroxene is expected to fractionate in the more evolved magmas. LLD models were run at 1 Kbar, an appropriate pressure considering seismic tomographic data identified a large magma storage body at about 2.25-3.5 km depth under Axial Seamount (West et al., 2001). Similar fractional crystallization models have been proposed to explain major element variations in basalts from other segments of the JdFR (Smith et al., 1994; Sours-Page et al., 1999). Inflections observed in the diagrams for CaO variation and CaO/Al_2O_3 (Figure 2-3) correspond to the appearance of clinopyroxene on the liquidus, although this phase is absent in thin section except in the groundmass. Clear control of basaltic liquid fractionation by clinopyroxene with scarce representation of the phase in thin section is relatively common for evolved basalts and has appropriately been termed the 'pyroxene paradox' (e.g. Grove et al., 1992; Maclennan, et al., 2001).

Although LLD calculations produce major element variations that generally correspond to the observed trends, a single liquid line of descent cannot explain the wide scatter in major element concentrations for the suite of lavas from the study area (Figure 2-3). Instead, the basalts appear to have originated and evolved from a broad range of parental magmas. This is particularly evident in the variation observed in K_2O/TiO_2 (Figures 2-3 and 2-5), a ratio that will show only a minor increase with crystal fractionation in a cogenetic suite, but varies from 4.54 to 15.82.

The basalts in Table 2-1 have been grouped based on their location, with "Seamount Group" samples taken from the Axial Seamount caldera and flanks, where bathymetric contours are roughly concentric to the caldera and lavas have flowed downslope from the summit region (Figure 2-1). "Ridge Group" samples are those taken from the rift zones to the north and south of Axial Seamount on the Axial Segment, where the volcanic morphology and bathymetric contours are clearly dominated by parallel-trending volcanic ridges. This grouping based on morphology does not coincide with any abrupt changes in geochemistry, but suffices to separate lavas that may have erupted directly from Axial Seamount and those that were erupted along the "ridge" portion of the Axial Segment. The boundary between the Seamount and Ridge Groups is roughly demarcated by the 1600 m isobath contour.

Seamount Group lavas are generally more primitive than the Ridge Group, with MgO values ranging from 6.7 to 9.4 wt.%, and the vast majority (139 of 155) falling in a small range of lower values between 7.0 and 7.6 wt. % These basalts can be classified as ferrobasalts, with most FeO concentrations in excess of 10 wt. %. The largely restricted compositional variation (average MgO 7.36 wt. %, s.d. 0.26) possibly reflects long-term storage and homogenization of magmas in a large chamber or lens under Axial Seamount (Perfit et al., 1988; Rhodes, 1988; West, 2001). However, six mafic basalts (MgO > 7.75 wt.%) were collected in and near the caldera, suggesting that some of the seamount magmas circumvent this homogenization process. The low standard deviations and implied geochemical homogeneity of the Seamount Group are likely due in part to a sampling bias, as many of the basalts from Axial Seamount were collected by submersibles in confined sampling areas, and numerous samples may come from individual lava flows. However, when this bias is removed and only samples from diverse parts of the caldera and flanks are examined, there is still very little geochemical variation, and a high degree of homogeneity is still demonstrable.

Basalts from the Ridge Group have significantly higher compositional variability than the Seamount Group, with similar ranges of MgO (9.37 to 6.35 wt. %,), but substantially higher standard deviations (e.g., average MgO 7.20; s.d. 0.57, not including the andesites) and a notable lack of homogeneity. At a given distance from the seamount, however, the variability is similar to that observed in the Seamount Group (Figure 2-4a). The overall greater chemical variability in the Ridge Group is largely due to gradients in major element contents with distance from Axial Seamount, with more primitive basalts found close to Axial

Figure 2-4. (A) Spatial variation in MgO content, showing a distinct trend of decreasing MgO with distance from the Axial Seamount caldera in the rift zones of the Axial Segment. Correlative increases and decreases in other major element concentrations suggest this is a fractional crystallization trend that increases with distance from the hotspot along the ridge. A few basalts have more mafic compositions (>7.75%) and do not fall along the main trend. (B and C) The anticipated enrichment in incompatible trace element compositions as a result of this fractionation with distance is not observed. The ratios of Zr/Y and Sr show decreases with distance from the hotspot. The peaks in the trends appear to be slightly offset to the north of the Axial Seamount caldera.

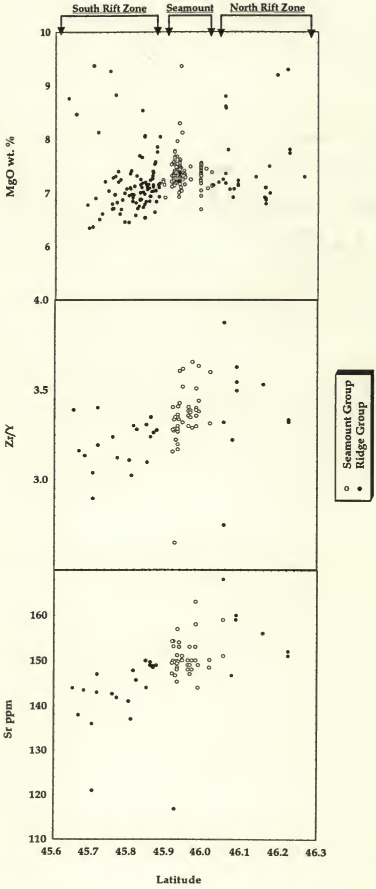
South Rift Zone
Seamount
North Rift Zone
MgO wt. %
10
9
8
7
6
4.0
3.5
3.0
Zr/Y
Sr ppm
160
150
140
130
120
110
45.6
45.7
45.8
45.9
46.0
46.1
46.2
46.3
Latitude
○ Seamount Group
● Ridge Group

Seamount, and increasingly more evolved lavas at greater distance from the hotspot (Figure 2-4a). The corresponding decreases observed in Al_2O_3 and CaO and increases in TiO_2, FeO, and K_2O suggest that this spatial pattern is controlled by fractional crystallization. Scattered among this gradient are a few higher-MgO basalts (>7.75 wt. %) that clearly do not fall along the regional trend. Some of these mafic samples were collected from small volcanic cones in the rift zones, but others were collected in areas with no anomalous bathymetric features.

Trace Element Geochemistry

Trace element concentrations in glasses were measured by x-ray fluorescence (XRF) spectroscopy and inductively coupled plasma mass spectrometry (ICP-MS). The trace element concentrations in representative basalt samples are presented in Table 2-2. The homogeneity observed in major element chemistry of the Seamount Group is also observed in the trace element compositions, with a largely confined grouping of points on trace element diagrams (Figure 2-5). Sr concentrations range from 145 to 156 ppm Y ranges from 27 to 32 ppm, Sr/Y ratios range from 5.5 to 4.6, Ce_N/Yb_N (chondrite normalized) from 0.9 to 1.1, and K_2O/TiO_2 ratios range from 6.9 to 15.8, all generally intermediate between the compositions of the C-E Seamounts and the most depleted compositions from the JdFR. Seamount Group Zr/Y ratios range from 3.2 to 3.6, and Zr/Nb from 18.6 to 23.6, values that slightly higher than the ranges of basalts from the JdFR (Figure 2-5), resulting from similar Zr and lower Y concentrations in Axial Seamount basalts.

Table 2-2. Representative Seamount Group trace elements; analyzed by XRF[1] and ICP-MS[2].

Sample	R460-06	R461-16	R461-25	R461-26	R462-08	R462-15	R467-01	R471-04	R473-21	R474-02	R474-03	R476-02
XRF (ppm)												
Zr	99.1	98.5	71.1	97.1	98.7	98.4	98.8	98.5	97.0	94.7	100.0	98.8
Sr	149.6	150.0	116.8	149.6	149.9	148.5	150.1	151.2	146.7	148.0	149.7	150.2
Y	29.6	30.1	26.8	29.0	29.9	31.1	29.8	30.2	30.1	28.9	30.0	29.8
Nb	4.6	4.6	1.7	4.5	4.9	4.6	5.3	4.9	4.7	4.7	4.8	4.9
Sc	60.0	66.7	55.2	60.6	54.7	59.4	57.1	56.9	65.0	63.7	59.6	61.1
ICP-MS (ppm)												
Cr			317			279						
Ni			61			46						
Rb			1.1			2.1						
V			263			295						
La			2.8			4.7						
Ce			8.7			13.6						
Pr			1.5			2.1						
Nd			8.2			11.0						
Sm			2.7			3.5						
Eu			1.0			1.3						
Gd			3.9			4.7						
Tb			0.7			0.8						
Dy			4.7			5.2						
Ho			1.0			1.1						
Er			2.7			3.0						
Tm			0.4			0.5						
Yb			2.6			3.0						
Lu			0.4			0.5						
Sr/Y	5.1	5.0	4.4	5.2	5.0	4.8	5.0	5.0	4.9	5.1	5.0	5.0
Zr/Y	3.3	3.3	2.7	3.3	3.3	3.2	3.3	3.3	3.2	3.3	3.3	3.3
Y/Nb	6.5	6.6	15.9	6.5	6.1	6.7	5.6	6.1	6.5	6.1	6.2	6.1
Zr/Nb	21.7	21.5	42.0	21.7	20.2	21.2	18.6	20.0	20.8	20.1	20.7	20.2
Ce_N/Yb_N			0.8			1.0						

[1] XRF analyses performed at the University of Florida, Dept. of Geological Sciences.

[2] ICP-MS analyses performed at the Geological Survey of Canada.

Table 2-2. Continued (Seamount Group).

Sample	R479-15	R488-16	R491-22	R497-20	R501-02	R501-07	R501-09	R501-10	R501-12	R548-02	R552-02	R552-07
XRF (ppm)												
Zr	93.3	98.7	97.2	116.3	96.5	98.6	97.3	101.3	95.4	97.2	100.8	94.9
Sr	145.4	149.4	156.9	148.5	154.3	149.5	147.2	153.2	154.3			
Y	29.2	29.3	28.5	32.3	28.3	30.1	30.8	30.9	28.6	29.0	27.8	27.8
Nb	4.7	4.8	5.0	5.3	4.5	4.7	4.4	4.3	4.7	5.3	5.6	5.5
Sc	58.9	64.2	60.8	56.2	55.5	61.2		66.3	61.6			
ICP-MS (ppm)												
Cr	295	282	302	276	295	283		199	298			
Ni	47	44	55	44	51	46		44	52			
Rb	2.1	2.1	2.3	2.3	2.1	2.0		2.1	2.1			
V	290	297	281	287	284	296		293	283			
La	4.9	4.8	5.1	5.5	4.7	4.8		4.9	4.7			
Ce	13.0	13.0	14.0	15.2	13.0	13.0		14.0	13.0			
Pr	2.2	2.1	2.2	2.3	2.1	2.1		2.1	2.2			
Nd	12.0	11.0	11.0	12.0	11.0	11.0		11.0	11.0			
Sm	3.5	3.8	3.5	3.8	3.6	3.6		3.8	3.6			
Eu	1.4	1.4	1.4	1.4	1.4	1.4		1.4	1.3			
Gd	4.8	5.0	4.7	5.1	4.8	4.7		4.8	4.6			
Tb	0.8	0.9	0.8	0.9	0.8	0.9		0.9	0.9			
Dy	5.3	5.5	5.2	5.4	5.3	5.4		5.4	5.2			
Ho	1.2	1.2	1.1	1.2	1.2	1.2		1.2	1.2			
Er	3.1	3.1	2.9	3.2	3.1	3.1		3.2	3.1			
Tm	0.5	0.5	0.5	0.5	0.5	0.5		0.5	0.5			
Yb	3.2	3.2	3.1	3.3	3.2	3.2		3.3	3.1			
Lu	0.5	0.5	0.5	0.5	0.5	0.5		0.5	0.5			
Sr/Y	5.0	5.1	5.5	4.6	5.4	5.0	4.8	5.0	5.4			
Zr/Y	3.2	3.4	3.4	3.6	3.4	3.3	3.2	3.3	3.3	3.3	3.6	3.4
Y/Nb	6.2	6.2	5.7	6.1	6.3	6.4	6.9	7.2	6.1	5.5	5.0	5.1
Zr/Nb	19.9	20.7	19.3	21.9	21.3	21.0	21.9	23.6	20.2	18.3	18.0	17.3
Ce_N/Yb_N	0.9	0.9	1.0	1.1	0.9	0.9		1.0	1.0			

Table 2-2. Continued (Ridge Group).

Sample	RC-11	RC-102	RC-107	RC-108	RC-55	RC-60	RC-70	RC-75	RC-79	RC-81	99-RC-85
XRF (ppm)											
Zr	96.5	97.1	93.9	98.0	94.9	96.9	78.0	89.2	87.3	81.7	91.2
Sr	150.0	146.7		147.9	143.5		110.2	141.8	142.6		144.0
Y	29.2	30.1	28.2	29.7	30.3	29.2	27.2	28.6	27.0	26.7	29.5
Nb	4.5	3.8	4.6	4.1	4.1	5.2	3.6	3.5	3.5	3.2	3.9
Sc	58.8	63.9		53.1	64.5			57.8	60.7		47.0
ICP-MS (ppm)											
Cr	309	315		331	308			282	324		300
Ni	53	52		42	55			48	52		51
Rb	2.0	1.8		2.2	1.7			1.8	1.8		1.9
V	291	289		295	286			276	274		278
La	4.8	4.3		4.8	4.3			4.3	4.1		4.3
Ce	13.0	12.7		13.2	12.0			12.0	11.7		12.4
Pr	2.1	1.9		2.1	2.0			2.0	1.8		1.9
Nd	11.0	10.8		11.3	11.0			10.0	9.8		10.1
Sm	3.4	3.5		3.4	3.4			3.2	3.2		3.4
Eu	1.3	1.3		1.3	1.3			1.3	1.2		1.3
Gd	4.8	4.8		4.7	4.7			4.5	4.3		4.5
Tb	0.8	0.9		0.8	0.8			0.8	0.8		0.8
Dy	5.1	5.3		5.3	5.2			5.1	4.8		4.9
Ho	1.1	1.2		1.2	1.1			1.1	1.1		1.1
Er	3.0	3.2		3.1	3.0			3.0	2.8		2.9
Tm	0.5	0.5		0.5	0.5			0.5	0.4		0.4
Yb	3.1	3.2		3.1	3.1			3.3	2.8		2.9
Lu	0.5	0.5		0.5	0.5			0.5	0.5		0.5
Sr/Y	5.1	4.9		5.0	4.7		4.1	5.0	5.3		4.9
Zr/Y	3.3	3.2	3.3	3.3	3.1	3.3	2.9	3.1	3.2	3.1	3.1
Y/Nb	6.5	8.0	6.1	7.3	7.4	5.6	7.6	8.1	7.8	8.3	7.6
Zr/Nb	21.3	25.7	20.4	23.9	23.2	18.6	21.7	25.2	25.2	25.5	23.5
Ce_N/Yb_N	1.0	0.9		1.0	0.9			0.8	0.9		1.0

Table 2-2. Continued (Ridge Group).

Sample	RC-86	RC-88	RC-89	RC-91	R465-01	R465-02	R494-04	R494-05	R494-08	R554-04	R554-06
XRF (ppm)											
Zr	97.6	93.1	97.0	90.9	97.5	98.4	98.4	98.0	97.9	97.3	98.8
Sr		137.1	145.7	141.0	148.5	148.8	149.0	149.7	149.0		
Y	31.5	30.8	29.6	29.2	29.9	30.2	29.4	30.2	29.9	29.1	29.5
Nb	5.5	4.3	4.8	3.6	4.7	4.6	4.8	4.3	4.4	5.2	5.6
Sc		57.6	58.7	55.0	60.1	53.2	61.6	62.6	67.4		
ICP-MS (ppm)											
Cr		262	287	330	285		280	282	281		
Ni		48	44	53	47		44	45	45		
Rb		2.0	2.2	1.6	2.0		2.1	2.1	2.0		
V		289	296	273	290		294	297	294		
La		4.3	5.1	4.0	4.6		4.8	4.9	4.9		
Ce		12.6	13.7	12.0	13.1		13.0	14.0	13.3		
Pr		2.0	2.2	1.9	2.1		2.2	2.2	2.1		
Nd		10.5	11.3	10.2	10.7		11.0	11.0	11.4		
Sm		3.5	3.5	3.3	3.3		3.7	3.5	3.6		
Eu		1.3	1.3	1.2	1.4		1.4	1.3	1.4		
Gd		4.9	4.9	4.5	4.6		4.8	4.8	4.8		
Tb		0.8	0.8	0.8	0.8		0.9	0.9	0.9		
Dy		5.2	5.4	5.0	5.2		5.4	5.4	5.4		
Ho		1.1	1.2	1.1	1.1		1.2	1.2	1.2		
Er		3.1	3.2	2.9	2.9		3.1	3.2	3.1		
Tm		0.5	0.5	0.5	0.5		0.5	0.5	0.5		
Yb		3.1	3.1	2.9	2.9		3.3	3.3	3.2		
Lu		0.5	0.5	0.5	0.5		0.5	0.5	0.5		
Sr/Y		4.5	4.9	4.8	5.0	4.9	5.1	4.9	5.0		
Zr/Y	3.1	3.0	3.3	3.1	3.3	3.3	3.3	3.2	3.3	3.3	3.4
Y/Nb	5.7	7.2	6.1	8.0	6.3	6.5	6.1	7.0	6.8	5.6	5.3
Zr/Nb	17.8	21.7	20.1	24.9	20.7	21.2	20.5	22.6	22.4	18.7	17.6
Ce_N/Yb_N		0.9	1.0	0.9	1.0		0.9	1.0	0.9		

Trace element compositions in basalts from the Ridge Group are similar to those from the Seamount Group, but are generally less enriched in incompatible elements (not including the 4 andesites), creating a trend in the Axial Segment data (Figure 2-5) toward the generally more depleted JdFR basalt compositions. Overall, Zr/Y ranges from 3.0 to 3.3, Zr/Nb ranges from 20 to 25, Ce_N/Yb_N ranges from 0.9 to 1.0, and K_2O/TiO_2 ratios range from 7.0 to 12.3. Although there is clear evidence in the major element data for increased fractionation of magmas in the rift zones with distance from Axial Seamount (Figure 2-4a), the expected corresponding enrichment in incompatible element abundances and ratios is not observed. Instead, there is a moderate *decreasing* gradient in K_2O/TiO_2, Zr/Y, and Sr/Y ratios with increasing distance from the hotspot in the Ridge Group (Fig 4b).

The relative enrichments and depletions in trace element compositions in Axial Segment lavas relative to the neighboring JdFR generally reflect the enrichments and depletions of the C-E Seamounts, similar to the major element behavior. C-E Seamount Sr and Nb concentrations are distinctly higher than those from the JdFR, and Axial Segment basalts are intermediate between the two (Rhodes et al., 1990; Figure 2-5). Conversely, concentrations of Y are lower in C-E basalts than the JdFR, and Axial Segment Y values are likewise at an intermediate value and lower. The only exception is Sc, as Axial Segment basalts have higher Sc concentrations than both the JdFR and C-E Seamounts. The C-E basalts are more evolved than those from the JdFR, and increased fractionation

Figure 2-5. Axial Segment basalts are enriched in Sr, Sc, and Nb and depleted in Y relative to the rest of the Juan de Fuca Ridge, reflecting the same relative enrichments of the Cobb hotspot. The exception is Sc, which is lower for the C-E Seamounts and may reflect more progressed fractionation of clinopyroxene. (B) The Axial Segment basalts are distinctly intermediate between the JdFR and C-E compositions. However, some of the more mafic (MgO >7.75 wt. %) basalts fall within the JdFR field, suggesting that these represent the indigenous Axial Segment MORB.

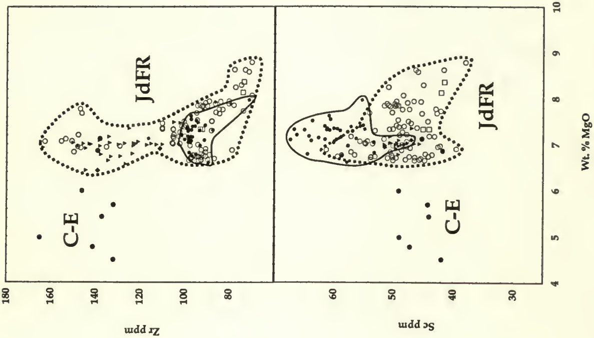
Zr ppm
180
160
140
120
100
80
C-E
JdFR
Sc ppm
60
50
40
30
C-E
JdFR
4
5
6
7
8
9
10
Wt. % MgO

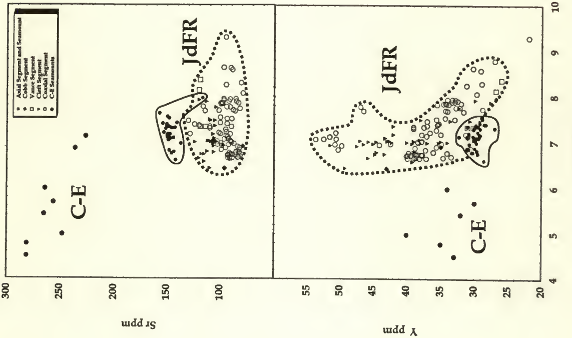
■ Axial Segment and Seamount
● Cobb Segment
□ Vance Segment
▼ Cleft Segment
○ Coaxial Segment
● C-E Seamounts
Sr ppm
300
250
200
150
100
C-E
JdFR
Y ppm
55
50
45
40
35
30
25
20
JdFR
C-E
4
5
6
7
8
9
10
Wt. % MgO

Figure 2-5. Continued.

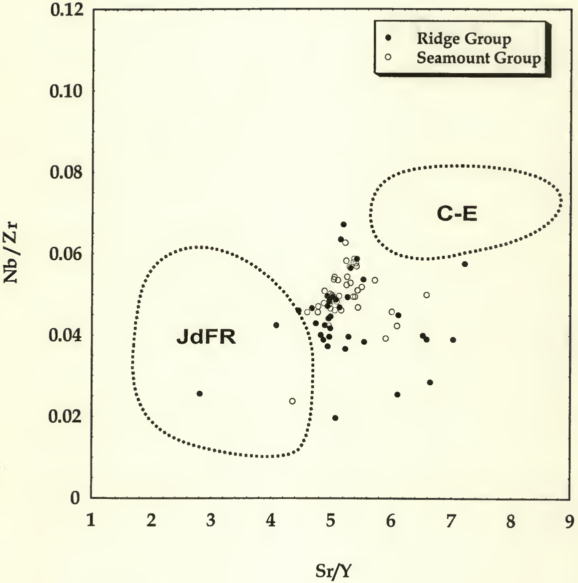
0.12
0.10
0.08
0.06
0.04
0.02
0
Nb / Zr
1
2
3
4
5
6
7
8
9
Sr/Y
● Ridge Group
○ Seamount Group
C-E
JdFR

of clinopyroxene may have led to a substantial decrease in Sc, which is compatible in this phase.

The high-MgO basalts found scattered along the Axial Segment in both the Ridge and Seamount Groups exhibit distinct depleted trace element compositions similar to JdFR MORB (Table 2-2). Representative samples (R461-25 from the Seamount Group and RC-70 from the Ridge Group) have much lower Sr, Zr, Nb and REE concentrations than the more common lower-MgO basalts in suite, and have depleted LREE patterns ($Ce_N/Yb_N = 0.76$) typical of N-MORB and similar to those from the CoAxial and Vance Segments (Figure 2-6). The typical lower-MgO basalts in the suite have relatively flat REE patterns, and average about 15 times chondritic abundances. The flat REE pattern in these basalts results from an enrichment in LREE relative to N-MORB. Despite the clear evidence for plagioclase fractionation in the suite, negative Eu anomalies are observed only in the andesites, which have flat REE patterns and concentrations that are 50 to 100 times chondritic. Some REE patterns show minor depletions of the HREE heavier than Dy, suggesting the presence of residual garnet in the melt source.

As a trace element compatible in olivine, Ni should show a decrease with MgO content and fractionation in a cogenetic suite, but considerable scatter is evident and only a general correlation exists (Table 2-2). Similarly, a general decrease in Sc and Cr, along with decreasing CaO/Al_2O_3 supports the likelihood of clinopyroxene fractionation in more evolved samples, but again scatter

Figure 2-6. Axial Segment basalts have flat rare earth element patterns that are distinctly enriched relative to the typical depleted MORB patterns shown by basalts from the neighboring CoAxial Segment. The MORB-like pattern displayed by the depleted basalt from the Axial Segment (R461-25) suggest these depleted types have a higher proportion of a MORB mixing end-member.

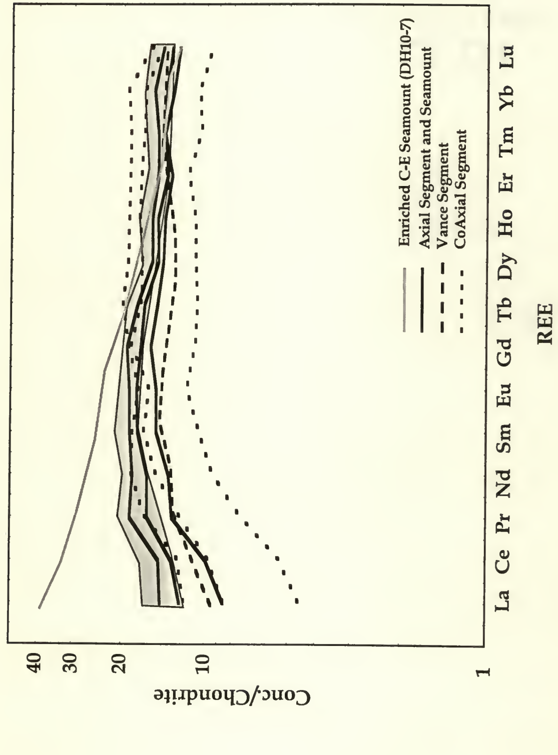
Conc./Chondrite
40
30
20
10
1
La
Ce
Pr
Nd
Sm
Eu
Gd
Tb
Dy
Ho
Er
Tm
Yb
Lu
REE
Enriched C-E Seamount (DH10-7)
Axial Segment and Seamount
Vance Segment
CoAxial Segment

suggests that fractionation is not the sole process controlling their abundances. Sr is compatible in plagioclase but incompatible in olivine and clinopyroxene, and should remain fairly constant during fractionation in cogenetic suites (D~1). However, there is a clear decrease in Sr concentrations with MgO content in the Axial Segment basalts, evidence for possible mixing between enriched and depleted components (Figure 2-4c).

Isotope Geochemistry

To further constrain the mantle source characteristics and discriminate between the compositions of possible mixing end-members for Axial Segment lavas, $^{87}Sr/^{86}Sr$, $^{206}Pb/^{204}Pb$, $^{207}Pb/^{204}Pb$, and $^{208}Pb/^{204}Pb$ isotopic ratios of 11 basalts from the Seamount and Ridge Groups were measured (Table 2-3). Radiogenic isotopic ratios are effective tools because they are not changed by melting or most shallow crustal processes. Sr isotopic ratios for the Axial Segment fall along a regional trend for the JdFR, which decreases from a high value on the Cleft Segment, declines to a minimum on the CoAxial Segment, then increases again toward the Cobb Offset (Eaby et al., 1984; Smith, 1999; Embley, 2000). Axial Segment radiogenic isotopic ratios do not depart from the regional JdFR trend largely due to the relatively unradiogenic and MORB-like isotopic composition of the Cobb hotspot. Samples from the C-E Seamounts have $^{87}Sr/^{86}Sr$ ratios ranging from 0.70245-0.7026 and $^{143/144}Nd$ ranging from 0.513109-0.513204 (Hegner and Tatsumoto, 1987; Desonie and Duncan, 1990). The Sr and Nd isotopic compositions for basalts from the Axial Segment (Eaby et

Table 3. Radiogenic Isotopic ratios for Axial Segment, Juan de Fuca Ridge, and Cobb-Eickelberg Basalts. Sources noted in parentheses.

Location	$^{87}Sr/^{86}Sr^1$	$^{143}Nd/^{144}Nd$	$^{206}Pb/^{204}Pb^2$	$^{207}Pb/^{204}Pb^2$	$^{208}Pb/^{204}Pb^2$
Axial Segment (this study)					
RC-11	0.702515				
RC-55	0.702496				
RC-64	0.702538				
RC-75	0.702504				
RC-82			18.501	15.442	37.912
RC-89	0.702548				
RC-98			18.565	15.404	37.991
RC-100	0.702614		18.548	15.448	37.925
R548-2	0.702510				
R497-20	0.702509		18.629	15.457	37.990
Axial Segment (Eaby et al., 1984)					
Y74-1-3-33	0.702530				
Y74-1-3-41	0.702560				
TT152-77-6	0.702440				
TT152-77-7	0.702520				
Y74-1-1-7	0.702450				
Y74-1-1-34	0.702520				
TT152-55-25	0.702570				
TT170-5	0.702460				
TT152-53-6	0.702500				
TT152-61-1	0.702490				
Axial Segment (Rhodes, 1990)					
Axial D55-1	0.702370	0.513170			
Axial 47-3	0.702430	0.513120			
Axial SRZ D77-7	0.702330	0.513240			
Cobb-Eickelberg Seamounts (Desonie and Duncan, 1990; Church and Tatsumoto, 1975)					
Eikelberg DH1-1	0.702467	0.513109	18.663	15.477	37.895
Eikelberg DH2A	0.702507	0.513122	18.624	15.491	37.985
Eikelberg DH28	0.702518	0.513128	18.609	15.521	38.028
Cobb CB-1	0.702454	0.513135	18.823	15.494	38.233
Warwick DH4-4	0.702596	0.513109	18.620	15.498	37.985
Cobb C-1	0.702490	0.513132	18.809	15.479	38.140
Cobb C-1	0.702560	0.51319	18.377	15.475	37.940
Cobb C-3	0.702570	0.513204	18.423	15.480	37.960
JdFR (this study)					
RC-94			18.679	15.476	38.043
JdFR-Cleft Segment (Hegner and Tatsumoto, 1987)					
alv 1455-2r	0.702524	0.513148	18.452	15.477	37.820
alv 1455-4r	0.702491	0.513152	18.461	15.491	37.866
alv 1457-1r-c	0.702479	0.513155	18.444	15.471	37.811
alv 1458-2r	0.702515	0.513199	18.435	15.458	37.764
alv 1459-1r	0.702451	0.513142	18.440	15.466	37.787
alv 1461-3r	0.702496	0.513140	18.461	15.471	37.824
alv1461-7r	0.702498	0.513143	18.440	15.462	37.777

[1] Long-term measurement of NBS 987 standard: $^{87}Sr/^{86}Sr$ value of [.710216 ± 45x10^{-6} check]

[2] NBS-981 standard during measurement: $^{206}Pb/^{204}Pb$ 16.91518722 ± 8.656 x 10^{-3}; $^{207}Pb/^{204}Pb$ 15.4492077 ± 9.757 x 10^{-3}; $^{208}Pb/^{204}Pb$ 36.5776344 ± 3.196 x 10^{-2}

Table 3. Continued.

Location	$^{87}Sr/^{86}Sr$	$^{143}Nd/^{144}Nd$	$^{206}Pb/^{204}Pb$	$^{207}Pb/^{204}Pb$	$^{208}Pb/^{204}Pb$
NE Pacific MORB (White et al., 1987)					
JDF VG768	0.702440	0.513030	18.766	15.547	38.226
JDF VG44	0.702580	0.513069	18.751	15.563	38.568
JDF D10-1	0.702560	0.513176	18.486	15.485	37.852
JDF VG348	0.702490	0.513250	18.470	15.457	37.867
JDF Average	0.702500	0.513150	18.488	15.480	37.897
Pacific N-MORB Average	0.702540	0.513140	18.437	15.489	37.891

al., 1984; Rhodes, 1990) are similarly unradiogenic in $^{87}Sr/^{86}Sr$ (0.7024-0.7026) and radiogenic in $^{143}Nd/^{144}Nd$ (0.5130-0.5132). The MORB-like character of the Cobb hotspot is anomalous for fixed mantle plumes (Desonie and Duncan, 1990; Rhodes, 1990).

All of the Axial Segment isotopic ratios fall within MORB-like ranges, but they are distinct from the C-E and basalts from the neighboring CoAxial Segment (Figure 2-7) which is the most strongly depleted in $^{87}Sr/^{86}Sr$ (Smith, 1999; Embley et al., 2000) on the entire ridge. Axial Segment basalts fall between the most depleted basalts of the CoAxial Segment and the C-E basalts (Figure 2-7), similar to the relationships observed in major and trace elements and supporting the hypothesis that these are viable mixing endmembers. Covariation between isotopic and incompatible trace element ratios indicates that much of the incompatible element variability of Axial Segment basalts may be a consequence of mixing between Axial Segment magmas that are similar to those from the CoAxial Segment and C-E magmas. The limited isotopic variability of Axial Segment basalts appears to correlate with trace element ratios such as Zr/Y (Figure 2-7), suggesting that the trace element variations observed are related to source compositional differences and varying mixing proportions from at least two magmatic sources, and are not a result of differences in melting fractions of the same source.

Figure 2-7. Sr and Pb isotopic ratios in basalts from the Axial Segment are generally indistinguishable from the C-E and other segments of the JdFR, with only modest enrichments relative to the very depleted CoAxial Segment. Axial Segment basalts have intermediate radiogenic isotopic compositions between CoAxial and C-E basalts. A correlation between trace element enrichment and radiogenic isotopic enrichment suggests mixing between the ridge and hotspot end-members.

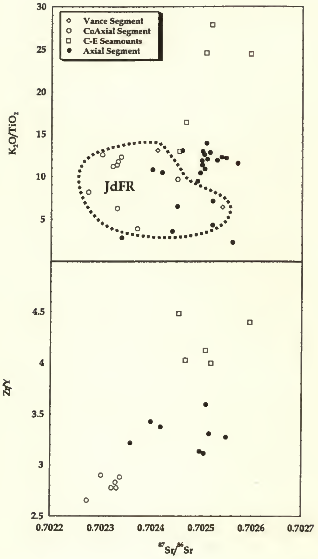
◇ Vance Segment
○ CoAxial Segment
□ C-E Seamounts
● Axial Segment
JdFR
K$_2$O/TiO$_2$
30
25
20
15
10
5
Zr/Y
4.5
4
3.5
3
2.5
0.7022
0.7023
0.7024
0.7025
0.7026
0.7027
^{87}Sr/^{86}Sr

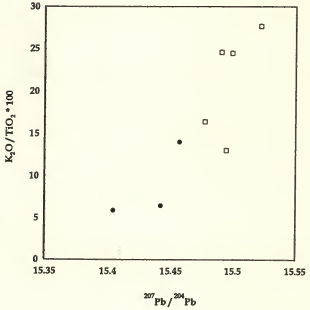
K$_2$O / TiO$_2$ * 100
30
25
20
15
10
5
0
15.35
15.4
15.45
15.5
15.55
^{207}Pb / ^{204}Pb

Discussion

The anomalous geomorphology, bathymetry, and geochemical gradients observed on the Axial Segment provide insight into the physical and chemical consequences of lateral magma migration, crystal fractionation, and mixing. Similar geochemical gradients, albeit on a longer length scale, have been identified on the Reykjanes Ridge and are attributed to the presence of the Iceland hotspot and lateral migration of hotspot magmas along the ridge (e.g. Hart et al., 1973, 1992; Schilling, 1973, Schilling et al., 1983, Elliot et al., 1991). The oversupply of magma to the JdFR appears to be confined to the Axial Segment, as the neighboring Vance and CoAxial Segments exhibit normal, axial rift morphology and chemistry.

The decline in MgO, CaO, and Al_2O_3 along with corresponding increases in TiO_2, FeO, K_2O, and Na_2O along the Axial Segment rift zones with increasing distance from Axial Seamount indicate that more fractionated lavas erupt at greater distances from the hotspot (Figure 2-4a). This is most likely attributed to the fact that the crust becomes progressively thinner and cooler away from the hotspot. Enhanced fractionation is likely due to the "cold edge effect" or equivalent phenomenon (Langmuir and Bender, 1984), which is commonly observed near ridge-transform intersections or at the end of overlapping ridge segments. The abundance of phenocrysts in Ridge Group basalts relative to most

Seamount Group samples, and the general increase in phenocryst abundance with distance from Axial Seamount further supports this hypothesis.

The expected enrichment in incompatible trace element contents resulting from the progressive fractionation postulated in the rift zones is not observed. Instead, there is a negative correlation between trace element and major element gradients in the rift zones, with generally more evolved, but more depleted basalts with distance from the hotspot (Figure 2-4). This observation suggests that the proportion of the depleted mixing component increases with distance from the hotspot, and this effect overprints the enrichment effects of fractionation.

The high degree of scatter exhibited by major and trace element data about calculated LLD, the inverse correlation between major and trace elements in the rift zones, and the positive correlation between radiogenic isotope and trace element ratios indicate that fractionation of a single parent cannot explain the geochemical variability of the Axial Segment suite, and indicates the presence of more than one magmatic source. The high-MgO basalts that do not fall along the regional gradient of the Ridge Group are also depleted in incompatible elements relative to the rest of the suite, and have N-MORB-like REE patterns. These high- MgO basalts show little of the geochemical enrichments observed in the rest of the suite. This suggests that these basalts represent melts from the indigenous Axial Segment MORB source (similar to the neighboring CoAxial and Vance Segment MORB sources), which avoid significant fractional crystallization and mixing with the Cobb hotspot component. The occurence of several examples of the depleted, high-MgO basalt type on Axial Seamount suggests that the magma chamber under the seamount may be transitory or smaller at times, allowing a few MORB-source magmas to avoid mixing during ascent to the surface (Rhodes, 1990).

The results of mixing calculations (Langmuir, 1978) between the most enriched C-E basaltic compositions and the most depleted Axial and CoAxial Segment compositions are shown in Figure 2-8. The results clearly indicate that these are viable mixing end-members for producing the Axial Segment suite, and show the range of hybrid magmas produced by mixing of these components. In addition to mixing, low-pressure fractional crystallization of the hybrid parents that form along the mixing lines is required to account for the remaining geochemical variation observed in the entire Axial Segment suite (Figure 2-8). The mixing relations suggest that the typical low-MgO basalts contain between 30 and 40% of the Cobb hotspot component. This result is in agreement with geophysical studies that suggest a 30% increase in crustal production at Axial Seamount due to the presence of the hotspot (Hooft and Detrick, 1995). The more "enriched" basalts containing the highest proportion of the Cobb component are more depleted than any recovered on the C-E chain (Desonie and Duncan, 1990), a result of the thorough mixing with the more depleted end-member at the ridge. Alkali and light rare earth element (LREE) enrichments decrease with age in the C-E chain, suggesting an increasing influence of the

Figure 2-8. Variable mixing between the Cobb hotspot magmas and the local MORB source, and subsequent fractional crystallization of the hybrid magmas can explain the geochemical variation observed on the Axial Segment. Mixing relations between the Cobb-Eickelberg seamount basalt composition and depleted CoAxial Segment basalts show that mixing between the hotspot magmas and local MORB basalts can explain the trace element variation on the Axial Segment. Thorough mixing of the two end-members has prohibited any lavas with the 'pure' Cobb plume geochemical signature from erupting, and its proportion in Axial Segment lavas is up to ~40%.

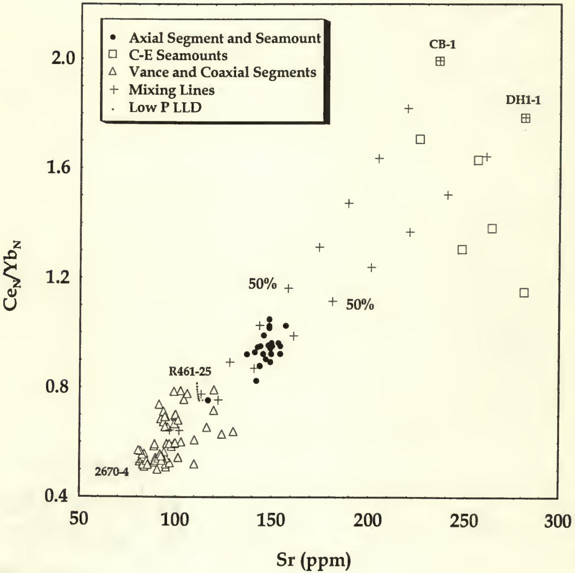
● Axial Segment and Seamount
□ C-E Seamounts
△ Vance and Coaxial Segments
+ Mixing Lines
· Low P LLD
CB-1
DH1-1
50%
50%
R461-25
2670-4
Ce_N/Yb_N
0.4
0.8
1.2
1.6
2.0
50
100
150
200
250
300
Sr (ppm)

depleted MORB source as the ridge approached the hotspot (Desonie and Duncan, 1990).

The gradients in incompatible trace elements along the Axial Segment indicate that the proportion of the MORB mixing component generally increases with distance from the hotspot. One possible explanation for this observation is that the Cobb plume is zoned or has entrained upper mantle materials, and has a more enriched core and progressively more of the depleted component toward its periphery (Figure 2-9a). Close to Axial Seamount, magmas with the highest proportion of the Cobb hotspot component are sampled, but further along the rift zones, progressively more of the depleted material is tapped. The MORB-source material may reside in a mixed sheath around the plume core or as discrete masses entrained in the plume (e.g. Campbell, 1990). A second possible explanation for the gradients is that crustal dikes that emanate from the Axial Seamount magmatic system interact with shallow MORB magma chambers as they propogate down the rift zones during tectonic events (Figure 2-9b). The dikes would initially contain a high proportion of the Cobb end-member, but may become progressively more contaminated with distance down the rift zone due to mixing.

The notable homogeneity of the basalts, both from Axial Seamount and at any given distance from it in the Ridge Group (Figure 2-4a), suggests that they have been homogenized in a large magmatic storage system prior to eruption (West, 2001). It is not clear if all of the lower-MgO magmas originate in the same

Figure 2-9. Models to explain the spatial geochemical trends observed on the Axial Segment. The 'Cold Edge Effect' and smaller magma chambers may lead to enhanced fractional crystallization and more evolved lavas with increasing distance from the hotspot. Trace element trends may result from: (A) tapping into a geochemically zoned plume, with progressively more of the depleted MORB component with increasing distance from the hotspot. The plume may also entrain discrete masses of the MORB-source. (B) The mixing may take place at shallow crustal levels, with propagating dikes penetrating MORB magma lenses as they migrate along the ridge, becoming more contaminated with the depleted component with distance.

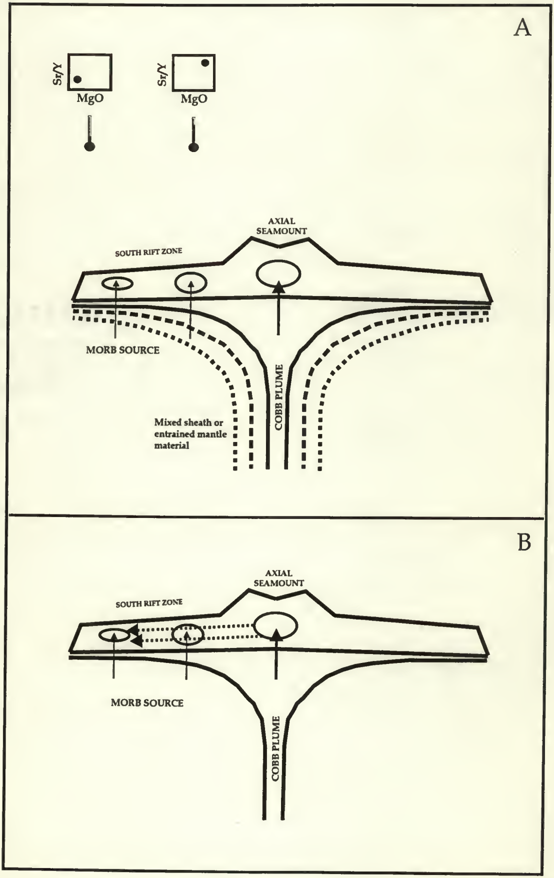
A
Sr/Y
MgO
Sr/Y
MgO
AXIAL SEAMOUNT
SOUTH RIFT ZONE
MORB SOURCE
COBB PLUME
Mixed sheath or entrained mantle material
B
AXIAL SEAMOUNT
SOUTH RIFT ZONE
MORB SOURCE
COBB PLUME

large magma chamber under Axial Seamount and migrate laterally from it and down the length of the Axial Segment rift zones. The clear correlations in major and trace element gradients in the basalts along the rift zones suggests this may be the case, although it is not possible for the progressive effects of fractionation and mixing described above to operate in a closed system. The lateral transport of the hybrid magmas away from the plume and along the rift zones is implied by the shallow bathymetry and the dominance of volcanic features along the length of the Axial Segment, in addition to the spatial gradients in major elements. Moreover, the migration of SOSUS T-phase epicenters supports the hypothesis that magmas can migrate great distances in shallow crustal dikes from the Axial Seamount area.

Rhodes and others (1990) suggested that Axial magmas are derived from the same mantle source as the JdFR, and that differences between the two were based on the depth of melting rather than source differences. Melt initiation at greater depths would account for a higher magma production rate at Axial and many of the subtle geochemical differences between Axial and the ridge. They suggested that the Axial melting column may originate in the spinel peridotite stability field (where Sr is an incompatible element), whereas ridge lavas originate in the shallower plagioclase peridotite stability field, where Sr is more compatible. This would account for the higher Sr content of Axial Seamount lavas. Higher pressure melts are expected to be less saturated in silica and possess higher Na_2O and MgO contents than low-pressure melts (Kushiro, 1968;

Presnall and Hoover, 1987). For the upwelling mantle to intersect the solidus at a deeper level in this model, the mantle supplying Axial must be hotter than at the JdFR, consistent with a thermal plume model. Batiza and Vanko (1983, 1984) and Zindler and others (1984) propose a model in which a smaller degree of partial melting of the upper mantle source that is producing MORB lavas would result in melts that are slightly enriched in alkalis and incompatible elements, but result in essentially a MORB-like isotopic composition. This study has shown differences in incompatible trace element enrichments and particularly radiogenic isotopic ratios that require more than one mantle sources for Axial Segment lavas, and that the most likely additional source is the Cobb hotspot plume.

CHAPTER 3
TEMPORAL GEOCHEMICAL VARIABILITY OF AXIAL SEGMENT LAVAS REVEALED BY RIDGE CAPTURE

Introduction

The Juan de Fuca Ridge (JdFR) is the 490-km-long boundary between the Pacific and Juan de Fuca plates, located in the northeast Pacific off the west coast of North America (Figure 3-1). The JdFR is a medium spreading rate ridge (~2.8 cm/yr half rate; Tivey, 1994), which is migrating to the northwest at 3.1 cm/yr (Karsten and Delaney, 1989). The ridge is divided into seven segments, extending from the Blanco fracture zone in the south where it connects to the Gorda Ridge, to the Nootka fault at its northern terminus where the plate boundary is called the Explorer Ridge.

The Axial Segment is a 100-km-long central segment (Figure 3-1) of the JdFR, which is offset to the west in an en-echelon arrangement with the neighboring Vance and Coaxial Segments. Its southern extension is bifurcated into the Southwest and South Axial Rift Zones (Appelgate, 1990). The Axial Segment is dominated by Axial Seamount, a 2100-m-high volcanic edifice currently being created by the Cobb hotspot. The hotspot has created the Cobb-Eickelberg (C-E) seamount chain, which extends from Axial Seamount to the 33 million year-old Patton Seamount near the Aleutian Trench (Karsten and Delaney, 1989; Desonie and Duncan, 1990; Keller et al., 1997). The seamount

Figure 3-1. The Axial Segment of the Juan de Fuca Ridge is the 100-km-long segment that is currently interacting with the Cobb Hotspot. The interaction has created the large volcanic edifice of Axial Seamount, and a broad, shallow ridge segment dominated by constructional volcanic features. The North and South Rift Zones are the portions of the ridge adjacent to Axial Seamount, and the entire structure is collectively referred to as the Axial Segment. Overlapping spreading centers mark the second-order ridge offsets with the neighboring CoAxial and Vance Segments. Brown Bear Seamount is the hotspot volcano that formed prior to Axial Seamount.

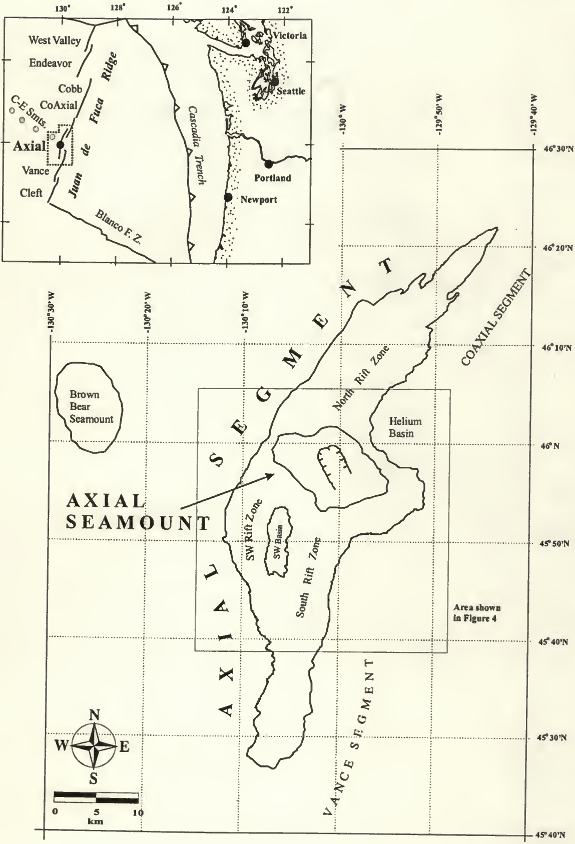
130°
128°
126°
124°
122°
48°
46°
44°
West Valley
Endeavor
Cobb
CoAxial
C-E Smts.
Axial
Vance
Cleft
Juan de Fuca Ridge
Cascadia Trench
Blanco F. Z.
Victoria
Seattle
Portland
Newport
-130° W
-129° 50' W
-129° 40' W
46° 30'N
46° 20'N
46° 10'N
46° N
45° 50'N
45° 40'N
45° 30'N
45° 40'N
-130° 30' W
-130° 20' W
-130° 10' W
AXIAL SEGMENT
COAXIAL SEGMENT
VANCE SEGMENT
North Rift Zone
Helium Basin
Brown Bear Seamount
AXIAL SEAMOUNT
SW Rift Zone
SW Basin
South Rift Zone
Area shown in Figure 4
N
W
E
S
0
5
10
km

chain lies along a trend that is consistent with predicted absolute motions of the Pacific Plate indicating that the hotspot is a fixed mantle melting anomaly. The chain is parallel to the trend of the Hawaiian seamount chain, and C-E seamounts become progressively younger to the southeast as they approach the hotspot. Axial Seamount is anomalous in that it erupts relatively depleted, MORB-like lavas without the distinct elemental and isotopic enrichments found in lavas from other hotspot-related seamounts and islands (Rhodes et al., 1990; Desonie and Duncan, 1990).

The complex interaction between seafloor spreading and hotspot volcanism has created distinct bathymetric and morphological features on the Axial Segment. It has the highest-standing bathymetry on the entire JdFR, with average depths that are 250-750 m shallower than the other segments (Figure 3-2). The morphology of the Axial Segment changes with distance from the hotspot; close to Axial Seamount, it is shallowest and has an inflated, corrugated appearance, composed of parallel-trending sets of thin, linear ridges that are likely dike-fed volcanic constructs (Appelgate, 1990). These ridges are similar to volcanic ridges on the submarine extension of the Kilauea rift zone (Puna Ridge), which are inferred to have erupted along linear vents where dikes intersect the surface (Fornari et al., 1978). Near it's north and south distal ends, the Axial Segment deepens and is characterized by small (typically <2km in diameter) volcanic cones and mounds that are superimposed on more irregular volcanic ridges. No structurally defined spreading axis or major tectonic features of any

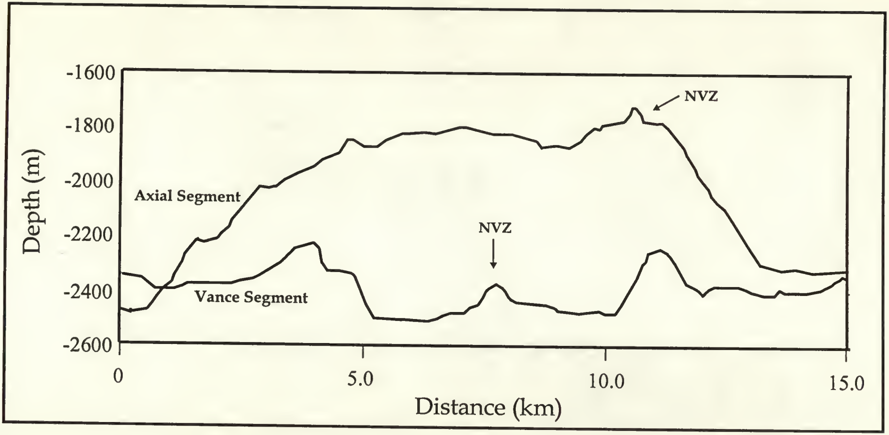

Figure 3-2. Topographic cross-sections of the Axial and Vance Segments. Note the symmetrical profile of the Vance Segment, with a centralized axial volcanic ridge identifying the neo-volcanic zone (NVZ) within a well-defined axial graben. The Axial Segment has much shallower bathymetry due to magmatic oversupply from the hotspot, and its NVZ is off-center to the east. Bathymetry gradually increases from west to east as well, reflecting ridge capture.

kind have been identified in high-resolution sonar imagery of the ridge (Appelgate, 1990). The dominance of volcanic features is atypical for the JdFR, as the rest segments are characterized by a majority of tectonic features, including well-defined axial graben or valleys. (Johnson and Holmes, 1989; Van Wagoner and Leybourne, 1991; Smith et al., 1994; Perfit and Chadwick, 1998; Embley et al. 2000). In spite of the medium spreading rate on the JdFR (6 cm/yr full rate; Johnson and Embley, 1990), the morphology of the Axial Segment is similar to the broad, inflated axial high that is more commonly observed at fast spreading ridges (Phipps Morgan and Chen, 1993), which is likely an effect of excess magma supply from the hotspot. Axial high morphology has also developed on the Kolbeinsy and Reykjanes Ridges in proximity to the Iceland hotspot, in spite of the slow spreading rate of the Mid-Atlantic Ridge (Searle and Laughton, 1981). The morphology of intermediate spreading rate ridges (2-3 cm/yr) may be particularly sensitive to magma supply, varying between the rift morphology typical of slow spreading ridges to the axial high typical of fast spreading ridges. The transition in axial morphology of medium rate ridges depends on the balance between the heat supplied by intrusion and its removal by hydrothermal circulation (Phipps Morgan and Chen, 1993; Hooft and Detrick, 1995). The shallow bathymetry of the Axial Segment suggests that hotspot magmas are channeled laterally along the segment (Vogt and Johnson, 1975; Yale and Phipps Morgan, 1998). The infiltration of the hotspot magmas leads to an oversupply along the ridge and allows hotspot and shallow MORB magmas to mix (see Chapter 2).

Although the characteristics of the Axial Segment are very different from the rest of the JdFR due to its interaction with the hotspot, it is likely an integral part of the JdFR spreading system and not an isolated volcanic rift system similar to the Kilauea volcano rift zones in Hawaii (Hammond and Delaney, 1985). The segment fills the approximately 60-km gap between the southern end of the Coaxial segment and the northern end of the Vance segment (Figure 3-1), and it overlaps these segments in the manner of an overlapping spreading center, with the ends of the segments curving toward each other (Lonsdale, 1985; Embley et al., 1990).

Migration of the JdFR system brought it to the vicinity of the Cobb hotspot during the Brunhes magnetization period (Figure 3-3a). The Vance and Coaxial segment trends are collinear with the centerline of the normal-polarity Brunhes pattern, but the Axial Segment is offset to the west by about 15 km (Tivey and Johnson, 1990). This indicates that active spreading linked the Vance and Coaxial segments in early- to mid mid-Bruhnes time, but ceased when the section of ridge between them was abandoned and spreading began on the Cobb hotspot, creating the Axial Segment (Figure 3-3b). Although the JdFR was still 15-20 km to the west of the hotspot, magnetic anomaly data reveal that a central section of the ridge "jumped" to the location of the hotspot 0.2-0.7 m.y. ago (Delaney et al., 1981; Hammond and Delaney, 1985; Karsten and Delaney, 1989;

Figure 3-3. History of the interaction of the Juan de Fuca Ridge with the Cobb Hotspot. (A) Prior to about 0.4 Ma, the ridge was approaching the hotspot from the southeast, migrating at about 3 cm/yr. Brunhes crust is shown in gray, Matuyama crust in white. (B) A central portion of the ridge was abandoned, and spreading was initiated over the Cobb hotspot, creating the Axial Segment. Small islands of Matuyama crust were isolated between the new and old spreading centers. (C) In the current situation, capture of the Axial Segment has led to the production of abandoned volcanic ridges to the west of the neo-volcanic zone (NVZ), leading to the apparent asymmetrical properties of the segment. Continued migration of the Juan de Fuca Ridge will re-link the Vance and CoAxial Segments with the Axial Segment in about 0.5 my.

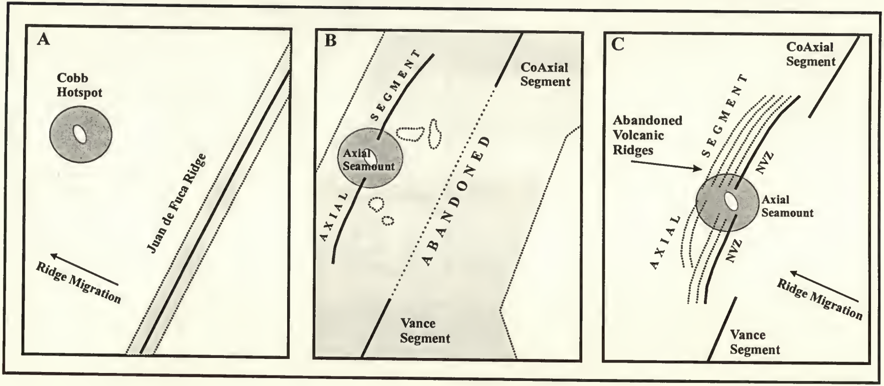
A
Cobb Hotspot
Juan de Fuca Ridge
Ridge Migration
B
AXIAL SEGMENT
Axial Seamount
ABANDONED
CoAxial Segment
Vance Segment
C
CoAxial Segment
Abandoned Volcanic Ridges
AXIAL SEGMENT
NVZ
Axial Seamount
NVZ
Ridge Migration
Vance Segment

Tivey and Johnson, 1990). The age of the interaction is revealed by the off-center location of the Axial Segment on the Brunhes magnetic pattern, as well as the presence of Matuyama negative-polarity crust (e.g. Helium Basin) within the Brunhes region age crust (Figure 3-3b), trapped between the abandoned and current spreading ridges. This relocation event, and similar events at other ridge-hotspot interactions (Small, 1995; Hey and Vogt, 1977), suggests that as migrating ridges approach a hotspot, the regional extensional stresses on the plates may transfer spreading to a position over the hotspot due to the thermal and mechanical weakness imposed on the lithosphere by the plume.

This paper presents the results of a study of regional age relationships, ridge morphology, and basalt geochemistry on the Axial Segment, in an effort to understand the tectonic and magmatic processes that have taken place since the interaction of these two major geological features began. The Axial Segment provides a unique opportunity to study the first few hundred thousand years of a ridge-hotspot interaction, and can offer insight into the universality of paradigms developed from studies of the well-documented Iceland-Mid-Atlantic ridge interaction.

Sample Recovery and Geological Observations

The goals of this study were to identify the location of the active plate boundary on the Axial Segment using basalt ages, ridge bathymetry and morphology, and to investigate the tectonic processes and geochemical variability resulting from the JdFR-Cobb hotspot interaction. To these ends, an extensive basalt sampling campaign was conducted as part of the 1998-2002 NOAA-sponsored New Millennium Observatory (NeMO) research program, which was devoted to geological, biological, and hydrothermal studies of the results of the 1998 eruption of Axial Seamount (NeMO Cruise reports, 1998-2002). Basalt samples have been collected from the Axial Seamount caldera and adjacent flanks by the Remotely Operated Platform for Ocean Science (ROPOS) submersible during the NeMO cruises, operated from the RV Ronald Brown and RV Thomas Thompson. For this study, a more regionally extensive sampling campaign was accomplished along the North and South Rift Zones of the Axial Segment with wax corers during the NeMO project as well (Figure 3-4). To ascertain intra-segment variations in basalt ages and geochemistry, and to elucidate the relative roles of Cobb hotspot and local MORB magmas in Axial lavas, 139 wax core samples were acquired in a high-density pattern both along and across the strike of the Axial Segment. Out of logistical necessity, the majority of these were acquired in the South Rift Zone within 20 km of the 1998 eruption site.

The lavas in the 1998 eruption issued from a dike or dike system that extended along the South Rift Zone about 10 km from the southeastern corner of the Axial Seamount caldera, along the eastern side of the Axial Segment. The basalts collected from these flows were all very fresh, glassy, and free of associated sediments as would be expected from such a recent eruption, but wax core samples collected elsewhere on the Axial Segment exhibit varying degrees

Figure 3-4. Age relationships on the Axial Segment are revealed by the glassiness, manganese coating, and sediment volume associated with wax core samples. The freshest basalts (Age 1) were recovered exclusively on the eastern side of the ridge, and a general progression of older samples to the west indicate the neo-volcanic zone (NVZ) is offset to the east from the centerline of the topographic ridge. This hypothesis is supported by bathymetric and sonar reflectivity data, as well as the asymmetric location of the 1998 lava flow. A few of the most weathered/altered samples (Age 3) were recovered on the extreme eastern side of the ridge in the South Rift Zone, indicating older lavas to the east of the NVZ. Intermediate-age samples (Age 2) overlap the entire sampling area, and are not shown.

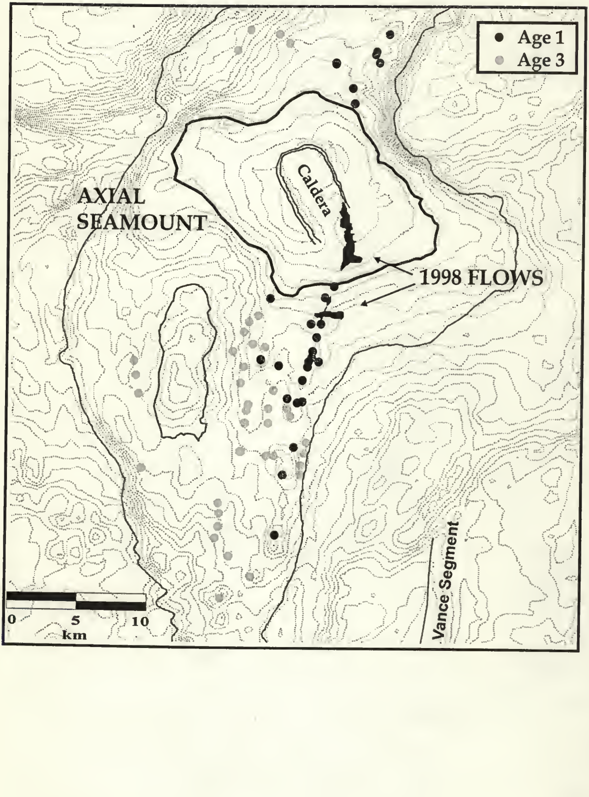
● Age 1
● Age 3
AXIAL SEAMOUNT
Caldera
1998 FLOWS
Vance Segment
0
5
10
km

of freshness, likely reflecting variations in their eruption age. The wax core samples retrieved from the Axial Segment were given a qualitative age classification (1-3) upon retrieval of the sampler from the ocean floor (Figure 3-4); a "1" denoting the freshest, glassiest basalts with little weathering and/or Mn-coating and the least amount of associated pelagic sediment (including sediments embedded in the coring wax), a "2" for intermediate-age samples, and a "3" for basalts with the least glass, thickest Mn coating and greatest amounts of associated sediment, suggesting the longest time period since their eruption. Similar qualitative age classification schemes have been used in previous studies of basalt ages at Axial Seamount (Embley et al., 1990; Hammond, 1990), and it is used here to gain insight into the spatial and temporal evolution of eruptive activity on the Axial Segment.

Basalts retrieved from the eastern part of the Axial Segment (North and South Rift Zones) are the glassiest and freshest, whereas samples from progressively further west across the strike of the ridge are generally less glassy and associated with thicker Mn-coatings and more sediment cover (Figure 3-4). Wax core sampling attempts on the westernmost part of the ridge met with limited success due to thick sediment cover, also implying an older surface. These relative age relations suggest that the basalts are youngest on the eastern side of the North and South Rift Zones of the Axial Segment, becoming progressively older toward the west (perpendicular to the strike of the ridge). Although the majority of the basalt samples were collected in the South Rift Zone of the Axial Segment (Figure 3-4), the age pattern is also clearly present in the North Rift Zone as well. This asymmetrical pattern is inconsistent with a normal spreading ridge but is compatible with the east-of-center locations of the 1998 eruption and a recent eruption documented in the north rift zone, as well as the off-center location of the Axial Seamount caldera (Figure 3-4). This age interpretation is supported by high-resolution sonar mapping, which has revealed high backscatter lavas interpreted to be fresh constructional volcanic ridges and flows in the eastern half of the South Rift Zone, and low backscatter, more sediment-covered and older terrain to the west (Appelgate, 1990). These differences in sonar backscatter intensity are interpreted to reflect changes in sediment thickness and age, and the boundary between younger and older surfaces is gradational and indistinct. Tectonic structures are largely absent in the South Rift Zone in sonar imagery, but post-eruptive faults with trends mimicking the volcanic ridges are prevalent in the SW Basin and on the SW Rift Zone. These observations suggest that the eastern sides of the rift zones are the only areas exhibiting recent volcanic activity, and that the plate boundary of the Axial Segment is located there. The absence of an unequivocal structural expression of the plate boundary is likely due to high rates of volcanism that buries large faults as fast as they form.

Mid-ocean ridges typically have a symmetrical cross-section, with a centrally located neovolcanic zone (NVZ), either within a structurally-defined central rift or graben (e.g. the Vance Segment, Figure 3-2), or atop a symmetrical broad volcanic arch (axial high) in the case of fast-spreading ridges (Perfit and Chadwick, 1998). In addition to the anomalous shallow bathymetry of the Axial Segment, it also has an asymmetric across-axis bathymetric profile, with the shallowest bathymetry on the eastern part of the ridge, corresponding with the locations of the freshest basalt flows (Figure 3-2). This association indicates the thermal and/or isostatic uplift associated with the NVZ is also off-center on the eastern side of the Axial Segment. This is likely a consequence of thermal buoyancy from a narrow column of buoyant material (e.g. Madsen et al. 1984, Wilson, 1992), horizontal viscous shear stress driven by plate separation (Eberle and Forsythe, 1998), or accretional bending stresses (Buck, 2001). The bathymetric gradient to the west is similar to the gradients observed at all mid-ocean ridges, and likely results from subsidence due to the gradual conductive cooling of the lithosphere as it moves away from the NVZ (Cochran and Buck, 2001).

Ridge Capture

Several mid-ocean ridge systems that are currently interacting with hotspots (e.g. Iceland, Discovery, Galapagos) show evidence of discrete ridge jumps in the direction of the hotspot (Ward, 1971; Saemundsson, 1974; Hey and Vogt, 1977; Small, 1995). The most likely cause for this is thermal weakening of the ridge flank by the plume, resulting in the relocation of the axis of spreading back over the plume. Wax-model study studies (Leary et al., 1991) have also shown that sections of ridges jump to and reside over hotspots as the ridge migrates toward a fixed plume. "Capture" of the segment continues for some time after the adjoining sections of the ridge pass by, as is the case at Iceland (Hardarson, 1997).

The repeated eastward relocation of the active rift zone over the Iceland hotspot in response to WNW migration Mid-Atlantic Ridge has been a significant geological process on the island for at least the last 15 m.y. (Hardarson, 1997). Two previous rift zones can be identified in western Iceland; the Northwest Iceland Rift and the Snaefellsnes Rift, each abandoned by periodic rift relocations to the east. Rift relocation is a complex process, with volcanic and tectonic activity initiated on the new rift several million years before the old rift becomes extinct (Hardarson, 1997). The current neovolcanic zone in Iceland is itself in the process of relocating, which will ultimately lead to the abandonment of the still active Western Volcanic Zone and fully transfer activity to the Eastern and Northern Volcanic Zones (Oskarsson et al., 1985), 100 km to the east over the center of the hotspot.

The asymmetries in morphologic, volcanic and age properties of the Axial Segment presented in the previous section support the hypothesis that it has been captured by the Cobb hotspot. Active spreading first jumped from the JdFR to the northwest to lie directly over the hotspot, and has since remained fixed relative to the hotspot as the rest of the plate boundary has continued to migrate to the northwest (Figures 3-3c and 3-5). This has led to an apparent eastward migration of volcanism (relative to the center of the Axial Segment) over time,

Figure 3-5. Capture of the Axial Segment by the Cobb Hotspot has led to the asymmetrical growth of the segment, and the majority of the new crust produced since the capture is transferred to the Pacific Plate to the west. The result of ~3 cm/yr (half-rate) ridge spreading (T1A) and ~3 cm/yr migration (T1B) after a given time period leads to the removal of most of the new crust away from the hotspot. The captured neo-volcanic zone remains over the hotspot or jumps back to it, however, and spreading persists there (T2). Continued spreading and migration (T3) has lead to the creation of an asymmetric ridge segment. The shallowest bathymetry on the ridge is also on the eastern side, due to progressive cooling of the older crust to the west.

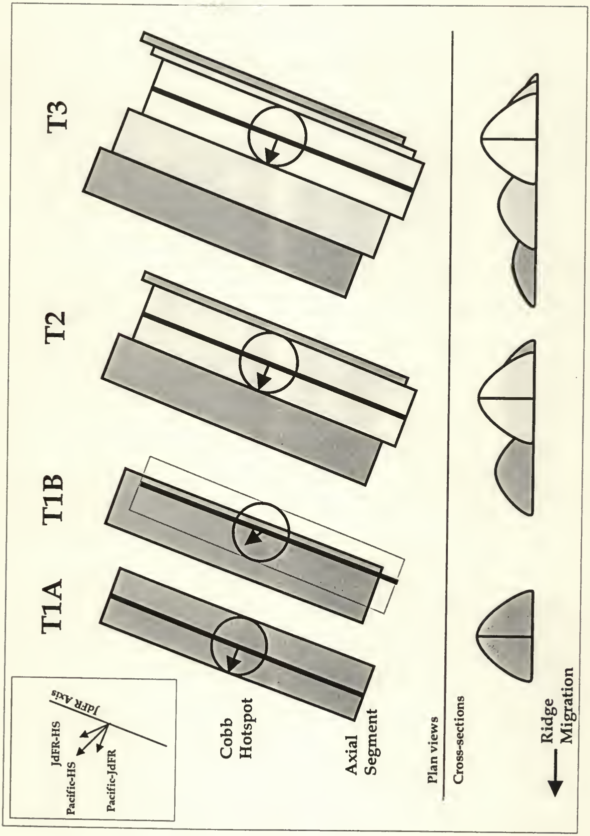
T1A
T1B
T2
T3
JdFR Axis
JdFR-HS
Pacific-HS
Pacific-JdFR
Cobb Hotspot
Axial Segment
Plan views
Cross-sections
Ridge Migration

due to the formation of successive rift zones that migrate to the west with the Pacific Plate when they are abandoned. This would lead to progressively older basalt eruption ages from east to west, and is consistent with the geological observations discussed above. The similarity in the magnitude of the plate migration and spreading vectors (Karsten and Delaney, 1989), coupled with a 20° azimuthal difference results in the transferal of most of the new crust produced by Axial Segment spreading to the Pacific Plate when the zone of active spreading migrates or jumps back over the hotspot (Figure 3-5). A small amount, however, remains on the Juan de Fuca Plate, and may be represented by several "Age 3" samples on the extreme east side of the South Rift Zone (Figure 3-4). Calculations using plate motion vectors predict this sliver of crust produced by the Axial Segment over the 0.4 my due to ridge capture should be just over 1 km wide, and much of it may be buried by younger lavas.

The ridge relocation process appears to occur more rapidly at Axial Seamount than on Iceland, leading to the development of a single, wide ridge on the northern half of the segment instead of isolated rift zones. The southern half of the Axial Segment is bifurcated (Southwest and South Axial Rift Zones of Appelgate, 1990), suggesting a 3-4 km jump of the spreading center, creating the Southwest Basin between the two arms of the ridge (Figures 3-1 and 3-4). It is not clear why a similar feature did not form on the northern half of the segment, but the 12-km total width of the two arms of the South Rift Zone is the same as the uniform North Rift Zone, and was likely produced in the same amount of time.

An understanding of the modified crustal accretion mechanism due to capture of the Axial Segment can allow for a reassessment of the age of its interaction with the hotspot. Assuming a 3 cm/yr half-spreading rate (azimuth 315°), 3.1 cm/yr migration rate (azimuth 335°), and a 12-km-wide ridge, the captured Axial Segment produces ~2.8 cm/yr of new Pacific crust (Figure 3-5), and results in a net Pacific Plate motion to the NW of 4.4 cm/yr (Desonie and Duncan, 1986; Karsten and Delaney, 1989). About 430,000 years (12 km/2.8 cm/yr = 428,571 yrs) is required for the captured Axial Segment to produce 12 km of overthickened crust to the west of the current neovolcanic zone. This age for the initiation of ridge-hotspot interaction is consistent with ages suggested by previous workers (Delaney et al., 1981; Hammond and Delaney, 1985; Karsten and Delaney, 1989; Tivey and Johnson, 1990) based on magnetic anomaly data.

Temporal Geochemical Variations

The capture of the Axial Segment and the resulting spatial segregation of basalts with different ages provides an opportunity to examine the geochemical variability of the Cobb hotspot-JdFR magmatic system over the history of their interaction. Major and trace element abundances of samples collected by wax core and ROV on the ridge were determined (Table 3-1) to investigate regional geochemical variations. Electron microprobe and X-ray fluorescence (XRF)

Table 3-1. Age classifications for rock samples from the Axial Segment. Major element analyses from electron microprobe[1].

Sample	Longitude	Latitude	Age Class	SiO_2	Al_2O_3	TiO_2	FeO	MnO	MgO	CaO	K_2O	Na_2O	P_22O_5	Total
98-RC-01	-129.9970	45.8922	1	50.3	14.4	1.52	10.7	0.21	7.15	11.7	0.19	2.95	0.14	99.3
98-RC-03	-130.0130	45.8287	1	50.0	14.1	1.59	11.1	0.21	7.00	11.6	0.20	3.03	0.16	99.0
98-RC-04	-130.0117	45.8325	1	50.2	14.2	1.61	11.2	0.20	7.10	11.7	0.19	2.86	0.15	99.4
98-RC-05	-130.0053	45.8327	1	49.9	14.9	1.37	10.2	0.20	7.66	11.9	0.14	2.82	0.12	99.2
98-RC-06	-130.0097	45.8363	1	50.0	14.1	1.59	11.1	0.21	7.02	11.6	0.21	2.96	0.16	99.1
98-RC-11	-130.0062	45.8505	1	50.1	14.3	1.52	10.6	0.20	7.16	11.9	0.20	2.94	0.13	99.0
98-RC-12	-130.0088	45.8400	1	50.2	14.2	1.63	11.2	0.22	6.98	11.6	0.20	3.02	0.18	99.5
98-RC-15	-130.0318	45.8943	1	50.3	14.3	1.60	11.2	0.22	6.92	11.7	0.20	2.86	0.16	99.5
98-RC-23	-130.0417	45.8803	1	50.3	14.3	1.50	10.9	0.21	7.17	11.9	0.19	2.87	0.13	99.6
98-RC-26	-130.0485	45.8343	1	48.7	16.3	1.07	9.9	0.20	8.53	11.8	0.11	2.56	0.11	99.4
98-RC-28	-130.0250	46.0075	1	50.6	14.5	1.52	10.5	0.20	7.09	11.3	0.24	3.07	0.17	99.2
98-RC-35	-130.0113	45.8612	1	50.2	14.3	1.45	10.6	0.20	7.32	12.0	0.17	2.83	0.13	99.1
98-RC-36	-129.9638	45.8263	1	49.5	15.2	1.34	10.6	0.20	7.69	12.0	0.14	2.80	0.12	99.5
98-RC-39	-130.0028	45.8608	1	50.1	14.4	1.51	10.5	0.20	7.27	11.9	0.19	2.85	0.14	99.1
98-RC-46	-130.0308	45.7483	1	47.8	17.2	1.01	9.8	0.16	9.27	11.4	0.07	2.52	0.05	99.3
98-RC-49	-129.9630	46.0623	1	57.7	12.3	1.79	13.6	0.32	1.82	5.8	0.90	2.29	0.70	97.2
99-RC-100	-129.9600	46.0560	1	55.1	12.8	1.99	13.2	0.29	2.26	6.1	0.84	4.27	0.68	97.5
99-RC-101	-129.9520	46.0770	1	53.8	12.1	2.19	14.6	0.32	2.40	6.5	0.71	4.12	0.96	97.7
99-RC-50	-130.0000	45.8810	1	49.5	15.5	1.35	10.0	0.17	8.05	12.1	0.12	2.85	0.12	99.7
99-RC-81	-130.0230	45.7690	1	49.9	14.2	1.38	10.3	0.19	7.40	12.6	0.12	2.81	0.13	99.0
99-RC-90	-130.0350	45.8300	1	49.8	13.9	1.59	11.1	0.21	7.25	11.7	0.17	3.01	0.13	98.9
99-RC-91	-130.0280	45.8050	1	49.7	14.0	1.54	10.7	0.21	7.41	12.1	0.14	3.00	0.14	98.9
99-RC-92	-130.0210	45.8020	1	49.8	14.1	1.54	10.7	0.21	7.36	11.9	0.18	2.84	0.15	98.7
99-RC-93	-130.0170	45.8030	1	49.8	14.1	1.52	10.6	0.20	7.08	11.9	0.17	2.92	0.14	98.5
99-RC-97	-130.0370	45.7030	1	47.9	16.7	0.98	9.6	0.17	9.37	11.6	0.04	2.58	0.05	99.0
99-RC-99	-129.9620	46.0640	1	58.3	12.5	1.57	12.9	0.29	1.56	5.4	0.90	3.67	0.63	97.7
00-RC-113	-129.9825	45.9165	1	49.6	14.5	1.51	10.5	0.18	7.57	12.0	0.19	2.89	0.15	99.1
00-RC-117	-130.0168	45.8190	1	50.0	14.4	1.54	10.6	0.21	7.32	12.1	0.20	2.87	0.16	99.3
00-RC-118	-129.9684	45.9167	1	49.7	14.6	1.48	10.2	0.20	7.27	12.2	0.18	2.84	0.15	98.9
00-RC-119	-129.9928	46.0562	1	47.0	17.2	1.32	8.9	0.17	8.58	11.7	0.11	2.81	0.12	98.0

[1] Microprobe analyses performed at USGS, Denver, Colorado

Samples with no geochemical data: no recovery, whole rock samples with no glass, or high analytical errors

Table 3-1. Continued.

Sample	Longitude	Latitude	Age Class	SiO_2	Al_2O_3	TiO_2	FeO	MnO	MgO	CaO	K_2O	Na_2O	P_22O_5	Total
R465-01	-129.9862	45.8693	1	50.1	14.2	1.53	10.9	0.19	7.04	11.7	0.20	2.98	0.14	99.1
R465-02	-129.9863	45.8695	1	50.2	14.2	1.57	10.9	0.20	7.05	11.6	0.20	2.97	0.14	99.0
R494-01	-130.0042	45.8583	1	50.1	14.3	1.53	10.6	0.19	7.03	12.3	0.18	2.84	0.15	99.2
R494-04	-130.0041	45.8624	1	50.1	14.4	1.56	10.8	0.20	7.11	11.8	0.18	2.90	0.15	99.3
R494-05	-130.0041	45.8624	1	50.1	14.5	1.53	10.9	0.19	7.14	11.9	0.18	2.91	0.15	99.5
R494-06	-130.0041	45.8624	1	50.1	14.4	1.55	10.7	0.18	7.15	12.0	0.19	2.86	0.15	99.3
R494-08	-129.9958	45.8782	1	50.1	14.5	1.57	10.7	0.21	7.10	12.0	0.18	2.88	0.14	99.4
R546-02	-130.0037	45.8631	1	50.1	14.4	1.53	10.6	0.20	7.38	12.3	0.19	2.85	0.15	99.6
R554-02	-129.9982	45.8739	1	49.9	15.0	1.32	10.0	0.20	7.85	12.4	0.13	2.73	0.13	99.7
R554-03	-129.9983	45.8739	1	48.5	14.4	1.55	10.6	0.20	7.76	12.6	0.15	2.77	0.14	98.7
R554-04	-130.0003	45.8686	1	49.3	14.5	1.53	10.6	0.19	7.58	12.1	0.19	2.86	0.15	98.9
R554-05	-130.0015	45.8665	1	49.2	14.4	1.53	10.5	0.21	7.54	12.2	0.19	2.84	0.16	98.8
R554-06	-130.0015	45.8665	1	49.1	14.3	1.52	10.6	0.18	7.54	12.0	0.19	2.84	0.16	98.5
01-RC125a	-130.0368	45.7632	1											
01-RC127	-129.9615	45.9190	1											
01-RC129	-130.0260	46.0062	1											
01-RC130	-129.9928	46.0553	1											
01-RC131	-129.9795	46.0367	1											
01-RC132	-129.9943	46.0282	1											
01-RC133	-129.9790	46.0248	1											
01-RC134	-130.0232	46.0232	1											
01-RC135	-130.0248	46.0013	1											
01-RC136	-130.0432	46.0000	1											
01-RC138	-129.9547	45.9548	1											
98-RC-02	-129.9758	45.8535	2	50.0	14.1	1.65	11.3	0.21	6.94	11.6	0.23	2.96	0.15	99.0
98-RC-10	-129.9633	45.9615	2	50.1	14.8	1.41	10.5	0.20	7.49	11.6	0.16	2.83	0.14	99.2
98-RC-13	-130.0268	45.8440	2	50.1	14.1	1.50	10.9	0.21	7.15	11.8	0.19	2.86	0.15	98.9
98-RC-18	-130.0193	45.8087	2	50.0	14.0	1.65	11.3	0.21	6.91	11.6	0.21	3.07	0.15	99.1
98-RC-21	-130.0813	45.6367	2	48.2	16.6	1.31	10.1	0.18	8.76	11.2	0.09	2.75	0.10	99.4
98-RC-22	-130.0467	45.8707	2	50.4	14.1	1.63	11.3	0.22	6.84	11.7	0.20	2.95	0.17	99.4
98-RC-24	-130.0380	45.8527	2	50.1	14.0	1.62	11.5	0.22	6.85	11.5	0.21	3.00	0.16	99.1
98-RC-27	-130.0258	45.8342	2	49.9	14.2	1.53	10.9	0.21	7.18	11.9	0.17	2.98	0.14	99.2
98-RC-30	-130.0375	45.8212	2	49.9	13.8	1.66	11.7	0.23	6.71	11.5	0.20	3.01	0.14	98.9
98-RC-31	-130.0277	45.8167	2	50.0	14.3	1.71	11.8	0.23	6.58	11.1	0.24	3.17	0.18	99.3

Table 3-1. Continued.

Sample	Longitude	Latitude	Age Class	SiO_2	Al_2O_3	TiO_2	FeO	MnO	MgO	CaO	K_2O	Na_2O	P_22O_5	Total
98-RC-32	-130.0130	45.8133	2	50.1	14.2	1.62	11.0	0.21	7.13	11.9	0.20	2.93	0.16	99.4
98-RC-33	-130.0315	45.8437	2	50.2	13.9	1.65	11.5	0.22	6.84	11.7	0.20	2.92	0.15	99.2
98-RC-34	-130.0475	45.8403	2	50.0	13.7	1.74	11.9	0.22	6.54	11.3	0.23	3.03	0.18	99.0
98-RC-41	-130.0290	45.8893	2	50.4	14.4	1.54	10.8	0.21	7.21	11.8	0.19	2.91	0.15	99.6
98-RC-42	-129.9965	46.0227	2	50.1	14.3	1.62	10.8	0.22	7.14	11.7	0.21	2.97	0.18	99.3
98-RC-44	-130.0500	45.8275	2	50.2	13.9	1.59	11.5	0.23	6.86	11.4	0.18	2.99	0.15	99.0
98-RC-45	-130.0602	45.8053	2	49.9	14.0	1.59	11.3	0.22	6.97	11.7	0.21	2.91	0.17	99.0
98-RC-47	-129.9828	46.0488	2	50.0	14.2	1.49	10.8	0.20	7.25	11.9	0.18	2.84	0.13	99.1
98-RC-48	-129.9678	46.0660	2	50.1	14.1	1.55	11.0	0.22	7.07	11.8	0.20	2.88	0.15	99.1
99-RC-51	-130.0150	45.8790	2	50.1	14.1	1.59	11.1	0.22	6.93	11.7	0.17	2.88	0.16	99.1
99-RC-52	-130.0210	45.8760	2	49.9	14.5	1.50	10.9	0.21	7.15	12.1	0.15	2.88	0.15	99.3
99-RC-53	-130.0300	45.8620	2	49.9	14.4	1.53	10.9	0.21	7.40	12.0	0.15	2.85	0.15	99.6
99-RC-56	-130.0820	45.6920	2	50.0	13.8	1.77	12.3	0.23	6.35	11.3	0.18	3.13	0.17	99.3
99-RC-58	-130.0640	45.7570	2	49.9	14.0	1.71	11.6	0.24	6.71	11.8	0.18	2.97	0.16	99.2
99-RC-60	-130.0630	45.7770	2	49.9	13.9	1.65	11.4	0.21	6.70	11.9	0.19	2.99	0.16	98.9
99-RC-63	-130.0530	45.8570	2	49.9	14.0	1.57	11.0	0.20	6.94	12.0	0.18	2.88	0.15	98.7
99-RC-68	-130.0580	45.8360	2	49.9	13.7	1.70	11.5	0.22	6.73	11.6	0.20	2.92	0.18	98.7
99-RC-69	-130.0610	45.8420	2	50.0	14.3	1.51	10.7	0.21	7.20	12.2	0.19	2.67	0.13	99.1
99-RC-70	-130.0190	45.7340	2	50.0	14.4	1.45	10.5	0.21	7.21	12.2	0.13	2.80	0.14	98.9
99-RC-71	-130.0180	45.7440	2	50.1	14.2	1.51	10.7	0.22	7.04	12.2	0.14	2.82	0.14	99.1
99-RC-73	-130.0070	45.7550	2	49.4	14.3	1.45	10.4	0.21	7.28	12.2	0.17	2.73	0.14	98.4
99-RC-76	-130.0010	45.7700	2	49.5	14.3	1.48	10.4	0.21	7.21	12.2	0.18	2.72	0.15	98.3
99-RC-77	-130.0070	45.7810	2	49.4	14.0	1.62	11.2	0.21	6.87	11.9	0.17	2.94	0.16	98.5
99-RC-78	-129.9990	45.7760	2	49.5	14.3	1.48	10.4	0.21	7.25	12.2	0.18	2.76	0.15	98.3
99-RC-79	-130.0050	45.7620	2	48.8	14.3	1.44	10.3	0.21	7.31	12.2	0.17	2.72	0.15	97.7
99-RC-84	-130.0600	45.8470	2	49.8	14.1	1.54	10.9	0.22	7.06	12.0	0.18	2.86	0.15	98.9
99-RC-85	-130.0600	45.8530	2	50.0	14.0	1.55	10.8	0.20	7.09	12.0	0.17	2.85	0.15	98.8
99-RC-89	-130.0240	45.8250	2	50.1	13.9	1.64	11.1	0.20	6.75	11.8	0.20	3.01	0.18	98.8
99-RC-98	-130.0340	45.7160	2	48.6	16.1	1.40	9.6	0.18	8.13	11.8	0.08	3.01	0.09	99.1
00-RC-116	-130.0317	45.8283	2	49.9	14.0	1.71	11.6	0.22	6.88	11.7	0.21	2.94	0.17	99.2
00-RC-120	-130.0093	46.0619	2	49.3	15.5	1.33	9.7	0.21	7.80	12.2	0.13	2.78	0.11	99.1
00-RC-122	-129.9848	45.8403	2	48.2	16.7	1.38	9.2	0.18	8.06	11.9	0.13	2.96	0.12	98.8
00-RC-123	-129.9983	45.8398	2	48.8	15.8	1.29	9.7	0.18	8.04	12.1	0.12	2.72	0.11	98.9
98-RC-14	-130.0250	45.9408	2											

Table 3-1. Continued.

Sample	Longitude	Latitude	Age Class	SiO_2	Al_2O_3	TiO_2	FeO	MnO	MgO	CaO	K_2O	Na_2O	P_22O_5	Total
98-RC-19	-130.0413	45.6920	2											
98-RC-29	-130.0075	45.9947	2											
01-RC124	-130.0307	45.7482	2											
01-RC126	-130.0317	45.9265	2											
01-RC128	-129.9197	45.9085	2											
01-RC137	-129.9708	45.9875	2											
98-RC-07	-130.0597	45.7867	3	50.0	14.0	1.57	11.2	0.21	6.99	11.8	0.16	2.98	0.15	99.0
98-RC-09	-130.0575	45.8012	3	50.2	14.2	1.58	11.1	0.23	7.10	11.7	0.17	2.99	0.16	99.4
98-RC-16	-130.0258	45.7923	3	50.2	14.0	1.48	11.3	0.20	7.08	11.7	0.15	2.87	0.14	99.1
98-RC-17	-130.0283	45.7983	3	50.4	13.9	1.57	11.5	0.21	6.95	11.6	0.16	2.95	0.15	99.3
98-RC-40	-130.0700	45.8400	3	50.1	13.9	1.67	11.6	0.22	6.79	11.4	0.18	3.13	0.16	99.2
98-RC-43	-130.0475	45.8310	3	50.3	13.9	1.65	11.4	0.23	6.88	11.4	0.19	2.98	0.15	99.2
99-RC-102	-130.0370	46.0770	3	49.7	14.1	1.52	10.6	0.21	7.08	12.0	0.15	2.88	0.13	98.3
99-RC-105	-130.0620	45.8550	3	49.6	14.3	1.47	10.3	0.20	7.24	11.9	0.15	2.84	0.12	98.2
99-RC-106	-130.0580	45.8620	3	49.5	14.0	1.53	10.7	0.20	7.03	12.0	0.17	2.91	0.14	98.1
99-RC-107	-130.0620	45.8290	3	49.7	14.2	1.53	10.5	0.21	7.15	12.2	0.16	2.93	0.13	98.7
99-RC-108	-130.0640	45.8170	3	50.0	13.9	1.65	11.2	0.22	6.82	11.6	0.19	3.04	0.13	98.7
99-RC-54	-130.0780	45.6560	3	48.7	16.9	1.25	9.3	0.17	8.47	11.8	0.09	2.78	0.09	99.5
99-RC-55	-130.0720	45.6870	3	50.0	14.1	1.69	11.4	0.22	6.78	11.9	0.18	2.91	0.13	99.2
99-RC-57	-130.0820	45.7010	3	50.0	13.7	1.79	12.3	0.22	6.37	11.4	0.18	3.14	0.17	99.3
99-RC-59	-130.0630	45.7660	3	50.0	14.1	1.62	11.3	0.20	6.82	11.8	0.16	3.01	0.14	99.2
99-RC-61	-130.1380	45.7530	3	50.0	13.8	1.64	11.4	0.22	6.70	11.5	0.19	2.99	0.17	98.7
99-RC-62	-130.0510	45.8670	3	50.1	13.7	1.72	11.4	0.21	6.64	11.5	0.21	2.95	0.18	98.6
99-RC-64	-130.0800	45.7270	3	50.0	13.8	1.71	11.4	0.23	6.62	11.6	0.21	2.97	0.19	98.7
99-RC-65	-130.0790	45.7190	3	50.0	13.8	1.73	11.7	0.23	6.51	11.7	0.20	2.94	0.16	99.0
99-RC-66	-130.0800	45.7090	3	50.2	14.0	1.51	11.0	0.20	6.91	11.9	0.13	2.90	0.13	98.8
99-RC-67	-130.1410	45.8080	3	49.7	14.2	1.71	10.8	0.21	6.85	11.9	0.22	3.06	0.19	98.8
99-RC-72	-130.0140	45.7600	3	49.0	14.1	1.59	11.0	0.20	6.97	11.9	0.17	2.89	0.14	98.0
99-RC-74	-130.0170	45.7530	3	49.5	14.1	1.58	11.1	0.22	6.80	12.0	0.17	2.92	0.17	98.5
99-RC-75	-130.0120	45.7740	3	49.9	14.1	1.64	11.2	0.22	6.61	12.0	0.18	2.94	0.15	98.9
99-RC-82	-130.0370	45.7630	3	47.8	16.9	1.17	9.6	0.19	8.82	11.8	0.07	2.68	0.09	99.1
99-RC-83	-130.0550	45.8460	3	49.8	14.1	1.55	10.7	0.22	7.10	12.2	0.17	2.85	0.15	98.8
99-RC-86	-130.0430	45.7870	3	49.9	13.7	1.73	11.8	0.22	6.46	11.5	0.20	3.09	0.19	98.8
99-RC-87	-130.0430	45.7980	3	49.9	13.7	1.76	11.9	0.24	6.46	11.5	0.19	3.12	0.19	98.9

Table 3-1. Continued.

Sample	Longitude	Latitude	Age Class	SiO_2	Al_2O_3	TiO_2	FeO	MnO	MgO	CaO	K_2O	Na_2O	P_22O_5	Total
99-RC-88	-130.0390	45.8110	3	49.9	13.9	1.59	11.0	0.20	6.97	11.8	0.17	2.95	0.16	98.8
98-RC-08	-130.0593	45.7975	3											
98-RC-20	-130.0550	45.6717	3											
98-RC-25	-130.0463	45.8433	3											
98-RC-37	-129.9247	45.7897	3											
98-RC-38	-130.0375	45.7625	3											
99-RC-103	-130.0590	46.0800	3											
99-RC-104	-130.0690	46.0650	3											
99-RC-109	-130.1430	45.8220	3											
99-RC-110	-130.1450	45.8330	3											
99-RC-80	-130.0130	45.7670	3											
00-RC-114	-129.8576	45.9017	3											
00-RC-115	-129.8603	45.8902	3											
00-RC-121	-130.0287	46.0700	3											
01-RC139	-129.9695	45.9877	3											

spectroscopy were used in these analyses. See Appendix for a description of the analytical methods used in this study.

The intermediate (Age 2) samples are found in the areas between the age 1 and 3 samples, but they also almost completely overlap the older and younger basalts. Therefore, only the samples classified as youngest (Age 1) and oldest (Age 3) were used in the geochemical analysis. Basalts may remain very fresh and glassy for a relatively short period of time before they 'age' to the intermediate category, and they may likewise be in the Age 3 category for a relatively short time before they are buried by sediments and not retrievable by the wax corer. They may remain in the intermediate state for the majority of their exposure time on the ocean floor, which would explain the spatial prevalence of Age 2 basalts. Using only the Age 1 and 3 samples allows for two relatively discrete spatial (and therefore temporal) groups of basalts to be examined for geochemical change in Axial Segment magmas.

The interaction of the Cobb hotspot and Juan de Fuca ridge has led to mixing of the magmas produced by the two systems and the production of hybrid magmas. Axial Segment lavas are more enriched in incompatible elements closer to Axial Seamount due to a higher proportion of the Cobb hotspot magmatic endmember, and they become progressively more depleted due to a higher proportion of the MORB endmember as distance from Axial Seamount increases along the ridge. In addition, Axial Segment lavas show increasing effects of fractional crystallization with increasing distance from the hotspot, suggesting that ridge magma chambers become progressively smaller and cooler. These two processes overprint one another, leading to more primitive and enriched basalts near Axial Seamount, and more depleted and evolved basalts near the distal ends of the Axial Segment. Figure 3-4 shows that the younger basalts were sampled more heavily in areas closer to the hotspot, whereas the older basalts were more heavily collected further to the south, and these spatial gradients prevent a direct comparison between the two groups. To eliminate this bias, only those samples collected in an area of overlap between latitude 45.76° and 45.88° were used to allow for a direct geochemical comparison. The results are shown in Figure 3-6, which clearly shows the younger basalts are generally more mafic than the older samples for a given distance from the hotspot.

Major element Harker diagrams show that the younger (Age 1) basalts are, in addition to being more mafic, slightly more enriched in K_2O for a given MgO content (Figure 3-6), and the K_2O/TiO_2 ratio is clearly higher for the younger basalts as a result (Figure 3-7). Concentrations of other major elements are not significantly different between the two groups, however (Table 3-1). Incompatible trace element concentrations and ratios are also enriched in the more recent lavas (Figure 3-8). Elevated K_2O/ TiO_2, along with elevated Sr and total alkali abundances, are prominent geochemical signatures of the Cobb hotspot relative to JdFR MORB (Rhodes et al., 1990), and an increase in these

Figure 3-6. Major element variation has been minimal in the time period between "Age 1" and "Age 3" basalts, but there is a clear distinction in the range of MgO compositions in the two groups. The more mafic composition of the younger basalts may be an indication of recent magma chamber recharge. Age 1 samples were more prevalent in the north part of the South Rift Zone, and Age 3 samples were more common in the south, and latitude range shown is the area of highest overlap. The decreasing gradient in MgO with latitude is apparent in both age groups (see Chapter 2)

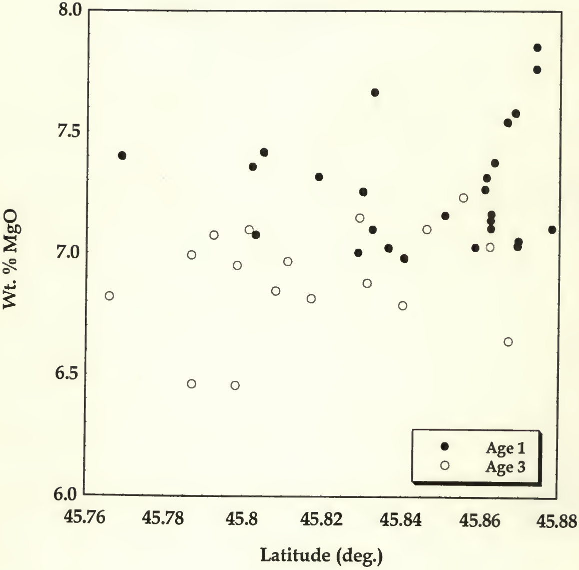
8.0
7.5
7.0
6.5
6.0
Wt. % MgO
45.76
45.78
45.8
45.82
45.84
45.86
45.88
Latitude (deg.)
● Age 1
○ Age 3

Figure 3-7. Two geochemical signatures of the Cobb hotspot are a high K_2O/TiO_2 content, and high total alkalis ($Na_2O + K_2O$) relative to the Juan de Fuca Ridge. The younger (Age 1) basalts have generally higher K_2O/TiO_2 ratios for a given MgO content, but the alkali contents of the two groups are not readily distinguishable.

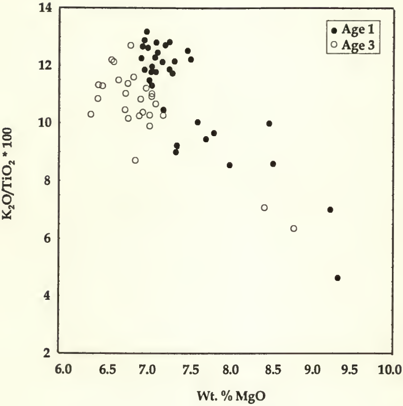
● Age 1
○ Age 3
14
12
10
8
6
4
2
K_2O/TiO_2 * 100
6.0
6.5
7.0
7.5
8.0
8.5
9.0
9.5
10.0
Wt. % MgO

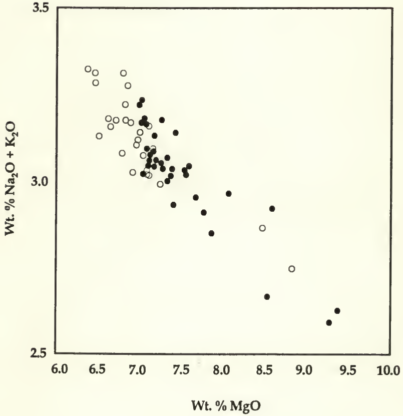
3.5
3.0
2.5
Wt. % $Na_2O + K_2O$
6.0
6.5
7.0
7.5
8.0
8.5
9.0
9.5
10.0
Wt. % MgO

Figure 3-8. Incompatible trace element ratios suggest that the younger lavas are generally more enriched, possibly reflecting an increase in the proportion of the Cobb hotspot mixing endmember.

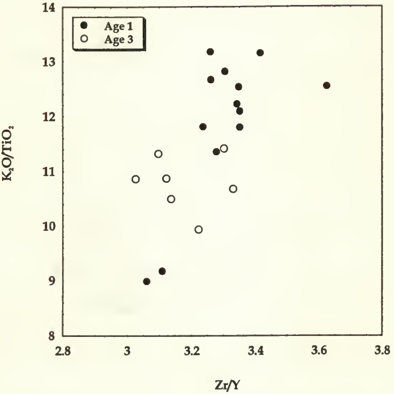
14
13
12
11
10
9
8
2.8
3
3.2
3.4
3.6
3.8
K₂O/TiO₂
Zr/Y
● Age 1
○ Age 3

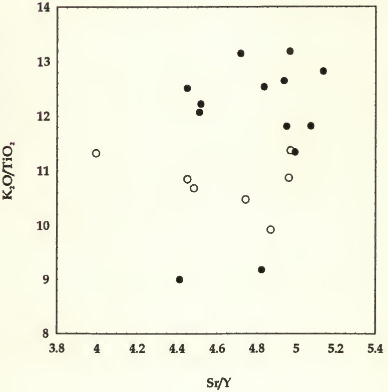
14
13
12
11
10
9
8
3.8
4
4.2
4.4
4.6
4.8
5
5.2
5.4
K₂O/TiO₂
Sr/Y

elements and ratios suggests an increase in the proportion of this endmember in recent time.

Discussion

The Axial Segment of the JdFR provides a unique opportunity to study the first few hundred thousand years of a ridge-hotspot interaction, and provides an interesting comparison with the well-studied and more prolonged interaction of the Mid-Atlantic Ridge with the Iceland plume. The Cobb hotspot has had a major influence on the magmatic and tectonic evolution of the Axial Segment. Hotspot-source magmas have entered the mid-ocean ridge magma system and oversupplied the segment, leading to anomalous shallow bathymetry, a dominance of volcanic features, and hybrid magmas. The capture of the Axial Segment has resulted in an off-center neovolcanic zone and gradients in bathymetry and basalt ages across the strike of the ridge.

The mechanism of spreading center capture may be different for the Axial Segment than for the Mid-Atlantic Ridge at Iceland, where the process takes place every few million years, and active rift zones can migrate hundreds of kilometers from the center of the hotspot before relocation back to the east occurs. At Axial, the NVZ relocations appear to have been more frequent or may occur as a constant migration or "asymmetric spreading" (Small, 1995), with the newest axis of active spreading overlapping with the most recently abandoned one, leading to the corrugated morphology of the Axial Segment. The difference may be due to the thicker crust generated by the more robust Iceland plume, 32-

40 km (Maclennan, 2001) compared with <10 km at Axial Seamount (Hooft and Detrick, 1995). If the crust over the hotspot is significantly thicker than at the active rift, this may prolong the time it takes for the NVZ crust to cool and strengthen to the point that it is stronger than the crust over the hotspot, resulting in a ridge jump.

Lavas erupted from Axial Seamount have been reported to have an unusually low geochemical variability, likely due to mixing and homogenizing effects of a large magma chamber or lens beneath the edifice (Perfit et al., 1988; Rhodes, 1988; West et al., 2001). This homogeneity does not extend into the rift zones of the Axial Segment, where variations in the proportions of Cobb hotspot and MORB magmas have been shown to be variable with distance from the hotspot and the proportions of hotspot and MORB mixing endmembers. The capture of the Axial Segment allows us to examine temporal variability of the magmatic system as well. It is not clear what age ranges are represented by the qualitative age groups in this study, but the placement of some Age 3 basalts close to the western side of the Axial Segment suggests that a significant portion of the magmas generated by the ~0.4 my ridge-hotspot interaction are represented in this study.

The young lavas from along the eastern side of the captured Axial Segment show minor but clear enrichments in incompatible trace elements, possible evidence for a recent increase in the proportion of Cobb hotspot magmas into the Axial Segment magmatic system. The generally higher MgO contents (up to 0.5 wt. %) in the more recent lavas may indicate a recent influx of primitive magma into the system.

CHAPTER 4
THE COBB HOTSPOT: A FIXED MANTLE MELTING ANOMALY WITH MORB-LIKE GEOCHEMICAL CHARACTERISTICS

Introduction

The Wilson (1963) hypothesis that mantle plumes are fixed relative to the mobile lithosphere has proven to be a generally successful model. This simple model of 'anchored' magma sources in the sub-lithospheric mantle readily explains the age-progressive distribution of hotspot volcanism, furnishes a reference frame for plate motion studies, and provides an explanation for the chemical and isotopic differences of hotspot lavas relative to shallower MORB. There are, however, important problems remaining in hotspot research that focus on developing a better understanding of the depth of origin and ultimate source of mantle plume material. The nature of these sources has important implications for constraining the depth and structure of convection and chemical diversity of the mantle.

Volcanic rocks from hotspots commonly have more radiogenic Sr and Pb, less radiogenic Nd isotopic ratios, and are more enriched in incompatible trace elements compared with basalts erupted at spreading ridges. These compositional differences suggest that magmas generated from most mantle plumes have time-integrated enrichments in incompatible trace elements, notably higher Rb/Sr and/or U/Pb ratios, and lower Sm/Nd ratios relative to the MORB source. Many of the compositional differences between ocean island basalt (OIB) and mid-ocean ridge basalt (MORB) are believed to reflect contributions from recycled oceanic crust and sediments that have been added to the deep mantle by subduction. For example, Hofman and White (1982) proposed a model in which subducted oceanic crust sinks to some density compensation level, possibly the D″ layer at the base of the mantle. Subsequent development of Rayleigh-Taylor instabilities in the material caused by internal radiogenic heating and heat transfer from the core (Elsasser et al., 1979), lead to diapiric rise of the material as mantle plumes. This interpretation was developed largely from analyses of radiogenic isotopic systems, particularly Sm-Nd, which have higher concentrations in the crust than in the mantle, and higher concentrations in OIB than in MORB (Carlson, 1998).

Evidence that some mantle plumes do not arise from the 2900 km core-mantle boundary has been growing in recent years, but the results remain controversial. High-resolution seismic tomographic imaging has revealed a 150-km-diameter plume conduit reaching depths of at least 400 km under Iceland (Wolf et al., 1997), and other seismic studies suggest lower-mantle sources for the Hawaiian and Iceland plumes (Li et al., 2000; Shen et al., 1998). Plumes are generally not resolved in global (whole mantle) tomographic models (Ekstrom and Dziewonski, 1998), possibly due to their apparent narrow diameter (<400 km).

Geochemical evidence for plume-core interaction derives from the isotopic composition of Re, Pt, and Os, which are siderophyl-calcophile elements that are expected to be concentrated in the core. Analyses of their isotopic ratios in some plume-derived volcanic rocks suggest that 0.5 to 1% core material has been added (e.g. Brandon et al., 1998; Walker, 1995). These estimates are derived from the observation that subducted oceanic crust is enriched in ^{187}Re due to its incompatiblity in the MORB mantle relative to Os. This enrichment would result in plumes with high radiogenic ^{187}Os compositions if subducted slabs are the source of plumes (Reisberg et al., 1993). Correlations of ^{187}Os with ^{186}Os in Hawaiian lavas, however, suggest high Pt/Re ratios that are not observed in crustal materials, but are consistent with the presumed core composition (Brandon et al., 1998). Alternatively, mass-balance calculations based on radiogenic Pb isotope compositions, which should have very low concentrations in the core, suggest a stronger influence from subducted oceanic crust. These data suggest the proportion of core material in some hotspots is less than 0.3% (Widom and Shirey, 1996).

The Cobb Hotspot

The Cobb-Eickelberg (C-E) seamount chain extends from the currently active Axial Seamount, the locus of the Cobb hotspot on the Juan de Fuca Ridge, to the 33 Ma Patton Seamount near the Aleutian Trench (Keller et al., 1997). The hotspot is unusual in that it exhibits the temporal and spatial characteristics of other hotspots, but not the typical isotopic or incompatible trace element characteristics (Desonie and Duncan, 1990). ^{40}Ar-^{39}Ar and K-Ar ages from volcanoes in the C-E chain show a clear positive correlation of age and distance from Axial Seamount to the northwest, consistent with plate motion vectors for the north Pacific and a fixed plume origin for the chain (Karsten and Delaney, 1989).

C-E basalts have a modest enrichment in some trace elements, particularly LREE (La_N/Yb_N up to 1.9), Sr (up to 328 ppm), and K_2O/TiO_2 (up to 0.24), distinguishing them from most N-MORB erupted from the nearby Juan de Fuca Ridge (see Chapter 2). These compositions fall within global MORB ranges, however. C-E basalts have Sr, Nd, and Pb isotopic ratios that are within MORB ranges as well (Figure 4-1; Desonie and Duncan, 1990). Axial Seamount lavas have MORB-like ^{3}He/^{4}He (7.9 to 8.4 R_A; Lupton et al., 1993) and volatile contents (< 0.25 wt.% H_2O, < 300 ppm Cl; unpublished data from this study), although these basalts are dominated by the JdFR MORB source and are calculated to contain a maximum of 40% of the Cobb plume component (see Chapter 2).

Discussion

Schilling (1973) and Hart et al. (1973) established geochemical support for the fixed mantle plume hypothesis based on the anomalous composition and geochemical gradients in basalts along the Mid-Atlantic Ridge proximal to Iceland. Subsequent studies (e.g., Zindler and Hart, 1986; Hart, 1988) have established a set of mantle end-members for hotspots, including EMI and EMII, which reflect mixing with continental material, and HIMU (which results from a

Figure 4-1. $^{143}Nd/^{144}Nd$ vs. $^{87}Sr/^{86}Sr$ variation diagram showing the similarity of the Cobb hotspot basalts to MORB in general and to Juan de Fuca Ridge MORB in particular. The radiogenic isotopic characteristics of Iceland, Hawaii, and the Galapagos, three hotspots with relatively low Sr and high Nd isotopic ratios, are shown for comparison. Like Cobb, the isotopic composition of Iceland basalts also falls within the global MORB field.

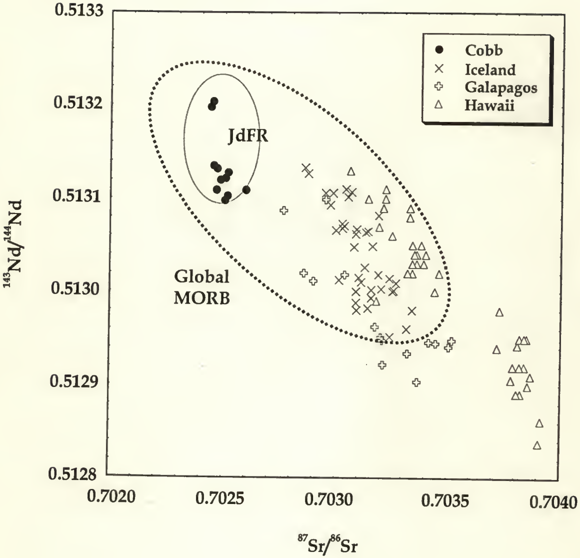
0.5133
0.5132
0.5131
0.5130
0.5129
0.5128
^{143}Nd/^{144}Nd
0.7020
0.7025
0.7030
0.7035
0.7040
^{87}Sr/^{86}Sr
● Cobb
× Iceland
✣ Galapagos
△ Hawaii
JdFR
Global MORB

time-integrated enrichment in U/Pb). The fourth end-member in the hotspot tetrahedron is Depleted MORB Mantle (DM), which is thought to represent the shallow MORB source that potentially mixes with the other components (Zindler and Hart, 1986). In those cases where plume-derived lavas do not show strong EM or HIMU signatures, recognition of plume activity must be dependent on physical manifestations (e.g., seamount chains). In the case of the C-E Seamounts, a model involving a fixed, deep mantle plume source with the geochemical characteristics of MORB presents a significant paradox in light of the hotspot geochemical paradigm.

Desonie and Duncan (1990) concluded that the major and trace element characteristics of the Cobb hotspot lavas are best explained by mixing of deep and upper mantle materials. They suggested a model of entrainment of MORB-source upper mantle by a thermally (as opposed to compositionally) buoyant plume of lower mantle composition, driven by viscosity and density differences created by its high temperature. The complete absence of the typical isotopic geochemical signature of this lower mantle plume, however, suggests that this is not the case. In addition, the MORB-like isotopic compositions of all seamounts in the northeastern Pacific may indicate differences in the composition of the deep mantle on a regional scale. Hart (1988) termed the regional isotopic homogeneity of the area the 'anti-Dupal anomaly', noting a general north-poleward trend toward more MORB-like hotspot compositions. Basalts from Iceland, for example, are confined to the global MORB field in Sr and Nd isotopic space in much the same way as the Cobb hotspot basalts, albeit with higher $^{87}Sr/^{86}Sr$ and lower $^{143}Nd/^{144}Nd$ (Figure 4-1).

Model Age of the Cobb Hotspot

Evidence for a role of subducted slabs in the generation of hotspots may be found in modeled time scales for the subduction-plume cycle, (e.g., 'model ages'). The basis of model ages such as these is the assumption that the composition of the source region from which magmas were originally derived is known or can be modeled (DePaolo, 1981). In the case of ridges and hotspots, the isotopic composition is extrapolated back in time using observed Sm/Nd ratios until it intersects the depleted mantle (DM) evolution line. At this point in time, the calculated age (model age) represents the time at which the sample had the same $^{143}Nd/^{144}Nd$ ratio as DM, but separated and acquired a different Sm/Nd ratio. Traditional DM model ages (T_{DM}) are calculated using:

$$T_{DM} = 1/\lambda \ \ln \ \frac{(^{143}Nd/^{144}Nd)_{sample,\ today} - (^{143}Nd/^{144}Nd)_{DM,\ today}}{(^{147}Sm/^{144}Nd)_{sample,\ today} - (^{147}Sm/^{144}Nd)_{DM,\ today}} +1$$

where λ is the decay constant for ^{147}Sm to ^{144}Nd (6.54×10^{-12}).

In light of the depleted nature of the Cobb plume, traditional model ages do not yield a useful data set. Alternatively, setting the values of DM to be the equivalent of the average JdFR MORB ($^{143}Nd/^{144}Nd = 0.513171$; $^{147}Sm/^{144}Nd = 0.21$) allows a more direct evaluation of the plume compared to both local asthenospheric sources and the global array of plume compositions. The results using these criteria are shown in Table 4-1, and show 'ages' between about 62 and 323 Ma. These results are likely biased to higher values, however, caused by the trace element enrichments in the Cobb lavas relative to the JdFR, particularly Sm/Nd, which is consistently lower in lavas than their source rocks (Figure 4-2). Decreases in the Sm/Nd ratio resulting from LREE enrichment lead to older calculated model ages. The MORB-like Sr, Nd, and Pb isotopic ratios of the Cobb hotspot indicate that the source of the plume must have had MORB-like depletions in incompatible elements over most of its history, and the current trace element enrichments indicate a decoupling of trace elements and radiogenic isotopes, and are likely to be the result of a recent metasomatic event.

The model ages calculated here ostensibly show the time elapsed since the separation of the sources of the Cobb plume and the JdFR MORB sources. The young ages suggest that the plume source does not reflect a contribution from oceanic crust that has undergone a cycle of subduction, heating at the core mantle-boundary, and diapiric rise through the entire mantle. Instead, in light of the MORB-like isotopic character, the Cobb hotspot source appears to reflect asthenospheric material that lies below the mobile mantle. This material may have been attached to a subducting slab and transported to a neutrally buoyant position where it detached from the sinking eclogitic slab at some time in the relatively recent past.

Table 4-1. Model ages calculated for the Cobb-Eickelberg Seamounts.

Sample	Sm[1]	Nd[1]	Sm/Nd	$^{147}Sm/^{144}Nd$	$^{143}Nd/^{144}Nd$	Model Age	$^{87}Sr/^{86}Sr$	$(La/Yb)_N$	K2O/TiO2
DH1-1	4.39	15.58	0.28	0.17	0.513109	2.38E+08	0.702467	1.83	16.40
DH2A	5.50	17.78	0.31	0.18	0.513122	3.23E+08	0.702507	1.32	24.57
DH2-8	4.17	19.00	0.22	0.13	0.513128	8.48E+07	0.702518	1.46	27.87
DH4-4	4.06	13.73	0.30	0.18	0.513109	3.02E+08	0.702596	1.52	24.43
DH5-14	4.68	15.83	0.30	0.18	0.51312	2.48E+08	0.702485	1.38	16.99
DH8-8	4.18	14.92	0.28	0.17	0.513103	2.55E+08	0.702515	1.85	23.53
DH10-7	5.48	19.40	0.28	0.17	0.51309	2.83E+08	0.702505	1.85	13.66
CB-1	4.41	22.00	0.20	0.12	0.51313	6.19E+07	0.702454	1.71	12.97

[1] Sm and Nd in parts per million (ppm)

Figure 4-2. Although they have MORB-like radiogenic isotopic compositions, Cobb hotspot basalts have clear trace element enrichments relative to the Juan de Fuca Ridge (JdFR), similar to Hawaii, Iceland and the Galapagos. This decoupling of trace elements and isotopic ratios suggests a recent metasomatic event enriched the hotspot source.

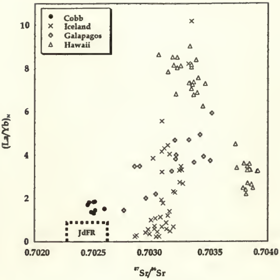
● Cobb
× Iceland
◇ Galapagos
△ Hawaii
JdFR
$(La/Yb)_N$
0
2
4
6
8
10
0.7020
0.7025
0.7030
0.7035
0.7040
$^{87}Sr/^{86}Sr$

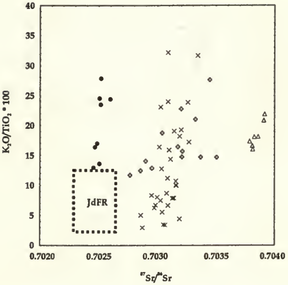
JdFR
$K_2O/TiO_2 * 100$
0
5
10
15
20
25
30
35
40
0.7020
0.7025
0.7030
0.7035
0.7040
$^{87}Sr/^{86}Sr$

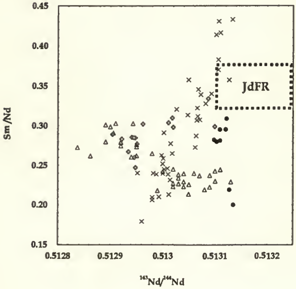
JdFR
Sm /Nd
0.15
0.20
0.25
0.30
0.35
0.40
0.45
0.5128
0.5129
0.513
0.5131
0.5132
$^{143}Nd/^{144}Nd$

CHAPTER 5
SUMMARY AND CONCLUSIONS

Magmatic Consequences of the Ridge-Hotspot Interaction

The shallow bathymetry and prevalence of volcanic features on the Axial Segment are indications that magmas from the Cobb hotspot have not only created the Axial Seamount volcanic edifice, but have also oversupplied the ridge segment and migrate laterally along it. To validate this hypothesis and to understand the relative proportions of hotspot and Axial Segment MORB magmas erupted along the ridge, major element, trace element, and isotopic analyses of basalts from the Axial Segment were conducted. The analyses have revealed that the relatively homogeneous basalts erupted from Axial Seamount are modestly incompatible-element enriched, albeit MORB-like, with chemical characteristics that can be related to the Cobb plume source (notably high total alkalis, K_2O/TiO_2, Sr and LREE). The basalts from the Axial Segment as a whole have incompatible trace element and isotopic compositions that are generally intermediate between basalts from the Cobb-Eickelberg seamount chain and the more depleted basalts from the other segments of the Juan de Fuca Ridge. Variable mixing of the two magma types and fractional crystallization of the hybrid magmas are required to explain the geochemical variation along the Axial Segment.

Basalts from the Axial Segment "rift zones" are more heterogeneous because of the prevalence of more mafic and depleted basalts with a high proportion the indigenous Axial Segment MORB component, and gradients in the lava compositions along the length of the Axial Segment. These gradients reveal that the magmas are progressively more evolved and the proportion of the MORB mixing component progressively increases with distance from the hotspot. The absence of the distinctive volcanic ridge morphology, shallow bathymetry, and trace element enrichments on the neighboring Vance and CoAxial Segments suggests the influence of the Cobb hotspot on the Juan de Fuca Ridge is confined to the Axial Segment.

Specifically, the results of this study suggest:

(1) Most basalts from the Axial Segment have generally higher K_2O+Na_2O, Sr, Nb, Sc and LREE, and lower FeO, TiO_2 and Y relative to basalts from the neighboring JdFR segments, although they are within MORB geochemical ranges. These are the same relative enrichments and depletions exhibited by the Cobb hotspot (except for Sc which has likely been depleted by cpx fractionation in the more evolved C-E lavas). These data support the hypothesis of lateral migration of hotspot magmas along the Axial Segment rift zones.

(2) Analyses of basalts collected in this extensive sampling campaign have revealed geochemical gradients in major and trace elements along the Axial Segment. The apices of these gradients are on or near Axial Seamount, and they

are inversely correlated, with progressively more fractionated and incompatible element depleted lavas erupted with greater distance from the Cobb hotspot. This relationship implies that in addition to fractional crystallization, mixing is also an important petrologic process on the Axial Segment.

(3) Some basalts recovered on the Axial Segment have distinct, depleted compositions (Generally higher MgO, lower Sr, MORB-like REE patterns) and presumably represent lavas with a high proportion of the local Axial Segment MORB source and mixing end-member. These lavas avoided the homogenization and thorough mixing with Cobb hotspot magmas and homogenization observed in most of the Axial seamount suite.

(4) Models of mixing relations suggest that the basalts sampled along the Axial Segment are the result of heterogeneous mixing between Cobb hotspot magmas and the presumed indigenous MORB component. The basalts are dominated by the MORB end-member, and the most enriched lavas contain only about 40% of the hotspot component. The dominance of the MORB component explains why none of the basalts from the Axial Segment are as enriched as samples from the C-E chain. Mixing of the two end-members and fractional crystallization of the hybrid magmas can explain the range of major element abundances, trace element ratios, and radiogenic isotopic ratios observed on the Axial Segment.

Capture of the Axial Segment by the Cobb Hotspot

The interaction between the Juan de Fuca Ridge and the Cobb hotspot began circa 0.4 Ma ago, when a ~60-km-long section of the northwesterly-migrating ridge was abandoned and spreading was initiated over the hotspot, creating the Axial Segment. The off-center locations of the Axial Seamount caldera and recent eruptions on the ridge, the age characteristics of basalts, and asymmetry of the bathymetric profile of the Axial Segment suggest that its neo-volcanic zone has been "captured" by the hotspot since the relocation, in spite of the continued migration of the rest of the plate boundary.

Ridge capture and the resulting process of rift zone abandonment have exposed a progression of older lavas to the west of the neo-volcanic zone, and the basalt sampling campaign and geochemical analyses undertaken in this study have revealed minor geochemical differences between younger and older lavas. The younger basalts recovered from the neo-volcanic zone on the eastern side of the Axial Segment are generally more mafic and more enriched in K_2O and Sr than the older basalts from the western side, an indication of recent minor changes in the composition and/or increase in the proportion of the Cobb hotspot mixing end-member relative to the MORB end-member supplying the Axial Segment. The higher MgO content of the younger lavas may also indicate a recent influx of more primitive magma into the Axial Seamount magmatic system.

The MORB-like Cobb Hotspot

Volcanic rocks from hotspots typically have more radiogenic Sr and Pb, less radiogenic Nd isotopic ratios, and are more enriched in incompatible trace elements compared with mid-ocean ridge basalts. The Cobb hotspot is unusual in that it exhibits the temporal and spatial characteristics of other hotspots, but not the typical geochemical characteristics. Cobb-Eickelberg Seamount basalts have a modest enrichment in some trace elements, particularly LREE (La_N/Yb_N up to 1.9), Sr (up to 328 ppm), and K_2O/TiO_2 (up to 0.24), distinguishing them from most N-MORB erupted from the nearby Juan de Fuca Ridge (see Chapter 2). These compositions fall within global MORB ranges, however, and basalts from the Cobb hotspot have MORB-like Sr, Nd, Pb, and He isotopic ratios as well. A mantle plume that has remained in a fixed location for at least 33 Ma with MORB geochemical characteristics presents a significant challenge to generally accepted models for deep mantle compositions and the origins of mantle plumes.

Model ages calculated in this study suggest that between about 62 and 323 Ma has elapsed since the "separation" of the sources of the Cobb plume and the JdFR MORB sources. The young ages suggest that the plume source does not reflect a contribution from oceanic crust that has undergone a cycle of subduction, heating at the core mantle-boundary, and diapiric rise through the entire mantle. Instead, the Cobb hotspot source appears to reflect asthenospheric material that lies below the mobile mantle.

APPENDIX
ANALYTICAL METHODS

Major element and some trace element analyses (SiO_2, Al_2O_3, TiO_2, FeO, MnO, MgO, CaO, K_2O, Na_2O, P_2O_5) of glasses were performed by electron microprobe at the U.S. Geological Survey in Denver, Colorado and at Florida International University in Miami, Florida. Glass chips (100-500 mg) were selected by hand under a microscope to choose those that were most free of alteration, and these were ensonicated for three minutes in a dilute hydrochloric acid and hydrogen peroxide solution. The microprobes typically analyzed a line of 10 μm target spots on the glass chips. Major element values in this paper are beta- and standard-corrected (standards JDF and 2392-9) averages of 6-10 spots on each sample, and rare spurious compositions caused by phenocrysts were excluded.

Trace element and some major element analyses (Ba, Ce, Co, Cr, Cu, Fe_20_3, Ga, K_20, La, Nb, Ni, Rb, Sc, Sr, TiO_2, V, Y, Zn, Zr) were performed on 30-mm-diameter pressed powder pellets on the X-ray fluorescence (XRF) spectrometer at the Department of Geological Sciences at the University of Florida. Glass for the pellets was coarsely crushed in a jaw crusher or cross-beater mill, ensonicated in dilute hydrochloric acid and hydrogen peroxide solution, and powdered in an agate ball mill for three 12-minute intervals to a fine powder. Powders were mixed with methylene chloride binder solution (0.5 ml/gram of sample) and pressed for five minutes at 30,000 psi. Spectrometer matrix effects were corrected by monitoring the Rh Compton peak, and instrumental drift, accuracy, and precision were monitored using basalt standards (internal standard ENDV-10, and BHVO) with each spectrometer run of five to fifteen samples.

Selected samples were analyzed for major and trace element composition, including rare earths, using Inductively-Coupled Plasma Mass Spectrometry (ICP-MS) at the Geological Survey of Canada and Boston University. The sample is sprayed as a fine aerosol into a 7000 K argon plasma, and the ions are separated according to their mass using a quadruple analyzer.

Radiogenic isotopic data was collected using the Thermal Ionization Mass Spectrometer (TIMS) facility at the Department of Geological Sciences at the University of Florida. For Sr ($^{87}Sr/^{86}Sr$), sample powders were crushed and cleaned as above for XRF analysis, and 50 to 100 mg powder samples were dissolved in once-distilled trace metal hydrofluoric acid with 1-2 drops of HNO_3 solution, then heated for two days at 100° C and dried on a hotplate. The precipitate was then converted to chloride salts by dissolving in 2 ml of 6N trace metal grade hydrochloric acid and then re-drying. These were dissolved again in HCl and centrifuged to remove any solid material. Sr and rare earth element cuts were then eluted using calibrated quartz glass columns packed with cation exchange resin (200/400 mesh sieve). Samples were then re-dried in preparation for filament loading and analysis on the mass spectrometer.

Radiogenic Pb isotopes ($^{208}Pb/^{204}pb$, $^{207}Pb/^{204}Pb$, $^{206}Pb/^{204}Pb$) required a two column process, using 500 µl and 200 µl columns with 100-200 mesh Dowex 1X-8 resin, and ultra-clean acids dopt for Pb isotopes. The columns are first cleaned with 6N HCl, and then equilibrated with 1N HBr. Samples are then converted to bromides by dissolving in 1N HBr, and solid material is collected by centrifuge. The samples are then passed through the columns, collected and dried after both column passes.

REFERENCES

Appelgate, T.B., Jr., Volcanic and structural morphology of the south flank of Axial Volcano, Juan de Fuca Ridge: Results from a SeaMARC I side scan survey, *J. Geophys. Res., 95,* 12765-12783, 1990.

Batiza, R., and D. Vanko, Volcanic development of small oceanic central volcanoes on the flanks of the East Pacific Rise inferred from narrow-beam echo-sounder surveys, *Mar. Geology, 54,* 53-90, 1983.

Batiza, R., and D. Vanko, Petrology of young Pacific seamounts, *J. Geophys. Res., 89,* 11235-11260, 1984.

Buck, W.R., Accretional curvature of lithosphere at magmatic spreading centers and the flexural support of axial highs, *J. Geophys. Res, 106,* 3953-3960, 2001.

Campbell, I.H., and R.W. Griffiths, Implications of mantle plumes for the evolution of flood basalts, *Earth Planet. Sci. Lett.,* 99, 79-93, 1990.

Carlson, R.W., A conduit to the core, *Nature, 394,* 11-12, 1998.

Cochran, J.R., and W. R. Buck, Near-axis subsidence rates, hydrothermal circulation, and thermal structure of mid-ocean ridge crests, *J. Geophys. Res., 106,* 19233-19258, 2001.

Delaney, J. R., H.P. Johnson, and J.L. Karsten, The Juan de Fuca Ridge-hotspot-propagating rift system: New tectonic, geochemical, and magnetic data, *J. Geophys. Res., 86,* 11747-11750, 1981.

Delaney, J.R., J.L. Karsten, and S.R. Hammond, Petrology and tectonics of the Juan de Fuca Ridge, *Eos Trans. AGU, 67,* 360, 1986.

DePaolo, D.J., Neodymium isotopes in the Colorado Front Range and crust-mantle evolution in the Proterozoic, *Nature, 291,* 193-196, 1981.

Desonie, D. L., and R.A. Duncan, Spreading ridge and hotspot contributions to seamounts near the Juan de Fuca Ridge, *Eos Trans. AGU, 67,* 1231, 1986.

Desonie, D. L., and R.A. Duncan, The Cobb-Eickelberg seamount chain: Hotspot volcanism with mid-ocean ridge basalt affinity, *J. Geophys. Res., 95*, p. 12697-12711, 1990.

Dziak, R.P., and C.G. Fox, Hydroacoustic detection of submarine volcanic activity at Axial Volcano, Juan de Fuca Ridge, *Eos Trans. AGU, 79*, F922, 1998.

Dziak, R.P., and C.G. Fox, The January, 1998 earthquake swarm at Axial Volcano, Juan de Fuca Ridge: Hydroacoustic evidence for seafloor volcanic activity, *Geophys. Res. Lett.*, 26, 3425-3428, 1999.

Eaby, J., D.A. Clague, and J.R. Delaney, Sr isotopic variations along the Juan de Fuca Ridge, *J. Geophys. Res., 89*, 7883-7890, 1984.

Eberle, M.A., and Forsyth, D.W., An alternative dynamic model of the axial high at fast-spreading ridges, *J. Geophys. Res., 103*, 12309-12320, 1998.

Elliot, T., C.J. Hawkesworth, and K. Gronvold, Dynamic melting of the Iceland plume, *Nature, 351*, 201-206, 1991.

Elsasser, W.M., P. Olson, and B.D. Marsh, The depth of mantle convection, *J. Geophys. Res., 84*, 147-155, 1979.

Embley, R.W., and W.W. Chadwick, Jr., Volcanic and hydrothermal processes associated with a recent phase of seafloor spreading at the northern Cleft segment: Juan de Fuca Ridge, *J. Geophys. Res., 99*, 4741-4760, 1994.

Embley, R.W., W.W. Chadwick, D.A. Clague, and D. Stakes, 1998 eruption of Axial Volcano; Multibeam anomalies and seafloor observations, *Geophys. Res. Lett., 26*, 3425-3428, 1999.

Embley, R.W., W.W. Chadwick, M.R. Perfit, M.C. Smith, and J.R. Delaney, Recent eruptions on the CoAxial segment of the Juan de Fuca Ridge: Implications for mid-ocean ridge accretion processes, *J. Geophys. Res., 105*, 16501-16525, 2000.

Embley, R.W., K.M. Murphy, and C.G. Fox, High-resolution studies of the summit of Axial Volcano, *J. Geophys. Res., 95*, 12785-12812, 1990.

Fornari, D.J., A. Malahoff, and B.C. Heezen, Volcanic structure of the crest of the Puna Ridge, Hawaii: Geophysical implications of submarine volcanic terrain, *Geol. Soc. Am. Bull., 89*, 605-616, 1978.

Grove, T.L., R.J. Kinzler, and W.B. Bryan, Fractionation of mid-ocean ridge basalt (MORB), Mantle Flow and Melt Generation, Geophysical Monograph 71, American Geophysical Union, 281-310, 1992.

Hammond, S.R., Relationships between lava types, seafloor morphology, and the occurrence of hydrothermal venting in the ASHES vent field of Axial Volcano, *J.Geophys. Res., 95,* 12875-12893, 1990.

Hammond, S.R., and J.R. Delaney, Evolution of Axial Volcano, Juan de Fuca Ridge, *Eos Trans. AGU, 66,* 925-926, 1985.

Hardarson, B.S., J.G. Fitton, R.M. Ellam, and M.S. Pringle, Rift relocation: A geochemical and geochronological investigation of a paleo-rift in northwest Iceland, *Earth Planet. Sci. Lett., 153,* 181-196, 1997.

Hart, S.R., Heterogenous mantle domains: Signatures, genesis, and mixing chronologies, *Earth Planet. Sci. Lett., 90,* 273-296, 1988.

Hart, S.R., E.H. Hauri, L.A. Oschmann, and J.A. Whitehead, Mantle plumes and entrainment: isotopic evidence, *Science, 256,* 517-520, 1992.

Hart, S.R., J.G. Schilling, and J.L. Powell, Basalts from Iceland and along the Reykjanes Ridge: Sr isotope geochemistry, *Nature Phys. Sci., 246,* 104-107, 1973.

Hegner, E., and M. Tatsumato, Pb, Sr, and Nd isotopes in basalts and sulfides from the Juan de Fuca Ridge, *J. Geophys. Res.,* 92, B11, 11380-11386, 1987.

Hey, R., and P.R. Vogt, Spreading center jumps and sub-axial asthenosphere flow near Galapagos hotspot, *Tectonophysics, 37,* 41-52, 1977.

Hey, R.N., and D.S. Wilson, Propogating rift explanation for the tectonic evolution of the northeast Pacific-the pseudomovie, *Earth Planet. Sci. Lett., 58,* 167-188, 1982.

Hofmann, A.W., and W.M. White, Mantle plumes from ancient oceanic crust, *Earth Planet. Sci. Lett., 57,* 421-436, 1982.

Hooft, E. E., and R.S. Detrick, Relationship between axial morphology, crustal thickness, and mantle temperature along the Juan de Fuca and Gorda Ridges, *J. Geophys. Res., 100,* 22499-22508, 1995.

Hyndman, R.D., R.P. Riddihough, and R. Herzer, The Nootka fault zone-a new plate boundary off western Canada, *Geophys. J. R. Astr. Soc., 58,* 667-683, 1979.

Johnson, H. P., and R.W. Embley, Axial Seamount: An active ridge axis volcano on the central Juan de Fuca Ridge, *J. Geophys. Res.*, 12689-12696, 1990.

Johnson, H.P., and M.L. Holmes, Evolution in plate tectonics; The Juan de Fuca Ridge, The Geology of North America, in *The Eastern Pacific Ocean and Hawaii*, vol. N, Geological Society of America, edited by E.L. Winterer et al., pp. 73-91, Boulder, Colorado, 1989.

Kappel, E.S., and W.B.F. Ryan, Volcanic episodicity and a non-steady state rift valley along northeast Pacific spreading centers: Evidence from SeaMARC I, *J. Geophys. Res., 91*, 13925-13940, 1986.

Karsten, J.L., and J.R. Delaney, Hot spot-ridge crest convergence in the northeast Pacific, *J. Geophys. Res., 94*, 700-712, 1989.

Karsten, J.L., J.R. Delaney, J.M. Rhodes, and R.A. Liias, Spatial and Temporal evolution of magmatic systems beneath the Endeavor Segment, Juan de Fuca Ridge: tectonic and petrologic constrains, *J. Geophys. Res., 95*, 19235-19256, 1990.

Karsten, J.L., S.R. Hammond, E.E. Davis, and R.G. Currie, Detailed geomorphology and neotectonics of the Endeavor Segment, Juan de Fuca Ridge: new results from Seabeam swath mapping, *Geol Soc. Am. Bull.*, 97, 213-221, 1986.

Keller, R.A., M.R. Fisk, R.A. Duncan, and W.M. White, 16 M.Y. of hotspot and nonhotspot volcanism on the Patton-Murray Seamount platform, Gulf of Alaska, *Geology, 25*, 511-514, 1997.

Kushiro, I., Composition of magma formed by partial zone melting of the Earth's upper mantle, *J. Geophys. Res., 73*, 619-634, 1968.

Langmuir, C.H., and J.F. Bender, The geochemistry of oceanic basalts in the vicinity of transform faults: observations and implications, *Earth Planet. Sci. Lett., 69*, 107-127, 1984.

Langmuir, C.H., R.D. Vocke, G.N. Hanson, and S.R. Hart, A general mixing equation with applications to Icelandic basalts, *Earth Planet. Sci. Lett., 37*, 380-392, 1978.

Leary, T.J., D.F. Naar, C. Knapp, E. Sielecki, D. Seidler, S. Weinberger, T.C. Roberge, and J. Neuhuas, Video of microplates and triple junctions in freezing wax, *Eos Trans. AGU, 72*, 509, 1991.

Lonsdale, P., Non-transform offsets of the Pacific-Cocos plate boundary and their traces on the rise flanks, *Geol. Soc. Am. Bull., 96*, 313-327, 1985.

Lupton, J.E., D.W. Graham, J.R. Delaney, and H.P. Johnson, Helium isotope variations in Juan de Fuca Ridge basalts, *Geophys. Res. Lett., 20*, 1851-1854, 1993.

Macdonald, K.C., Tectonic and magmatic processes on the East Pacific Rise, The Geology of North America, in *The Eastern Pacific Ocean and Hawaii*, vol. N, Geological Society of America, edited by E.L. Winterer, pp. 93-110, Boulder, Colorado, 1989.

Maclennan, J., D.M. McKenzie, K. Gronvold, and L. Slater, Crustal accretion under northern Iceland, *Earth and Planet. Sci. Lett., 191*, 295-310, 2001.

Madsen, J.A., D.W. Forsyth, and R.S. Detrick, A new isostatic model for the East Pacific Rise crest, *J. Geophys. Res., 89*, 9997-10016, 1984.

Malahoff, A., R. Embley, S. Hammond, W. Ryan, and K. Crane, Juan de Fuca and Gorda Ridge axial morphology and tectonics from combined seabeam and SeaMARC data, *Eos Trans. AGU, 63*, 1147, 1982.

Marzocchi, W., and F. Mulargia, Patterns of hot spot volcanism, *J. Geophys. Res., 98*, 14029-14039, 1993.

Oskarsson, N., S. Steinthorsson, and G.E. Sigvaldason, Iceland geochemical anomaly: Origin, volcanotectonics, chemical fractionation and isotope evolution of the crust, *J. Geophys. Res., 90*, 10011-10025, 1985.

Perfit, M.R., A.L. Heatherington, S. Hughes, I.R. Jonasson, and J.M. Franklin, Geochemistry of basalts from Axial Volcano: An example of a well-mixed magma chamber, *Eos Trans. AGU, 69*, 1467, 1988.

Perfit, M.R., and W.W. Chadwick, Jr., Magmatism at mid-ocean ridges: Constraints from volcanological and geochemical investigations, in *Faulting and Magmatism at Mid-Ocean Ridges*, pp. 59-115, American Geophysical Union, 1998.

Phipps Morgan, J., and Y.J. Chen, Dependence of ridge-axis morphology on magma supply and spreading rate, *Nature, 364,* 706-708, 1993.

Presnall, D.C., and J.D. Hoover, High pressure phase equilibria constraints on the origin of mid-ocean ridge basalts, Magmatic Processes: Physiochemical Principles, edited by B.O. Mysen, *Spec. Publ. Geochem. Soc., 1,* 75-89, 1987.

Raff, A.D., and R.G. Mason, Magnetic survey off the west coast of North America, 40 N latitude to 50 N latitude, *Geol. Soc. Am. Bull.,* 72, 1267-1270, 1961.

Reisberg, L., A. Zindler, F. Marcantonio, W. White, D. Wyman, and B. Weaver, Os isotope systematics in ocean island basalts, *Earth Planet. Sci. Lett., 120,* 149-167, 1993.

Rhodes, J.M., Geochemistry of the 1984 Mauna Loa eruption: Implications for magma storage and supply, *J. Geophys. Res., 93,* 4453-4466, 1988.

Rhodes, J.M., C. Morgan, and R.A. Liias, Geochemistry of Axial Seamount lavas: Magmatic relationship between the Cobb Hotspot and the Juan de Fuca Ridge, *J. Geophys. Res., 95,* 12713-12733, 1990.

Riddihough, R., Recent movements of the Juan de Fuca plate system, *J. Geophys. Res., 89,* 6980-6994, 1984.

Saemundsson, K, Evolution of the axial rifting zone in northern Iceland and the Tjornes fracture zone, *Geol. Soc. Am. Bull., 85,* 495-504, 1974.

Searle, R.C., and A.S. Laughton, Fine-scale sonar study of tectonics and volcanism on the Reykjanes Ridge, report, pp. 5-13, Inst. Of Oceanogr. Sci., Leads, UK, 1981.

Schilling, J.G., Iceland mantle plume: Geochemical evidence along Reykjanes Ridge, *Nature, 242,* 565-571, 1973.

Schilling, J.G., M. Zajac, and R. Evans, Petrologic and geochemical variations along the Mid-Atlantic Ridge from 29°N to 73°N, *Am. J. Sci., 283,* 510-586, 1983.

Shen, Y., S.C. Solomon, I. Th. Bjarnason, and C.J. Wolfe, Seismic evidence for a lower-mantle origin of the Iceland plume, *Nature, 395,* 62-64, 1998.

Small, C., Observations of ridge-hotspot interactions in the Southern Ocean, *J. Geophys., Res., 100,* 17931-17946, 1995.

Smith, M.C., Geochemistry of Eastern Pacific MORB: Implications for MORB petrogenesis and the nature of crustal accretion within the neovolcanic zone of two recently active ridge segments, PhD thesis, 164 pp., Univ. of Florida, Gainesville, 1999.

Smith M.C., M.R. Perfit, and I.R. Jonasson, Petrology and geochemistry of basalts from the southern Juan de Fuca Ridge: Controls on the spatial and temporal evolution of mid-ocean ridge basalt, *J. Geophys. Res., 99,* 4787-4812, 1994.

Smoot, N.C., Observations of Gulf of Alaska seamount chains by multibeam sonar, *Tectonophysics, 115,* 235-246, 1985.

Tivey, M.A., Fine-scale magnetic anomaly field over the southern Juan de Fuca Ridge: Axial magnetization low and implications for crustal structure, *J. Geophys. Res., 99,* 4833-4855, 1994.

Tivey, M.A., and H.P. Johnson, The magnetic structure of Axial Seamount, Juan de Fuca Ridge, *J. Geophys. Res., 95,* 12735-12750, 1990.

Van Wagoner, N.A., and M.I. Leybourne, Evidence for mixing and a heterogenous mantle on the West Valley Segment of the Juan de Fuca Ridge, *J.Geophys. Res., 96,* 16295-16318, 1991.

Vine, J.F., and D.H. Matthews, Magnetic anomalies over ocean ridges, *Nature, 199,* 947-949, 1963.

Vine, F.J., and J.T. Wilson, Magnetic anomalies over a young oceanic ridge off Vancouver Island, *Science, 150,* 485-489, 1965.

Vogt, P.R., and L. Johnson, Transform faults and longitudinal flow below the mid-ocean ridge, *J. Geophys. Res., 80,* 1399-1428, 1975.

Walker, R.J., J.W. Morgan, and M.F. Horan, Osmium-187 enrichment in some plumes: evidence for core-mantle interaction? *Science, 269,* 819-822, 1995.

Ward, P.L., New interpretation of the geology of Iceland, *Geol. Soc. Am. Bull., 82,* 2991-3012, 1971.

Weaver, J.S., and C.H. Langmuir, Calculations of phase equilibrium in mineral-melt systems, *Computers and geosciences, 16,* 1-19, 1990.

Weinstein, S.A., and P.L. Olson, The proximity of hotspots to convergent and divergent plate boundaries, *Geophys. Res. Lett., 5,* 433-436, 1989.

West, M., W. Menke, M. Tolstoy, S. Webb, and R. Sohn, Magma storage beneath Axial volcano on the Juan de Fuca mid-ocean ridge, *Nature, 25,* 833-837, 2001.

Widom, E. and S.B. Shirey, *Earth Planet. Sci. Lett.,* 142, 451-465, 1996.

Wilson, D.S., Focused upwelling beneath mid-ocean ridges: Evidence from seamount formation and isostatic compensation of topography, *Earth Planet. Sci. Lett., 113,* 41-55, 1992.

Wilson, D.S., Confidence intervals for motion and deformation of the Juan de Fuca plate, *J. Geophys. Res., 98,* 16,053-16,071, 1993.

Wilson, D.S., and R.N. Hey, Propogation as a mechanism of reorientation of the Juan de Fuca Ridge, *J. Geophys. Res., 89,* 9215-9225, 1984.

Wilson, J.T., A possible origin of the Hawaiian Islands, *Can. J. Phys., 41,* 863-870, 1963.

Wolf, C.J., I. Th. Bjarnason, J.C. VanDecar, and S.C. Solomon, Seismic Structure of the Iceland mantle plume, *Nature, 385,* 245-247, 1997.

Yale, M.W., and J. Phipps Morgan, Asthenosphere flow model of hotspot-ridge interactions: a comparison of Iceland and Kerguelen, *Earth Planet. Sci. Lett., 161,* 45-56, 1998.

Zindler, A., and S.R. Hart, Geochemical geodynamics, *Annu. Rev. Earth Planet. Sci., 14,* 493-571, 1986.

Zindler, A., H. Staudigal, and R. Batiza, Isotope and trace element geochemistry of young Pacific seamounts: implications for the scale of upper mantle heterogeneity, *Earth Planet. Sci., Lett., 70,* 175-195, 1984.

BIOGRAPHICAL SKETCH

Dr. David John Chadwick acquired a Bachelor of Science Degree in geology from James Madison University in Harrisonburg, Virginia in 1987. In 1993, he obtained a Master of Science degree in Geology from Northern Arizona University in Flagstaff, Arizona. In 2002, he received a Ph.D. from the Department of Geological Sciences at the University of Florida in Gainesville, Florida.

Dr. Chadwick was employed by the Smithsonian Institution's Center for Earth and Planetary Studies from 1987 to 1989. As a research assistant there, he studied tectonic features on flood basalt plains on the Earth, Mars, and the Moon. From 1990 to 1994, he was employed as a research scientist by the U.S. Geological Survey in Flagstaff, Arizona. There he performed planetary geological research, focusing on the tectonism of the Valles Marineris on Mars and the formation of impact craters on Venus. He also studied the sand-penetration capabilities of airborne synthetic aperture radar in desert regions of the southwestern United States, and used remote sensing imagery to monitor glacier velocities in Antarctica. From 1994 to 1995, he was an employee of the Remote Sensing/GIS Center of the Army Corps of Engineers in Hanover, New Hampshire. There he worked with several different remote sensors to monitor oil spills in Russia and soil properties in New Hampshire. He also developed and taught a remote sensing course for Corps personnel. From 1995 to 1997, he worked at the NASA Goddard Space Flight Center, using Space Shuttle synthetic aperture radar (SIR-C) imagery to develop algorithms for monitoring soil conditions from space. While at NASA, he taught an introductory remote sensing course to NASA and U.S. Geological Survey employees, and scientists from the People's Republic of China. This course was developed into a semester-long class entitled 'Remote Sensing and GIS for Geologists', which he taught at the University of Florida in the Dept. of Geological Sciences in 2001.

I certify that I have read this study and that in my opinion it conforms to acceptable standards of scholarly presentation and is fully adequate, in scope and quality, as a dissertation for the degree of Doctor of Philosophy.

Michael R. Perfit

Michael R. Perfit
Professor, Geological Sciences

I certify that I have read this study and that in my opinion it conforms to acceptable standards of scholarly presentation and is fully adequate, in scope and quality, as a dissertation for the degree of Doctor of Philosophy.

Paul A Mueller

Paul A. Mueller
Professor, Geological Sciences

I certify that I have read this study and that in my opinion it conforms to acceptable standards of scholarly presentation and is fully adequate, in scope and quality, as a dissertation for the degree of Doctor of Philosophy.

David A. Foster
Associate Professor, Geological Sciences

I certify that I have read this study and that in my opinion it conforms to acceptable standards of scholarly presentation and is fully adequate, in scope and quality, as a dissertation for the degree of Doctor of Philosophy.

Ann Heatherington
Assistant in Geological Sciences

I certify that I have read this study and that in my opinion it conforms to acceptable standards of scholarly presentation and is fully adequate, in scope and quality, as a dissertation for the degree of Doctor of Philosophy.

Willie Harris

Willie Harris
Professor, Soil and Water Sciences

This dissertation was submitted to the Graduate Faculty of the Department of Geological Sciences in the College of Liberal Arts and Sciences and to the Graduate School and was accepted as partial fulfillment of the requirements for the degree of Doctor of Philosophy.

May 2002

Dean, Graduate School

LD
1780
2002
.C432

UNIVERSITY OF FLORIDA
3 1262 08555 3294